MICROSTRUCTURAL MATERIALS DESIGN USING DATA AND GRAPH

A Thesis

by

ABHILASH MOLKERI

Submitted to the Graduate and Professional School of
Texas A&M University
in partial fulfillment of the requirements for the degree of

DOCTOR OF PHILOSOPHY

Chair of Committee,	Ankit Srivastava
Committee Members,	Raymundo Arroyave
	Douglas Allaire
	Qing Tu
Head of Department,	Ibrahim Karaman

December 2021

Major Subject: Materials Science and Engineering

ABSTRACT

Technological advancements such as efficient jet engines and nuclear reactors rests on our ability to design and discover new materials. Historically, discovery of new materials has relied on Edisonian approach, but it is doubtful that this approach will efficiently meet our future needs. Thus, the aim of this dissertation is to enable goal-oriented material design and discovery. A goal-oriented closed-loop material design framework rests on our ability to correlate the design space (input) and objective (output). Most design frameworks tend to utilize a single source of data or information to exploit the input-output correlation even though often there are multiple sources of information. Herein, a closed-loop multi-fidelity Bayesian optimization framework is used to efficiently exploit a wide variety of information sources to design a dual-phase material with a targeted property. While fundamentally materials science involves the study of processing/chemistry - microstructure - property correlations, in practice, material design involves finding optimum processing/chemistry that yields desired properties, and the microstructure information is used to rationalize the observations. This raises a fundamental question, can the intermediate microstructural information aid in a material design campaign. To answer this, a novel microstructure aware design approach is proposed and compared against the traditional microstructure agnostic approach. The results show that the knowledge of material microstructure does not only rationalize an observation but can also accelerate the design process. Furthermore, some of the most critical material performance metrics depend on the detailed description of the length-scales associated with the material microstructure e.g., crack growth resistance. Intuitively, crack growth resistance of a material can be enhanced by microstructural design. However, microstructural design calls for a computationally efficient method to assess material's crack growth resistance within a closed-loop iterative design framework. To this end, a novel computationally efficient method utilizing evolving graphs and microstructural unit events is developed and validated against the results of microstructure-based finite element calculations of ductile fracture. The fully validated method is then used to design material microstructures with enhanced intergranular crack growth resistance.

ACKNOWLEDGMENTS

If a Ph.D. is a journey and you are in the driver's seat trying to make sense of things, your research advisor is the navigation system without whom there is no end of the tunnel. I want to express my sincere thanks to Prof. Ankit Srivastava for his constant guidance, inputs, and support during my entire journey. His attention to detail and curiosity in scientific investigations have encouraged me to continuously improve and thrive both professionally and personally. I have learned a lot from him, and I always try to emulate his best practices.

I would also like to thank Prof. Raymundo Arroyave, Prof. Douglas Allaire and Prof. Qing Tu for serving on my committee and for their invaluable guidance and feedback.

Furthermore, I would also like to express my sincere thanks to Prof. Alan Needleman and Prof. Shmuel Osovski for their invaluable guidance and feedback while carrying out some part of the work reported in this dissertation.

I would like to specifically acknowledge Dr. Seyede Fatemeh Ghoreishi, Dr. Richard Couperthwaite, Danial Khatamsaz, and Jaylen James for their immense help and support in carrying out some part of the work reported in this dissertation. I'm also lucky to have group members like Dr. Yu Liu, Dr. Xinzhu Zheng, Lara Draelos, Edwin Chiu, Zhara Ghasemi, who helped me so much in the formative years of my Ph.D.

Finally, on a more personal note, I would like to thank Hemant Rathod and Dr. Abhinav Srivastava, who have always cheered and been there for me. No words are enough to thank my friend Bhaskar Botcha, who has been a constant support in every aspect of my life and has breathed this Ph.D. journey with me. The list of people to whom I owe my gratitude would be incomplete without Siddhi Shrotri, who was always there to provide emotional support and motivation. Lastly, I'm thankful to my family, who always sacrificed their comfort for my success and building my career. I thank them for their unconditional love and support during my Ph.D.

CONTRIBUTORS AND FUNDING SOURCES

Contributors

This work was supported by a dissertation committee consisting of Professor Ankit Srivastava and Professor(s) Raymundo Arroyave and Qing Tu of the Department of Materials Science and Engineering and Professor Douglas Allaire of the Department of Mechanical Engineering.

The closed-loop multifidelity Bayesian optimization material design framework used in Chapters 2 and 3 were developed in collaboration with Dr. Seyede Fatemeh Ghoreishi, Dr. Richard Couperthwaite and Danial Khatamsaz.

Funding Sources

Graduate study was supported by the U.S. National Science Foundation grant CMMI-1663130.

TABLE OF CONTENTS

Page

LIST OF FIGURES

FIGURE Page

LIST OF TABLES

TABLE Page

1. INTRODUCTION

The ever-growing need of materials with enhanced properties and performance calls for materials scientists to discover new methods to design and develop materials with desired properties in a much faster and cost-effective manner compared to the traditional ways. Historically, design and discovery of new materials has involved extensive trial and error experiments to optimize its properties for the desired application. Therefore, these early methods have been expensive and required a long, laborious process before integrating the material into a commercial setup. To overcome this challenge, materials scientists have advocated a goal-oriented exploration of the material design space through experimental, computational, and/or data-driven methods to arrive at a material that meets the needs.

Essentially, the focus of a goal-oriented material design process is to predict the right combinations of material chemistry and processing route that yields a material with targeted properties, Figure 1.1. The goal-oriented material design approach is enabled by understanding and exploiting processing/chemistry - microstructure - property relationships. In this approach, the material is treated as a complex hierarchical system ultimately described by linkages along the processing/chemistry - microstructure - property (PSP) chain [1, 2, 3]. Next, the goal-oriented material design approach is enabled by exploiting the PSP relationships through iterative optimization techniques that search design space to find the optimum combinations of processing route and material chemistry that result in desired properties. This has led to initiatives such as Integrated Computational Materials Engineering (ICME) [4, 5] and Materials Genome Initiative [6].

While the exploitation of full PSP relationships is postulated as an essential element of a goal-oriented material design approach, establishing the quantitative PSP relationships requires explicit integration of multiple tools across multiple scales which is technically challenging [7]. Primarily due to the complex and highly coupled, multi-scale nature of linkages along the PSP chain. This complexity makes it very difficult to computationally emulate such PSP chains. Recently, some of these challenges have been addressed and there have been some successes in the establishment and

exploitation of fully integrated PSP relationships to carry out goal-oriented materials design [8, 9]. However, considerable cost associated with querying the PSP relationships along with the high-dimensional nature of the materials design space poses a major challenge on the practical implementation of goal-oriented materials design approaches.

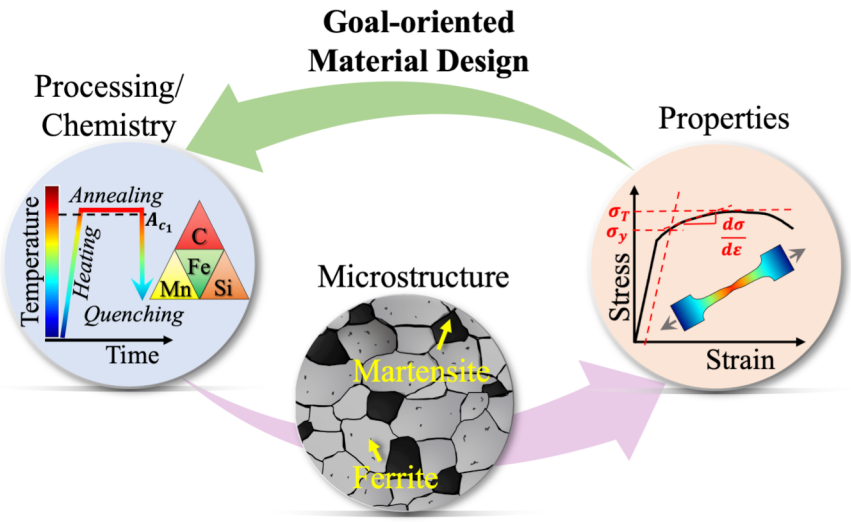

Figure 1.1: Schematic of a goal-oriented Materials Design process: Through exploitation of Processing/Chemistry-Microstructure-Property (PSP) relationships.

To overcome the limitations on resources and take the cost of exploring complex high dimensional materials design space into account, the concept of optimal experimental design using closed-loop Bayesian optimization (BO) techniques has been proposed [10, 11, 12, 13]. BO-based design frameworks are capable of efficiently balancing the exploration and exploitation of the materials design spaces. This is achieved by using a utility function within the concept of BO strategy. BO-based design approaches are carried out by constructing a surrogate model of physics-based models that correlates the design space (input) to the objective (output) to carry out queries. Most BO-based approaches in material design tend to use a single model or information source to correlate the input-output space [10, 11, 12], which is an unwarranted limitation as oftentimes there are multiple computational models with varying degrees of fidelity and cost, to

model the material behavior and correlate the input-output space. Furthermore, the current material design approaches are not capable of directly integrating experimental information into the design/optimization loop, other than for calibration, validation or verification purposes. Potential valuable experimental information could instead be directly incorporated into the material design framework but this remains largely unexplored. In fact, even state-of-the-art BO-based materials design [10, 11] tends to be limited to a single probe (experimental or computational) to query specific linkages of the PSP chain, although other engineering fields have developed sophisticated approaches for the integration of multiple information sources within optimization schemes [14].

In order to address the aforementioned challenges, in Chapter 2, a closed-loop multi-fidelity BO framework is presented for the design of materials that is capable of accounting for multiple information sources to correlate the input-output space. First, the demonstration of the material design framework is done through the microstructure-based design of a model dual-phase material. Specifically, the goal is to maximize the strength normalized strain-hardening rate of a dual-phase ferritic/martensitic steel. The mechanical response of the dual-phase steel is modeled through a wide variety of reduced-order mechanical models ('information sources') with varying degrees of fidelity as well as cost, and finally through a high-fidelity microstructure-based finite element model ('ground truth'). The available information from all mechanical models is fused through a reification approach and then a sequential experimental design is carried out. The experimental design seeks not only to identify the most promising region in the materials design space relative to the objective at hand, but also to identify the source of information that should be used to query this point in the decision space. The selection criterion for the source used, accounts for the discrepancy between the 'information source' and the 'ground truth' predictions as well as its cost. It is shown that when there is a hard constraint on the budget available to carry out the optimization, accounting for the cost of querying individual sources is essential.

As discussed earlier, fundamentally, materials science involves the study of PSP relationships, Figure 1.1. However, the overarching goal of the material design process involves finding the right combinations of processing route and material chemistry that yields desired properties. The

intermediate microstructure information is only used to carry out sophisticated multiscale simulations to establish the PSP relationships. Essentially, a goal-oriented material design process is microstructure agnostic, i.e., it does not explicitly exploit the microstructure information but only explores the direct processing/chemistry - property relationships. Even in several recent experimental campaigns to carry out material design, the optimum properties of a material are achieved through fine-tuning of its processing conditions and chemistry, and the microstructure information is only used to rationalize the observations and not as a direct input in the materials design process [15, 16, 17, 18]. Intuitively, these studies point to a fundamental question, can the intermediate microstructure information aid in searching for optimum processing parameters and material chemistry that yield desired properties more efficiently than otherwise.

In Chapter 3, detailed investigations are carried to probe the importance (if any) of the microstructure information in the materials design process to answer the question posed in the preceding paragraph. Specifically, the material design problem here involves finding the optimum combinations of material chemistry and processing parameters that maximize the strength normalized strain hardening rate of a model dual phase material. To establish the quantitative PSP relationships, a computational thermodynamic model is used to predict the microstructure, which is then used to predict the mechanical properties using a variety of micromechanical models and a microstructure-based finite element model. The material design problem is first solved by following the traditional *microstructure agnostic* approach where the material design space includes the material chemistry and processing routes, and the microstructure information is only used to carry out multiscale simulations to establish PSP relationships. Next, the same material design problem is solved by following a novel *microstructure aware* approach where the material design space includes not only the material chemistry and processing routes but also the intermediate microstructure information. Essentially, apart from the explicit incorporation of the microstructure information in the materials design space in the *microstructure aware* design approach, the two approaches are similar. Both the design approaches are solved using a closed-loop BO framework demonstrated in Chapter 2. The investigations carried out show that explicit incorporation of the

microstructure information in the materials design space significantly accelerates the materials design process. Thus, knowledge of the microstructure not only rationalizes the observed properties but also assists in the decision-making process as one navigates the materials design space.

In the previous materials design approaches, the materials' microstructures entered the design space in a homogenized way i.e., the topological details of the material microstructure was smeared out. However, the target property may or may not be insensitive to the topological details. For example, it is seen that the flow response of dual-phase advanced high strength steel sheets under uniaxial tension are similar along the rolling and transverse direction. However, the same dual-phase advanced high strength steel exhibited dissimilar bendability for sheets samples with bend axis parallel to rolling direction to the one from sheet samples with bend axis parallel to transverse direction [19]. Thus, design problems in which the target property is sensitive to the topological details of the microstructure require optimization of the topological features of the material's microstructure to carry out goal-oriented material design. For example, the crack growth resistance of a material depends on the detailed description of the length-scales associated with the material microstructure. It has been shown that crack growth resistance of the material can be enhanced by guiding the crack path through microstructure design [20], Figure 1.2. Here, the crack path was engineered by controlling the distribution of second-phase particles in a ductile matrix to increase the materials crack growth resistance. The controlled microstructure was characterized by various sinusoidal distributions of particles with the fixed mean particle spacing. The results presented in Ref. [20] indicate that the crack path can be engineered to increase the crack growth resistance by appropriately adding or removing particles that guide the crack path. Similarly in Ref. [21], it was shown that varying the grain morphology of material microstructure caused significant changes in the crack growth resistance of the material. Here, material microstructures characterized with different grain distributions but with similar average grain size resulted in significantly different crack growth resistances. Intuitively these studies point that material design to increase the crack growth resistance by microstructural design requires optimizing the topological features of the material microstructure. Although microstructure-based finite element calculations have shown to be

effective in assessing the crack growth resistance of a microstructure [20, 21, 22, 23], these calculations tend to be highly computationally expensive. Thus, the microstructural design here requires developing a computationally efficient method to assess materials crack growth resistance which can then be used within a closed-loop iterative design framework.

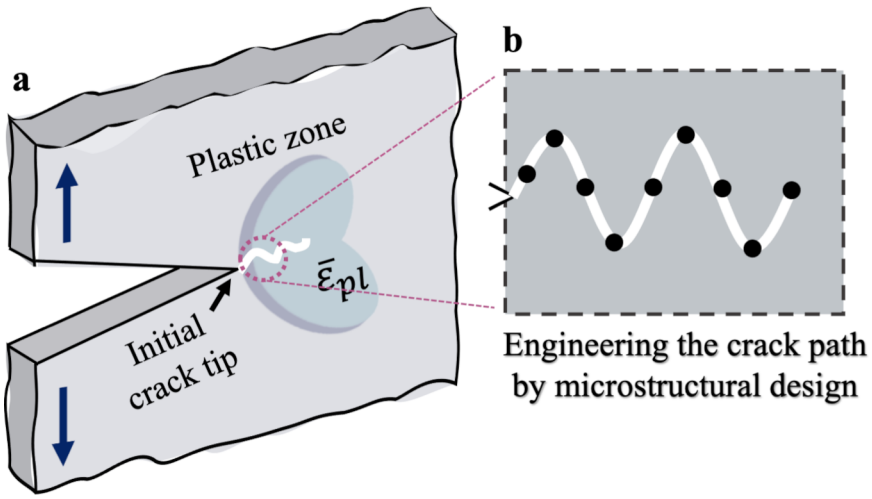

Figure 1.2: Schematic illustration of (a) the plastic zone and the growth of the crack (solid while line) from an initial notch and (b) the crack path in a material microstructure with sinusoidal distribution of discrete second-phase particles/inclusions (black solid circles) under mode I loading.

In order to carry out the efficient design of microstructures to enhance the crack growth resistance of a material, in Chapter 4, a novel computationally efficient method utilizing evolving graphs and microstructural unit events is proposed to infer crack path and crack growth resistance of material microstructure. The proposed approach outlines a method to search for optimum crack path under the circumstances where the knowledge of the target and graph are unknown a priori. For example, prediction of crack growth in heterogeneous material microstructure involves search for crack path where the knowledge of target i.e., end of the crack and the graph i.e., connectivity between microstructural features is in general unknown. The prediction of crack path and its crack growth resistance are carried out in two type of material microstructures. First, disconnected microstructural network, which consists of distribution of discrete inclusions or second-phase par-

ticles. These inclusions act as nodes in a graph through which the crack propagates and the connections i.e., the edges between these nodes in not known a priori. The second type of microstructure considered is a connected microstructural network and contains fully resolved grains and grain boundaries along which the crack propagates. Here, the grain boundary junctions act as nodes and grain boundaries act as edges connecting these nodes. Next, the crack path prediction in both of these microstructural networks is carried out by searching for an optimal path starting from the source i.e., the initial crack tip. Prediction of crack path is carried out by first building a local graph at every time step and selecting the optimum local crack path by using the knowledge of microstructural unit events. For a given microstructure, the final predicted crack path is then the collection of all local crack paths obtained at every time step. Finally, crack growth resistance curve is then calculated based on the predicted crack path and is compared with the results of full-field finite element calculations of ductile fracture. The full field finite element calculations are carried out for plane strain slice of materials with disconnected and connected microstructural networks subjected to mode I small-scale yielding conditions. The finite element formulation accounts for finite deformations, and the constitutive relation models the loss of stress carrying capacity due to progressive void nucleation, growth, and coalescence.

Following this in Chapter 5, using microstructure-based finite element calculations and evolving graphs proposed in Chapter 4, the influence of grain size distribution on ductile intergranular crack growth resistance is investigated. The crack path and crack growth resistance curves are predicted by the same approach developed in Chapter 4 and compared with the results of finite element calculations. The effect of unimodal and bimodal grain size distributions on intergranular crack growth is considered. It is found that a significant increase in crack growth resistance is obtained if the difference in grain sizes in the bimodal grain size distribution is sufficiently large.

2. MATERIALS DESIGN USING MULTIPLE INFORMATION/DATA SOURCES *

2.1 Introduction

Integrated Computational Materials Engineering (ICME) [4, 5], as currently understood, consists of the integration of multiple levels of computational tools, in combination with experiments, along the materials design/optimization chain to (i) establish quantitative Process-Structure-Property-Performance (PSPP) relationships; and (ii) exploit the so-established PSPP relationships in the acceleration of the materials design/optimization process. A challenge associated with ICME is the fact that the explicit integration of multiple computational materials tools remains an outstanding task [24].

While there have been successes in terms of fully integrated ICME approaches to materials design [25, 26, 27, 8], in most cases it is assumed that at each level/scale of simulation there is only one model that serves as a linkage along the PSPP relationship. This paradigm is somewhat restrictive as it is often the case that there are multiple models, with different levels of fidelity and associated (computational) costs, that could potentially be used to carry the modeling chain forward. Furthermore, existing frameworks do not explicitly account for the possibility of using other types of information or data, such as experiments, alongside computational models, within the same materials design/optimization framework.

It is further considered that ICME poses the establishment of linkages along the PSPP chain as a necessary, but not sufficient, condition towards the acceleration of the materials design/optimization process. ICME-based PSPP model chains tend to be computationally costly and a key outstanding challenge is how to utilize these ICME tools to efficiently explore the Materials Design Space (MDS). Currently, high-throughput (HT) experimental [28, 29, 30] and computational [31] exploration of the materials space constitute the dominant paradigm. These approaches, however, tend to be sub-optimal when there are constraints on available resources.

To overcome the challenges associated with the open-loop exploration (computational or otherwise) of MDS, notions of optimal experimental design—based on Bayesian Optimization (BO), for example—have been put forward [12, 32] and have been shown to be quite effective in carrying out the targeted search of optimal materials solutions by balancing the exploration and exploitation of the MDS. However, most BO-based frameworks, similar to ICME-based works, rely on a single source of information/data (i.e., model or experimental response surface) to query the MDS. In the absence of sufficient data—as it is most often the case in materials design/optimization problems—relying on a single model from the start is highly risky. Moreover, such an approach is limited as it implicitly requires the use of the most accurate approximation to the 'ground truth' available to query the design space at every step of the sequential materials design/optimization task. However, a high degree of fidelity to the 'ground truth' often comes at a considerable cost in terms of resources and time.

In the works of [32, 10], the authors have recently sought to address this challenge by adaptively selecting competing (non-parametric) theories or models relating materials features to their performance [32, 10]. The framework begins the exploration of the MDS by assuming that each of the competing models has equal weight. The weight of individual models is then adjusted by computing the Bayesian evidence relative to the acquired data. Bayesian Model Averaging (BMA) is then used to find the best next point to query in the design space as determined by all the competing models with their relative contribution to the utility function being adjusted by their updated weight. The framework, however, took a very conservative approach to information fusion and treated each model as statistically independent, ignoring the correlations between the models that could potentially be exploited in the materials design/optimization scheme. While this may not be a major issue when using non-parametric models—i.e., models that have no internal structure based on/constrained by physics—, this may be a significant limitation when the models available are all connected by the common physical phenomena they intend to represent.

State-of-the-art of approaches to the computer/data-enabled discovery and/or design of materials has moved forward significantly but there remain important issues to address. Specifically,

model-based ICME approaches focus on integration of tools along the PSPP relationship assuming there is only one model/tool relevant to each level of the problem. On the other hand, data-centric approaches tend to focus on the brute-force exploration of the MDS, without much emphasis on being able to inform decisions on where to explore next based on the knowledge acquired. Furthermore, both types of frameworks tend to discount the need for allocating resources in an efficient manner.

Here, a framework is presented that addresses the challenges outlined above. Specifically, to tackle the challenge of optimizing the features of a dual-phase microstructure for a specific (mechanical) property/performance metric. It is further assumed that there are availability of a set of models of varying complexity (or computational cost) and fidelity. It is also considered that there is access to a 'ground truth', in the form of an expensive microstructure-based finite element model that can be queried at much more expense than the other sources of information and that, therefore, should be queried as infrequently as possible, provided the design space represented by such 'ground truth' is sampled efficiently.

The (inexpensive) sources used in this work are fused by accounting for their mutual correlation as well as their correlation with the 'ground truth'. The framework accounts for the value of individual 'information sources' in relation to the property we wish to optimize. The queried source is used to construct a fuse model that represents our best estimate for the response of the 'ground truth'.The fused model is then incorporated within a Knowledge Gradient (KG) framework in order to carry out, in a principled manner, two decisions: (i) which source to query the MDS; and (ii) which location of the MDS to query; taking into account a fixed budget (cost) for queries to carry out before assessing the 'ground truth'.

While the framework is demonstrated in a computational context, the problem set up and its resolution closely mimics a typical materials design/optimization campaign: (i) there are more than one potential source of information (experimental and/or computational) about the system to be investigated; (ii) each of the 'information sources' has different degree of fidelity with regards to the 'ground truth'; (iii) each source has different cost (monetary and/or otherwise); and (iv)

there are hard constraints in time and resources available to complete the research campaign. The last point is often overlooked but constitutes a very important limitation to the effectiveness of any approach towards materials design/optimization. Indeed, towards the end of the work, ample (computational) evidence for the fundamental importance for accounting not only for the utility but for the cost of 'information sources' when there are (as always) hard resource constraints is provided.

2.2 Methods

2.2.1 Mechanical Behavior of Dual-Phase Microstructures

In this work, the materials design/optimization framework is demonstrated by focusing on the mechanical response of dual-phase advanced high strength steels. In these alloy systems, the microstructure consists of a relatively soft, ductile ferrite phase that is strengthened by the hard martensite phase [33]. The overall mechanical response of these dual-phase microstructures are controlled by the (non-linear) properties of the constituent phases, the microstructural features such as volume fraction, and the (non-linear) interaction among the constituent phases [34, 23, 22, 35]. In principle, the overall response of these dual-phase microstructures can be tuned and optimized. Unfortunately, any approach to microstructure design/optimization that does not rely on predictive models for the overall response of the microstructure will require extensive and expensive trial-and-error experimentation.

The overall mechanical response of composite dual-phase microstructures can be predicted with a higher level of fidelity through the use of single [34, 23, 22, 35] or multi-scale [36, 37] microstructure-based finite element calculations. Unfortunately, these models tend to be computationally costly which prevents their use to carry out direct optimization—of mechanical properties—over the entire microstructure space. On the other extreme, simple reduced-order models that make strong assumptions on how strain[38], stress [39] or work of deformation [40] partitions between the constituent phases are computationally cheap, but they offer much lower fidelity and predictability. At an intermediate level of complexity/fidelity, the response of dual-phase

microstructures can be predicted using sophisticated micromechanical homogenization schemes that consider the dual-phase microstructure as a matrix with inclusions of another phase homogeneously dispersed within it [41]. All these models, however, are only capable of predicting the (non-linear) mechanical response of these microstructures with varying degrees of accuracy (relative to a microstructure-based finite element calculation). Moreover, the computational cost of these reduced-order and micromechanical models also differ significantly—by orders of magnitude.

Recognizing the advantages and limitations of different potential cheap models used to predict the response of dual-phase microstructures, in this work all of them—reduced-order models and micromechanical homogenization schemes— are treated as sources of information with varying value and cost, with regards to the optimization problem at hand. In other words, in order to tackle the challenge of optimizing the dual-phase microstructures for enhanced mechanical performance, it is assumed that are a set of models of varying complexity (or computational cost) and fidelity available. In order to demonstrate this framework, the high-fidelity microstructure-based finite element calculations are considered as 'ground truth'. Furthermore, the cost to query the 'ground truth' is taken to be much more expensive than the other sources of information.

Before all the 'information sources' and the finite element calculations are described, it is noted that the problem posed here is a drastic simplification of the real problem—even within a simulation-only setting—as the fact that microstructure that is ultimately controlled via material chemistry and processing, is completely ignored. A more realistic problem setup would consist of models incorporating the process/chemistry-microstructure connection as well as the effect of both the chemistry and the processing conditions on the properties of the constituent phases. For the sake of demonstration, in this work the process/chemistry-microstructure connection is ignored and the design space is limited to simple microstructural descriptors.

2.2.1.1 Microstructure-based finite element modeling

The microstructure-based finite element modeling to predict the overall mechanical response of dual-phase microstructures is carried out using 3D representative volume elements (RVEs) as

described in [35, 13]. Fig. 2.1 shows two realizations of a 3D RVE of a dual-phase microstructure with about 50% volume fraction of the martensite (hard) phase. The RVEs are constructed using C3D8 brick elements of the ABAQUS/Standard element library [42], and have a dimension of 100μm $\times$ 100μm $\times$ 100μm. The RVEs are subjected to monotonically increasing uniaxial tensile deformation under periodic boundary conditions.

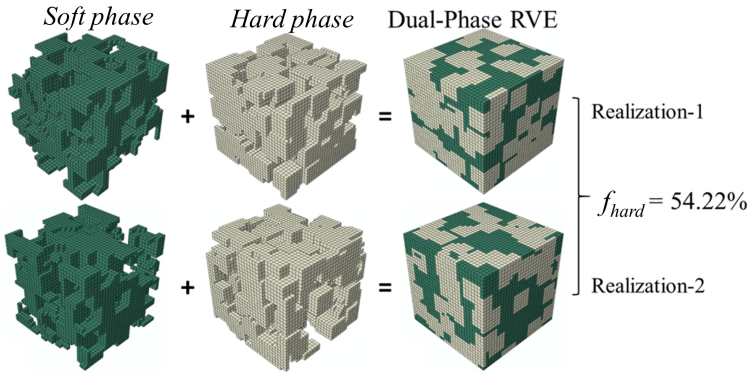

Figure 2.1: Two realizations of the representative volume element (RVE) of a dual-phase microstructure with 54.22% (by volume) of a hard (martensite) phase. The two realizations refer to different distributions of the hard phase particles in the RVE with a fixed phase volume fraction.

In the finite element calculations, it is assumed that both the ferrite and the martensite phase follow an isotropic elastic-plastic constitutive relation, with identical Young's modulus—$E = 200$GPa—and Poisson's ratio—$\nu = 0.3$, and a Ludwik type strain-hardening response,

$$\tau^p = \tau_o^p + K^p(\epsilon_{pl}^p)^{n^p}, \tag{2.1}$$

where τ^p is the flow stress, ϵ_{pl}^p is the plastic strain, τ_o^p is the yield strength, K^p is the strengthening coefficient, and n^p is the strain-hardening exponent of phase p. The values for these parameters are given in Table 2.1. The models are qualitative in nature and the parameters used are chosen in order to have a microstructure that represents a soft phase (ferrite) with a lower initial yield strength and a higher strain-hardenability than the hard phase (martensite) [34, 23, 22, 35].

Table 2.1: Parameterization of the Ludwik power law for the constituent phases of the dual-phase microstructure.

Constituent Phase, p	τ_o^p **[MPa]**	K^p **[MPa]**	n^p
Soft (ferrite)	300	2200	0.5
Hard (martensite)	1500	450	0.06

2.2.1.2 Reduced-order models

The overall mechanical response of a dual-phase microstructure can also be predicted using reduced-order models constructed under different assumptions regarding the partitioning of strain, stress or work of deformation among the constituent phases. Three such reduced-order models considered here are: (i) the Voigt/Taylor model that assumes isostrain partitioning, (ii) the Reuss/Sachs model that assumes equipartitioning of stress and (iii) the isowork model that assumes both phases undergo identical works of deformation as the composite microstructure is deformed [43]. For all three reduced-order models the constitutive relation, $\tau^p = f(\epsilon_{pl}^p)$, is assumed to follow Eq. (2.1), with the values of the parameters given in Table 2.1.

2.2.1.3 Micromechanical models

In addition to the simple reduced-order models presented above, three more sophisticated micromechanical homogenization schemes as sources of information that provide estimates of the overall mechanical response of dual-phase microstructures are also exploited. The first two homogenization schemes employed here are referred to as 'secant method - 1' and 'secant method - 2', whereas the third one is referred to as the 'elastic constraint' method. The secant method proposed by Weng [41], predicts the mechanical response of a two-phase composite microstructure based on Hill's weakening constraint power in a plastically-deforming matrix. In a dual-phase microstructure, where both the phases are capable of undergoing plastic deformation, and the phase constitution covers the entire range, i.e., zero-to-one (0% phase 1 & 100% phase 2) to one-to-zero (100% phase 1 & 0% phase 2), it is difficult to decide which phase should be considered as an

inclusion and which phase should be considered to be the matrix. Thus, the 'secant method - 1' is the secant method proposed by Weng [41], where the ferrite phase is considered the matrix, while the scenario when martensite is considered the matrix is referred to as 'secant method - 2'. It is expected that these two variants of the secant method will be valid in opposite regions in the microstructure design space. The third homogenization scheme, referred to as 'elastic constraint', is based on Kröner's treatment of the matrix-inclusion system under elastic constraints [41]. For this method, the final prediction does not depend on which phase, ferrite or martensite, is assumed as inclusion or the matrix. For all three homogenization schemes, 'secant method - 1', 'secant method - 2' and 'elastic constraint', the inclusion-inclusion interaction at finite concentration are accounted for by the Mori-Tanaka method. For all three homogenization schemes, the constitutive relation, $\tau^p = f(\epsilon^p_{pl})$, is assumed to follow Eq. (2.1), with the values of the parameters given in Table 2.1.

2.2.1.4 Comparison of the predictions of 'information sources' and the 'ground truth'

In this work, all the reduced-order models, Section 2.2.1.2, and micromechanical homogenization schemes, Section 2.2.1.3 are treated, as sources of information, while the microstructure-based finite element calculations, Section 5.2, is treated as 'ground truth'.

The predicted flow curve of a dual-phase microstructure with 25% volume fraction of the hard (martensite) phase, using the reduced-order models and micromechanical homogenization schemes are compared against the finite element results in Fig. 2.2. As can be seen from the figure, compared to the finite element predictions, the isostress model significantly under-predicts the stress values at nearly all plastic strain levels. The isostrain and isowork models, on the other hand, over-predict the stress at low strain levels. However, at large strain levels their predictions are comparable with the finite element predictions. In addition, none of the reduced-order models are able to correctly predict the overall strain-hardening response of the dual-phase microstructure. Of all the micromechanical homogenization schemes, predictions of the Weng [41] secant model with soft phase as matrix (secant method - 1) are comparable with the finite element calculations at low strain levels. The predictions of the Weng [41] secant model with hard phase as matrix (secant method - 2) and the elastic constraint model are roughly the same, and at low strain levels both

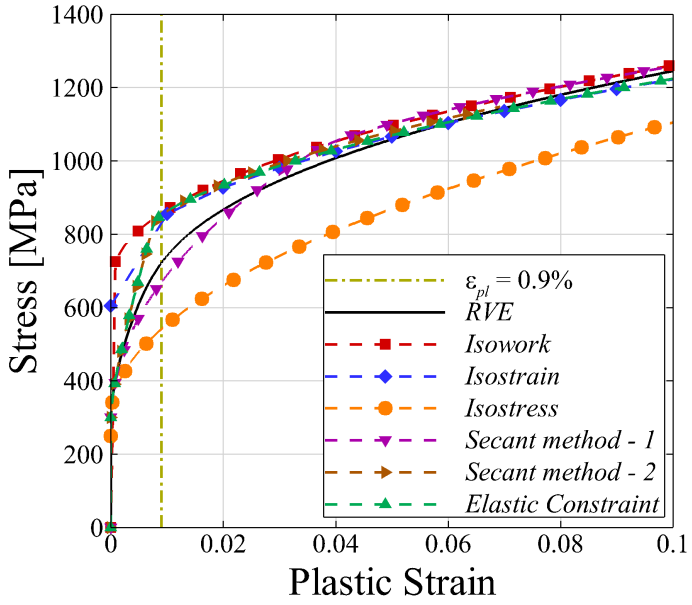

Figure 2.2: Comparison of the predicted stress-plastic strain curves by the three reduced-order models and the three micromechanical homogenization schemes with the microstructure-based finite element calculations (RVE) of a dual-phase microstructure with 25% volume fraction of the hard phase.

over predict the stress values.

The flow strength and the strain-hardenability of a material are two very important mechanical properties with practical implications for both its performance and manufacturability. These two fundamental mechanical properties can be reduced to a single metric by introducing a strength normalized strain-hardening rate, given as $(1/\tau)(\mathrm{d}\tau/\mathrm{d}\epsilon_{pl})$. This quantity provides an indication of the ductility and formability of the material, with higher values corresponding to higher ductility and formability. Fig. 2.3 shows how $(1/\tau)(\mathrm{d}\tau/\mathrm{d}\epsilon_{pl})$ varies with the volume fraction of the hard phase, f_{hard}, estimated at a plastic strain level of $\epsilon_{pl} = 0.9\%$ from the microstructure-based finite element calculations. The figure shows that $(1/\tau)(\mathrm{d}\tau/\mathrm{d}\epsilon_{pl})$ exhibits a maxima at a finite volume fraction of the hard phase. The variation of $(1/\tau)(\mathrm{d}\tau/\mathrm{d}\epsilon_{pl})$ in the figure also exhibits small perturbations, indicated as error bars, arising from seven different realizations of the RVE representation of the dual-phase microstructure with identical phase constitutions. The response of $(1/\tau)(\mathrm{d}\tau/\mathrm{d}\epsilon_{pl})$ predicted

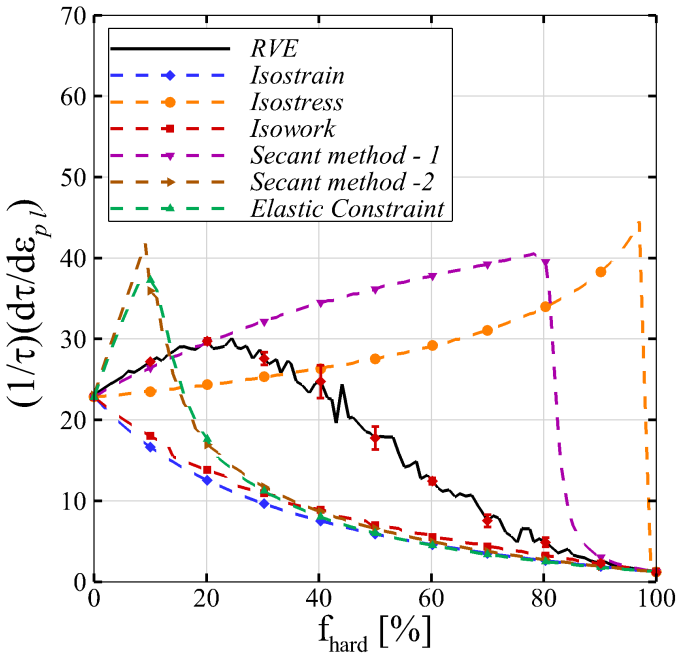

Figure 2.3: Strength normalized strain-hardening rate $(1/\tau)(\mathrm{d}\tau/\mathrm{d}\epsilon_{pl})$ at $\epsilon_{pl} = 0.9\%$ as a function of the volume fraction of the hard phase, f_{hard}. Predictions of the three reduced-order models and three micromechanical homogenization schemes are compared to the microstructure-based finite element calculations (RVE).

using the three reduced-order models and the three micromechanical homogenization schemes are also shown in Fig. 2.3. As can be seen, none of the approximate models or 'information sources' are capable of reproducing the response predicted using the microstructure-based finite element calculations over the entire phase constitution space. The 'Secant method-1' approximation is capable of reproducing the response at small volume fractions of the hard phase but the discrepancy with the 'ground truth' becomes significant at volume fractions above 20%. Most models tend to converge towards the finite element predictions when the majority of the microstructure consists of the hard phase. In this regime, the microstructure exhibits no strain-hardenability.

The results presented in Fig. 2.3 clearly show that all the 'information sources'—reduced-order models and micromechanical homogenization schemes—are incapable of reproducing the 'ground truth' with an acceptable level of fidelity. On the other hand, these 'information sources' are cheap and their predictions differ from the 'ground truth' in a systematic manner. So it may be possi-

Table 2.2: Computational cost of various 'information sources' used.

Information Source	Cost (seconds)	Normalized Cost
Reduced-order Models		
iso-strain	2.3×10^{-4}	1
iso-stress	1.0×10^{-3}	4.4
iso-work	4.7×10^{-1}	2.0×10^{3}
Micromechanical models		
secant method 1	3.8×10^{1}	1.7×10^{5}
secant method 2	8.4×10^{1}	3.7×10^{5}
elastic constraint	3.6×10^{1}	1.6×10^{5}
Finite element (RVE) or 'ground truth'		
RVE	7.2×10^{3}	3.1×10^{7}

ble to learn this discrepancy and use this knowledge to arrive at a more robust estimation of the 'ground truth' at an extremely low cost. The computational cost of each 'information source' and the 'ground truth' is calculated based on their run time on a PC equipped with an Intel® Xeon® E5-2670 v2 (Ivy Bridge-EP) processor. The run time of a given 'information source' was determined by tracking the wall-clock time using 'tic' and 'toc' functions in MATLAB. To avoid the effect of external load due to memory constraints, each 'information source' was queried 1000 times and the average run time of 1000 queries was considered as the run time or cost of each 'information source'. The final assigned computational cost to each 'information source' are given in Table 2.2. While all the 'information sources' considered here are computational models and the costs for each information-source is simply the computational time, this approach is generic enough to incorporate any other type of 'information source' or cost, as long as they can be represented in a consistent fashion.

2.2.2 Design Framework

The overall framework seeks to optimize an objective function assuming that there are multiple 'information sources' that can be used to query the input space. This problem is formulated following the work described in [13], however, here the expense of executing a given 'information

source' in the framework is explicitly incorporated:

$$\mathbf{x}^* =_{\mathbf{x}\in\chi} f(\mathbf{x}), \tag{2.2}$$

where f is the objective function, and $\mathbf{x}$ is a set of design variables in the vector space χ. In real-world applications, the objective function is often unknown and expensive to evaluate, and there are oftentimes constraints placed on decision-making. Additionally, in most real-world applications, there are potentially multiple ways in which one can query the design space. One can use, for example, a combination of numerical simulations, experiments and expert opinions, to approximate the objective function with varying fidelity or accuracy, and with varying cost (monetary or otherwise). Here, the an approach is presented that exploits all available 'information sources'. In each step of the approach, the choice of what 'information source' to sample and with what input (or region in the design space), is based on a trade off between the cost and fidelity of a specific 'information source'.

In this work it is assumed that are S 'information sources', $f_i(\mathbf{x})$, where $i \in \{1, 2, \ldots, S\}$, available that can be used to approximate the objective function, $f(\mathbf{x})$, at $\mathbf{x}$. Next, the response of each source through GP-based surrogates is modeled. These GPs are fit using data from previous queries, $\{\mathbf{X}_{N_i}, \mathbf{y}_{N_i}\}$, where $\mathbf{X}_{N_i} = (\mathbf{x}_{1,i}, \ldots, \mathbf{x}_{N_i,i})$ corresponds to the N_i input samples used to query the response of source i and $\mathbf{y}_{N_i}$ corresponds to the output—the domain of the 'information source' correspond to the microstructural degrees of freedom (i.e., phase fractions) available. The posterior GPs distributions of each f_i, $f_{GP,i}(\mathbf{x})$, at any point $\mathbf{x}$ are

$$f_{GP,i}(\mathbf{x}) \mid \mathbf{X}_{N_i}, \mathbf{y}_{N_i} \sim \mathcal{N}\left(\mu_i(\mathbf{x}), \sigma^2_{GP,i}(\mathbf{x})\right), \tag{2.3}$$

where

$$\mu_i(\mathbf{x}) = K_i(\mathbf{X}_{N_i}, \mathbf{x})^T [K_i(\mathbf{X}_{N_i}, \mathbf{X}_{N_i}) + \sigma^2_{n,i} I]^{-1} \mathbf{y}_{N_i}, \tag{2.4}$$

and

$$\sigma^2_{GP,i}(\mathbf{x}) = k_i(\mathbf{x},\mathbf{x}) - K_i(\mathbf{X}_{N_i},\mathbf{x})^T[K_i(\mathbf{X}_{N_i},\mathbf{X}_{N_i}) + \sigma^2_{n,i}I]^{-1}K_i(\mathbf{X}_{N_i},\mathbf{x}). \tag{2.5}$$

Here, k_i is a real-valued kernel function associated with 'information source' i over the input space, $K_i(\mathbf{X}_{N_i},\mathbf{X}_{N_i})$ is the $N_i \times N_i$ matrix whose m,n entry is $k_i(\mathbf{x}_{m,i},\mathbf{x}_{n,i})$, $K_i(\mathbf{X}_{N_i},\mathbf{x})$ is the $N_i \times 1$ vector whose m^{th} entry is $k_i(\mathbf{x}_{m,i},\mathbf{x})$ for 'information source' i, and the term $\sigma^2_{n,i}$ can be used to model observation error of 'information source' i or to guard against numerical ill-conditioning. A major ingredient of GPs is the prior information about the degree of correlation between different points in the input space. This information is encoded in a kernel function. In this work a relatively smooth response surface is assumed, based on the behavior of the 'ground truth' shown in Fig. 2.3 and thus the squared exponential kernel is used,

$$k_i(\mathbf{x},\mathbf{x}') = \sigma_s^2 \exp\left(-\sum_{h=1}^{d}\frac{(x_h - x'_h)^2}{2l_h^2}\right), \tag{2.6}$$

where d is the dimension of the input space, σ_s^2 is the variance, and l_h, where $h = 1,2,\ldots,d$, is the characteristic length-scale that measures the degree of correlation in the input space. It is assumed that each dimension of the input space, h, has its own stationary characteristic length-scale—the formulation is general but in this case it is attempted to solve an optimization problem with a one dimensional design/input space. The GP models for each 'information source' are fit through maximum likelihood or Bayesian techniques [44].

The uncertainty of each 'information source' with respect to the 'ground truth' can be estimated from the intrinsic variance of the GP as well as the discrepancy between the 'information source' and the 'ground truth':

$$\sigma_i^2(\mathbf{x}) = \sigma^2_{GP,i}(\mathbf{x}) + \sigma^2_{f,i}(\mathbf{x}), \tag{2.7}$$

where $\sigma^2_{f,i}(\mathbf{x})$ is the variance of the discrepancy of 'information source' i. It is noted that this variance can in principle vary over the input space.

While it is to be expected that low cost 'information sources' with missing physics will ex-

hibit large discrepancies with respect to the 'ground truth', in this work the hypothesis is that every source contains useful information about the 'ground truth' that is expensive/difficult to observe/query. In this specific case this is justified as all the reduced-order models and homogenization schemes use the same inputs and produce the same outputs as the 'ground truth' microstructure-based finite element calculations. More importantly, from an epistemic point of view, all the 'information sources' seek to predict the response of a microstructure as a function of imposed loading using different theoretical frameworks and/or physical assumptions. Regardless of the underlying assumptions (e.g. how stress, strain or work are partitioned among the different phases), all sources are 'causally' connected to the same underlying 'ground truth' and it is thus expected that they will be correlated—to differing degrees—to it.

Since all 'information sources' potentially have information about the 'ground truth', they are fused, using following standard approaches for the fusion of normally distributed data [45], as they are all represented as GPs. According to this fusion method, the fused mean and variance at point $\mathbf{x}$ can be computed as

$$\mu_{\text{Wink}}(\mathbf{x}) = \frac{\mathbf{e}^T \tilde{\Sigma}(\mathbf{x})^{-1} \mu(\mathbf{x})}{\mathbf{e}^T \tilde{\Sigma}(\mathbf{x})^{-1} \mathbf{e}}, \tag{2.8}$$

$$\sigma^2_{\text{Wink}}(\mathbf{x}) = \frac{1}{\mathbf{e}^T \tilde{\Sigma}(\mathbf{x})^{-1} \mathbf{e}}, \tag{2.9}$$

where $\mathbf{e} = [1, \ldots, 1]^\top$, $\mu(\mathbf{x}) = [\mu_1(\mathbf{x}), \ldots, \mu_S(\mathbf{x})]^\top$ contains the mean values of S sources at point $\mathbf{x}$, and $\tilde{\Sigma}(\mathbf{x})$ is the covariance matrix between sources,

$$\tilde{\Sigma}(\mathbf{x}) = \begin{bmatrix} \sigma_1^2(\mathbf{x}) & \cdots & \rho_{1S}(\mathbf{x})\, \sigma_1(\mathbf{x}) \sigma_S(\mathbf{x}) \\ \rho_{12}(\mathbf{x})\, \sigma_1(\mathbf{x}) \sigma_2(\mathbf{x}) & \cdots & \rho_{2S}(\mathbf{x})\, \sigma_2(\mathbf{x}) \sigma_S(\mathbf{x}) \\ \vdots & \ddots & \vdots \\ \rho_{1S}(\mathbf{x})\, \sigma_1(\mathbf{x}) \sigma_S(\mathbf{x}) & \cdots & \sigma_S^2(\mathbf{x}) \end{bmatrix}, \tag{2.10}$$

where $\sigma_i^2(\mathbf{x})$ is the total variance of source, i, at a point $\mathbf{x}$ computed in Eq. (2.7) and $\rho_{ij}(\mathbf{x})$ is the correlation between the deviations of 'information sources' i and j at point $\mathbf{x}$. The reification process described in [46, 47] is used, to estimate the correlation between the errors of sources i

and j, computed as

$$\rho_{ij}(\mathbf{x}) = \frac{\sigma_j^2(\mathbf{x})}{\sigma_i^2(\mathbf{x}) + \sigma_j^2(\mathbf{x})}\tilde{\rho}_{ij}(\mathbf{x}) + \frac{\sigma_i^2(\mathbf{x})}{\sigma_i^2(\mathbf{x}) + \sigma_j^2(\mathbf{x})}\tilde{\rho}_{ji}(\mathbf{x}), \tag{2.11}$$

which is the variance weighted average of the correlation coefficients computed by reifying sources i and j respectively as

$$\begin{aligned} \tilde{\rho}_{ij}(\mathbf{x}) &= \frac{\sigma_i(\mathbf{x})}{\sqrt{\left(\mu_i(\mathbf{x}) - \mu_j(\mathbf{x})\right)^2 + \sigma_i^2(\mathbf{x})}}, \\ \tilde{\rho}_{ji}(\mathbf{x}) &= \frac{\sigma_j(\mathbf{x})}{\sqrt{\left(\mu_j(\mathbf{x}) - \mu_i(\mathbf{x})\right)^2 + \sigma_j^2(\mathbf{x})}}, \end{aligned} \tag{2.12}$$

where $\mu_i(\mathbf{x})$ and $\mu_j(\mathbf{x})$ correspond to the means of sources i and j, and $\sigma_i^2(\mathbf{x})$ and $\sigma_j^2(\mathbf{x})$ are the total variances of 'information sources' i and j at $\mathbf{x}$. The correlations between the errors of two models/sources is estimated using the procedure described in [46, 47]. The fused means and variances in the input design space χ are used to construct a fused GP model. Letting $\mu_{\text{Wink}}(\mathbf{x}_{1:N_f})$ and $\Sigma(\mathbf{x}_{1:N_f}) = \text{diag}\left(\sigma^2_{\text{Wink}}(\mathbf{x_1}), \ldots, \sigma^2_{\text{Wink}}(\mathbf{x}_{N_f})\right)$ be the vector of fused means with a diagonal matrix of the fused variances at the sampling set $\mathbf{x}_{1:N_f} \subset \chi$, the posterior predictive distribution of the fused model is given by:

$$\hat{f}^{\text{fused}}(\mathbf{X}) \sim \mathcal{N}(\mu^{\text{fused}}(\mathbf{X}), \Sigma^{\text{fused}}(\mathbf{X})), \tag{2.13}$$

where

$$\begin{aligned} \mu^{\text{fused}}(\mathbf{X}) &= K(\mathbf{x}_{1:N_f}, \mathbf{X})^T [K(\mathbf{x}_{1:N_f}, \mathbf{x}_{1:N_f}) + \Sigma(\mathbf{x}_{1:N_f})]^{-1} \mu_{\text{Wink}}(\mathbf{x}_{1:N_f}), \\ \Sigma^{\text{fused}}(\mathbf{X}) &= K(\mathbf{X}, \mathbf{X}) - K(\mathbf{x}_{1:N_f}, \mathbf{X})^T [K(\mathbf{x}_{1:N_f}, \mathbf{x}_{1:N_f}) + \Sigma(\mathbf{x}_{1:N_f})]^{-1} K(\mathbf{x}_{1:N_f}, \mathbf{X}). \end{aligned} \tag{2.14}$$

By constructing the fused GP, in each iteration of the proposed methodology, the next design point is determined—i.e., phase fraction to evaluate—and 'information source' to query—i.e., model connecting microstructure and response—by balancing the cost of the query and the value of such query relative to the objective function, Eq. (2.2). In order to select the next point to query, first

a Latin Hypercube experimental design is generated, denotes as $\mathbf{X}_{\text{alt}}$ over the input space. Let $(\mathbf{x}_{1:N}, y_{1:N})$ be the design points and the corresponding objective values, and $i_{1:N}$ be the indices of the queried 'information sources' up to time step N. In a Bayesian optimization framework, the choice of utility function determines the next (unobserved) point in the design space to explore. While there are a number of possible utility functions to choose from, here a two-step look ahead utility is proposed, which considers the immediate improvement in one step as well as the expected improvement in two steps.

This utility, which is obtained by querying the design point $\mathbf{x} \in \mathbf{X}_{\text{alt}}$ from 'information source' i is defined as

$$U_{\mathbf{x},i} = \mathbb{E}\left[\max_{\mathbf{x}' \in \mathbf{X}_{\text{alt}}} \mu^{\text{fused}}(\mathbf{x}') + \max_{\mathbf{x}'' \in \mathbf{X}_{\text{alt}}} EI_{\mathbf{x},i}(\mathbf{x}'') \;\middle|\; \mathbf{x}_{1:N}, y_{1:N}, i_{1:N}, \mathbf{x}_{N+1} = \mathbf{x}, i_{N+1} = i \right], \quad (2.15)$$

where $EI_{\mathbf{x},i}(\mathbf{x}'')$ is the one-step look-ahead expected increase in the maximum of the fused GP given $\mathbf{x}_{N+1} = \mathbf{x}$ and $i_{N+1} = i$ as

$$EI_{\mathbf{x},i}(\mathbf{x}'') = \mathbb{E}\big[\max_{\mathbf{x}' \in \mathbf{X}_{\text{alt}}} \mu^{\text{fused}}(\mathbf{x}') \mid \mathbf{x}_{N+2} = \mathbf{x}'' \big] - \max_{\mathbf{x}' \in \mathbf{X}_{\text{alt}}} \mu^{\text{fused}}(\mathbf{x}'). \quad (2.16)$$

It is noted that to compute the expectation in Eq. (2.15), a Monte Carlo approach is used, drawing N_q independent samples from the normal distribution of the GP of 'information source' i at a design point $\mathbf{x}$, $f_i^q(\mathbf{x}) \sim \mathcal{N}\left(\mu_i(\mathbf{x}), \sigma^2_{GP,i}(\mathbf{x})\right),\ q = 1, \ldots, N_q$. Then, by temporarily augmenting $(\mathbf{x}\,,\ f_i^q(\mathbf{x}))$, one at a time, using the available samples of 'information source' i, the mean of the fused GP is temporarily updated, which is denoted as $\mu^{\text{fused},q}_{\mathbf{x},i}$, and the utility is approximated as

$$U_{\mathbf{x},i} \approx \frac{1}{N_q} \sum_{q=1}^{N_q} \big(\max_{\mathbf{x}' \in \mathbf{X}_{\text{alt}}} \mu^{\text{fused},q}_{\mathbf{x},i}(\mathbf{x}') + \max_{\mathbf{x}'' \in \mathbf{X}_{\text{alt}}} EI^q_{\mathbf{x},i}(\mathbf{x}'') \big), \quad (2.17)$$

where $EI^q_{\mathbf{x},i}(\mathbf{x}'')$ is the one-step look-ahead expected increase in the maximum of the fused GP upon augmentation of query $(\mathbf{x}\,,\ f_i^q(\mathbf{x}))$ to 'information source' i. This expected increase is computed using the Knowledge Gradient (KG) metric over the temporary fused GP as discussed in [48].

Using the Latin Hypercube sampling over the input space, the utility function for each of the 'information sources' is evaluated by removing the previously added sample and augmenting the next sample in the proposed alternatives. The next point to query—among all the candidate points—with the best 'information source' is determined using the following policy:

$$(i_{N+1}, \mathbf{x}_{N+1}) = _{i\in[1,\ldots,S],\mathbf{x}\in\mathbf{X}_{alt}} \frac{U_{\mathbf{x},i}}{C_{\mathbf{x},i}}, \tag{2.18}$$

where $C_{\mathbf{x},i}$ is the cost of querying 'information source' i at a design point $\mathbf{x}$.

Once the selected design point has been identified and a query has been made, the corresponding fused GP is updated. This loop is continued until the objective of the optimization problem has been met or the budget allocated to this optimization task has been exhausted:

$$\mathbf{x}^* = _{\mathbf{x}\in\chi} \mu^{\text{fused}}(\mathbf{x}). \tag{2.19}$$

A schematic of the framework just described is shown in Fig. 2.4.

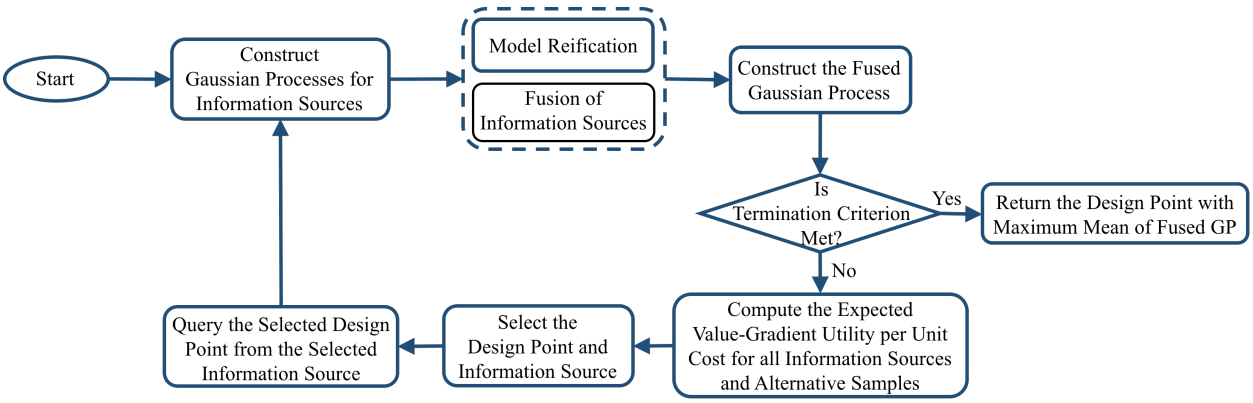

Figure 2.4: Flow chart of the proposed efficient multi-'information source' optimization framework.

2.3 Results and Discussion

2.3.1 Designing Dual-Phase Microstructures for Enhanced Mechanical Performance

The framework, Fig. 2.4, is now demonstrated against the problem of identifying the phase constitution –represented in this simplified instance as just the volume fraction of the constituents in the dual-phase microstructure–that results in the maximum formability metric. The microstructure-based finite element calculations are considered as 'ground truth' and the three reduced-order models and three micromechanical homogenization schemes as used as the cheap 'information sources' available to elicit the behavior of the composite dual-phase microstructure.

The optimization process starts by querying (once) the cheap and the 'ground truth' sources. These data are then used to construct the initial GPs used to emulate each of the 'information sources'. The framework is then used to identify which 'information source' to use next, and where in the input space to use it.

Here, after five queries to any of the cheap sources the framework makes the recommendation for the next point to query using the expensive 'ground truth'. Note that the framework allows for the querying of any of the cheap sources multiple times (or not at all) as long as the five-query budget has not been exhausted. Also note that while the cost is considered in the construction of the utility function, the total expenditure (i.e. total computational resources used) is not accumulated. Implicitly, this set up thus considers that there is no real hard budget constraining the optimization. This problem setup will be contrasted with a case in which there is a hard budget constrain for the total computational expenditures before a query to the 'ground truth' is made, as described later in Section 2.3.2.

Fig. 2.5 shows the fused model obtained by the approach, with mean represented by the smooth red line and 99.7% confidence interval represented by the red shaded area. These results are compared to the 'ground truth', represented with the jagged green line and the green shaded area. As it can be seen, the fused model obtained by this approach represents the 'ground truth' well in the region of the optimal design.

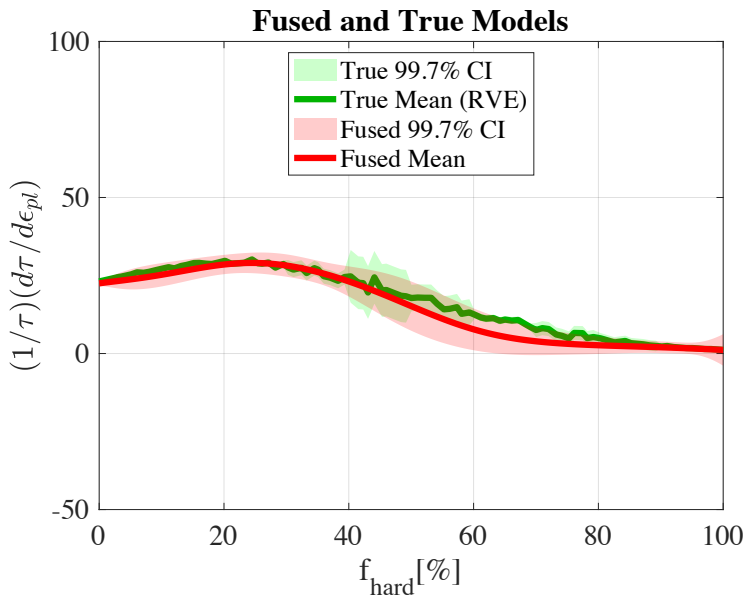

Figure 2.5: The mean and 99.7% CI of the fused model obtained by the proposed approach in comparison with the 'ground truth' (RVE).

Table 2.3: Performance of the optimization framework. The true optimal solution as obtained by the microstructure-based finite element calculation (RVE) is $(\mathbf{x}^*\,,\, f^*) = (21.6080\;,\;29.3123)$.

Experiment	$\mathbf{x}^*_{fused}$	f^*_{fused}	$f_{true}(\mathbf{x}^*_{fused})$
2	36.1809	18.8470	25.4273
3	36.6834	20.7475	25.1903
4	32.1608	22.5232	27.1322
5	31.6583	28.9564	27.3177
6	26.1307	29.8824	28.8633
7	22.6181	29.7564	29.2840

Table 2.3 shows the progression of the optimization procedure as the framework identifies the design point that corresponds to maximum formability. The table compares the predictions from the fuse model evaluated at the best design point thus far, $\mathbf{x}^*_{fused}$, with the value of the formability parameter evaluated using the 'ground truth' at the same best design point. The table shows that it takes seven queries of the 'ground truth' to produce a close-to-optimal solution. While it is not reported here, but in the works of [13] its is shown how this multi-'information source' framework is superior to the use of the 'ground truth' as the only query to sample.

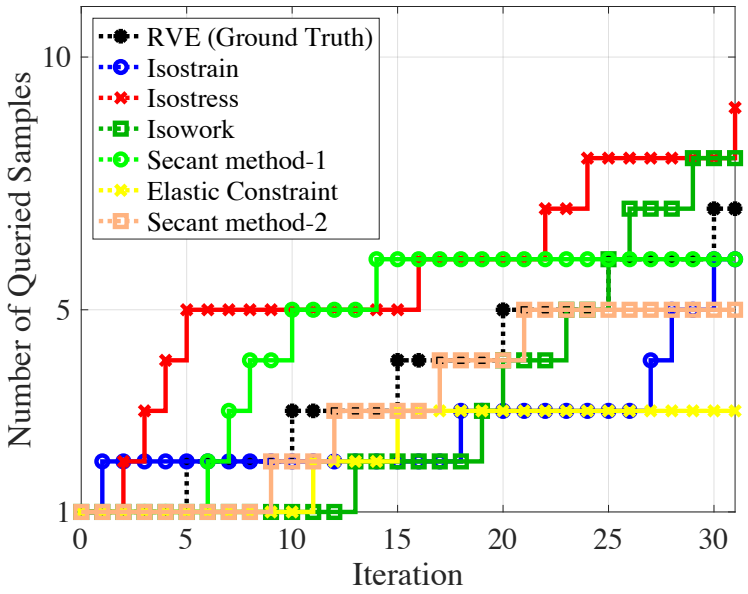

Figure 2.6: Number of queries as a function of the experimental sequence for all 'information sources'.

Fig. 2.6 shows the number of times that any of the 'information sources', including the expensive 'ground truth', are queried. Between each of these expensive queries, the different cheap 'information sources' are queried depending on their utility (including consideration of their cost). The figure shows that all the cheap sources are being queried, albeit at different frequencies, in order to identify the optimal design. As described above, the querying policy is controlled through Eq. (2.18), which balances improvement in objective with cost. The figure shows, for example, how in the early stages of the optimization the 'isostress' and 'secant method-1' sources tend to be queried more extensively than the other four available sources. In later stages of the process it is evident that many more sources are being queried and this serves as an indication of the ability of the present framework to optimally select the most cost effective 'information sources'. It is also pointed out here that very cheap 'information sources', such as the isostress and isostrain models, could potentially be queried exhaustively and still follow the policy determined by Eq. (2.18). In this case, the cost of querying is so negligible that any potential for objective improvement would lead to these sources being selected. This is an excellent feature of the policy, since in general,

if there is access to a very inexpensive ‘information source’, it makes intuitive sense to quickly gather all information that one can from it.

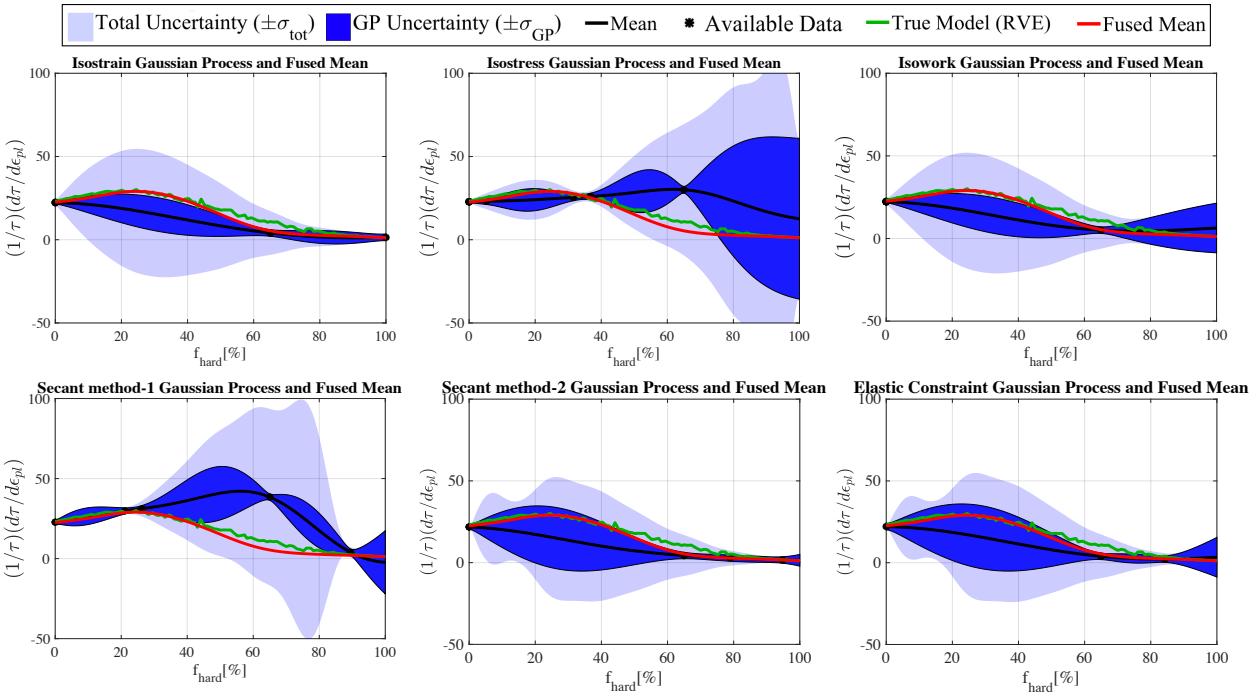

Figure 2.7: Comparison between the ‘ground truth’, fused model, and individual ‘information sources’.

Fig. 2.7 shows the GPs of the ‘information sources’. The black dots show the samples queried from the ‘information sources’ and the black lines represent the mean function of these sources. The solid shaded regions for each of the GPs correspond to the intrinsic uncertainty of the GPs themselves and originates from the lack of information about the response of that particular source in regions not explored yet. In addition to this uncertainty, a comparison with the response of the ‘ground truth’ is used to compute the discrepancy of the ‘information sources’. The intrinsic uncertainty of the GP and the discrepancy between the ‘information source’ and the ‘ground truth’ are added into the total uncertainty, shown as a lighter shaded region.

The figure shows that none of the ‘information sources’ performs well over the entire design domain. Some sources overstimate their predictions relative to the ‘ground truth’ (black solid line)

while some sources underestimate it. None of the sources provides even a qualitative indication of where the optimal value of the 'ground truth' should be. The application of the reification-based information fusion, however, results in a fused model that reproduces, with high fidelity, the response of the 'ground truth'.

Fig. 2.6 shows that different sources are queried at different stages of the optimization sequence. Moreover, Fig. 2.7 shows that while all sources have a significant discrepancy with the 'ground truth', some sources tend to be closer to it in some regions of the problem space. To understand how different sources were correlated to the 'ground truth', the effective independent 'information sources' (EIS) index is presented in Fig. 2.8. This index was introduced first time in the work of [13], and can be understood as a metric that indicates the number of effective number of independent 'information sources' used to estimate the fused model at different regions of the domain. If $\sigma_*^2(\mathbf{x})$ is defined as the variance of the current best 'information source' at point $\mathbf{x}$, the number of effective independent 'information sources' with variance $\sigma_*^2(\mathbf{x})$ at the point $\mathbf{x}$ is given as

$$I_{\text{eff}} = \sigma_*^2(\mathbf{x})\mathbf{e}^\top \tilde{\Sigma}(\mathbf{x})^{-1}\mathbf{e}. \tag{2.20}$$

The index shows the total number S of effective independent sources with the same variance at a given design point. Any source that has a variance larger than the variance of the best source(s) will not contribute to the reduction of the variance and its value, I_{eff}, will be less than S. The EIS index is thus calculated relative to the best source available at any given point. In the case of highly correlated 'information sources' Eq. (2.9) can result in a decrease in variance that is larger than in the case of statistically uncorrelated 'information sources'. The reification approach used in this work takes this into account by detecting the correlation and discounting this effect appropriately. It is noted that if these highly correlated sources were to be treated as statistically independent, they would have undue evidence on the overall estimation of the fused model.

Fig. 2.8 includes the I_{eff} for all the cheap sources simultaneously and compares this index against that of the isostress + secant method-1 pair and the combination of the isostrain + isowork + secant method-2 + elastic constraint. As can be seen in Fig. 2.8, I_{eff} is not large over the input

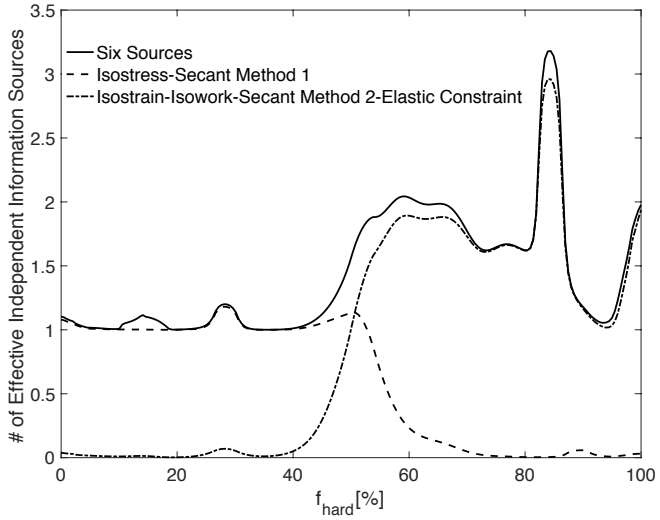

Figure 2.8: Number of effective independent 'information sources' (EIS), I_{eff} as a function of f_{hard}.

space. For this particular problem, it is often the case that only a few of the sources are reasonable estimates of 'ground truth' at any given location in the domain. This renders the contribution of the other more inaccurate sources to I_{eff} to be very small. In this figure, it is clear that initially, until $f_{\text{hard}} \approx 40\%$, the isostress + secant method-1 pair is driving the fused approximation, which is clear from the fact that the six-source index and the isostress + secant method-1 index nearly overlap in this region. This means that the isostress + secant method-1 are capable of explaining most of the variance with regards to the 'ground truth'. Examining Fig. 2.7 one can see that these two sources are closer to the 'ground truth' than the other four sources within this region of the input space. At the other end of the domain, the other four sources are contributing more to the prediction, which can again be seen from the near overlap with the six-source index and the drop-off of the isostress + secant method-1 pair. While all 'information sources' do not contribute equally over the domain, they are all necessary to construct the fused approximation shown in Fig. 2.5.

This result is significant as I_{eff} essentially indicates what 'information source' (or model) operates in a specific region of the problem domain. Thus, it is possible to use I_{eff} to uncover the relevant sources and, indirectly, the relevant physics governing the behavior of a system in different regimes. In this case, for example, I_{eff} suggests that the assumption of equal partitioning of

stress in the regime at low volume fraction of the hard particle seems to be operationally correct. At higher volume fractions of the hard phase, other theories may be more in agreement with the 'ground truth'.

2.3.2 The Impact of Cost on Optimal Decision Making under Budget Constraints

It is noted that the set up of the test problem presented in Section 2.3 was somewhat arbitrary as the acquisition protocol (five queries to the cheap sources before querying the 'ground truth') is defined ahead of carrying out the exploration/exploitation of the design space. In principle, the cheap sources could have been chosen to query any number of times in between queries to the 'ground truth'. More importantly, while cost was used to compute the utility metric of the design space, there was no explicit consideration of budget available during the optimization exercise.

To resolve this issue, a more realistic situation that is more relevant to the process of optimal experimental design for materials optimization is considered:

- There is a finite set of 'information sources' that can be queried at any given time in order to learn more about the problem space.
- Each of the sources has different degree of fidelity with regards to the 'ground truth' and, most importantly, different cost.
- There is a finite budget, expressed in terms of total cost (in this case in computational time) available to explore and exploit the domain space before the 'information source' considered as the 'ground truth' is queried.

In order to demonstrate the effect of cost in the decision-making process, the average results obtained over 100 independent simulations in two conditions—labeled as 'with cost consideration' and 'without cost consideration'—are compared in Fig. 2.9. In both conditions, a fixed budget (computational cost) of 100 seconds to be spent among all the cheap 'information sources' before querying the 'ground truth' is considered.

In the case identified as 'with cost consideration', the actual cost of 'information sources' in the selection criterion in Eq. (2.18) is considered, however in the case of 'without cost consideration',

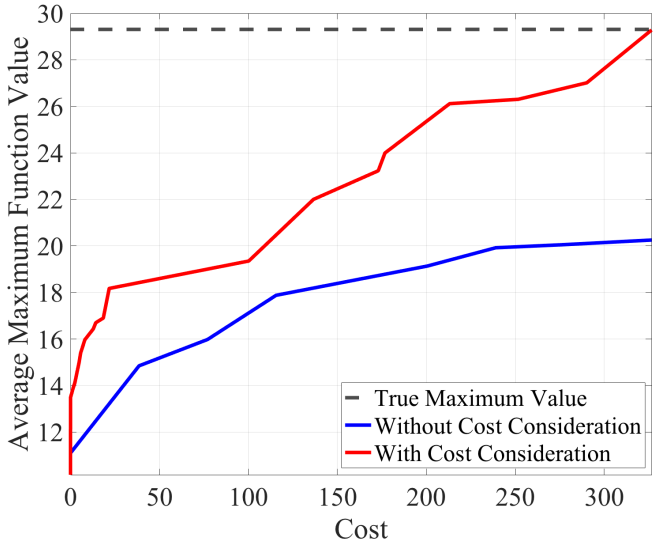

Figure 2.9: Average maximum function value per cost for cases of decision-making with and without cost consideration.

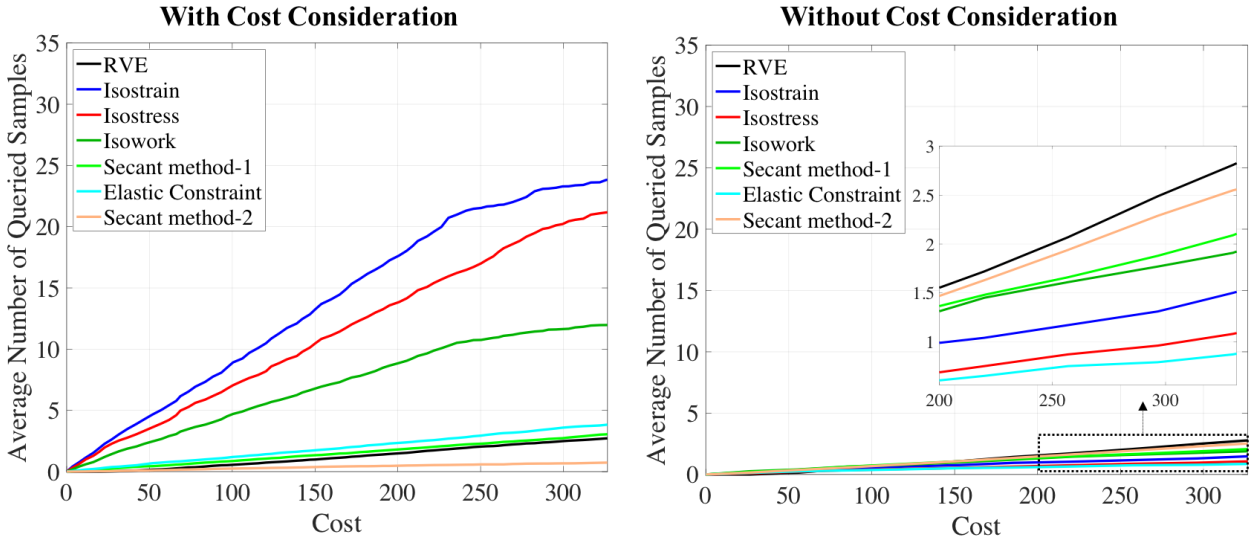

Figure 2.10: Average Number of samples queried from the 'ground truth' (RVE) model and the 'information sources' over average cost for the cases of decision-making with and without cost consideration.

the cost of all 'information sources' are assumed to be the same during the selection process. After the budget of 100 seconds is spent, then the 'ground truth' is queried in both cases.

In the first case (with cost consideration), the cheap 'information sources' are queried exhaustively allowing the policy to obtain all available information from the very inexpensive sources with almost negligible cost. After this, the more expensive sources are queried according to the balance between cost and utility, in a fully automated fashion. While in the second case (without cost consideration), as cost accumulation does not play a role in the selection process, the expensive 'information sources' are queried in the early iterations. Therefore, fewer queries are performed, particularly on the cheaper 'information sources', in the limited budget of 100 seconds. The result is that the total budget is exhausted before reaching the optimum. However, for the 'with cost consideration case', the optimum is obtained.

Fig. 2.10 demonstrates the average number of queries to each 'information source' and the 'ground truth' over average cost for two conditions of with and without cost consideration. As can be seen, in the case of 'with cost consideration', the cheaper 'information sources' are exhaustively queried, which helps to find the optimum with much less average cost in comparison to the case of 'without cost consideration' as seen in Fig. 2.9. Essentially, the policy in place has the ability to quickly gather all information from the negligible expense sources prior to making a query to a more expensive source. This provides for more informed queries to the more expensive sources, and also matches with the intuitive concept of exhaustively evaluating the very inexpensive sources immediately.

2.4 Summary

While there has been real progress in the development of ICME-based frameworks for materials design, major issues still remain. The challenges are closely associated to the resource-intensive nature of the computational and/or experimental approaches to exploring PSPP relationships as well as to the fact that most ICME frameworks tend to assume that there is a single model or experiment available at a given scale or PSPP linkage. A further limitation of traditional ICME approaches is the fact that in most cases there is no prescribed way to correct for discrepancies between models and 'ground truth'.

In this work, a framework capable of utilizing multiple available sources of information to

carry out a materials optimization task is presented. By exploiting statistical correlations among the different 'information sources' as well as between the sources and the 'ground truth' it is possible to develop a fused model that incorporates the available (useful) information originating from all of the sources. The fused model is represented as a GP and is thus amenable to Bayesian Optimization. Here the Knowledge Gradient (KG) metric is used to efficiently balance the need to explore and exploit knowledge of the materials design space in order to find an optimal solution in as efficient manner as possible. The framework, however, goes beyond optimal experimental design and enables the selection of the most cost-effective 'information source' to use every time that there is need to query the problem space, while accounting for a total available budget.

While the proposed framework has been demonstrated by using a combination of relatively inexpensive computational models, it is important to note that each 'information source' (including the 'ground truth') is represented as a stochastic model (i.e., a GP) and thus there is no fundamental limitation to using experimental or any other type of information as an independent 'information source'. One could, for example, combine mechanistic models, machine learning derived non-parametric models, experiments at different degrees of resolution, and even expert opinion as long as each source is modeled as a GP or any other suitable stochastic representation. The framework proposed thus provides a natural approach to seamlessly combining experiments and simulations, and hopefully will inspire and instigate future works in this direction.

3. IMPORTANCE OF MICROSTRUCTURE IN MATERIAL DESIGN

3.1 Introduction

The future of technologies such as efficient jet engines [49], hypersonic flights [50] and next-generation nuclear reactors [51] rests on our ability to design and discover new materials with desired properties. Although historically, discovery of new materials has relied on the Edisonian approach, it is doubtful that this approach will serendipitously yield new materials to meet the current and futuristic technological needs. Thus, to overcome this challenge, materials scientists have advocated a goal-oriented exploration of the material design space through experimental, computational, and/or data-driven methods [1, 2, 3]. Essentially, the focus of a material design process is to predict the combinations of material chemistry and processing route that yields a material with targeted properties. The goal-oriented material design approach is enabled by understanding and exploiting processing/chemistry - microstructure - property (PSP) relationships, whose existence represents the central paradigm in materials science (Fig. 3.1). In this approach, a material is treated as a complex hierarchical system ultimately described by linkages along the PSP chain [1, 2, 3, 4]. The established PSP chain is then exploited to tune the processing/chemistry space to yield target properties [3, 52, 53, 54, 55, 56, 57, 9]. While the exploitation of full PSP relationships is posited as an essential element of materials design and discovery, microstructure information is only used to carry out sophisticated multiscale simulations to establish the PSP relationships. So that, fundamentally, the material design process is *microstructure agnostic* i.e., does not explicitly exploit the microstructure information but only explores the direct processing/chemistry - property relationships (Fig. 3.1).

Indeed, even the state-of-the-art experimental materials design are carried out through direct exploration of the materials processing/chemistry space to arrive at optimal properties without explicitly exploiting the knowledge of the microstructure state of the material [15, 16, 17, 18]. For example, the authors in ref. [15], experimentally designed a refractory high-entropy alloy with

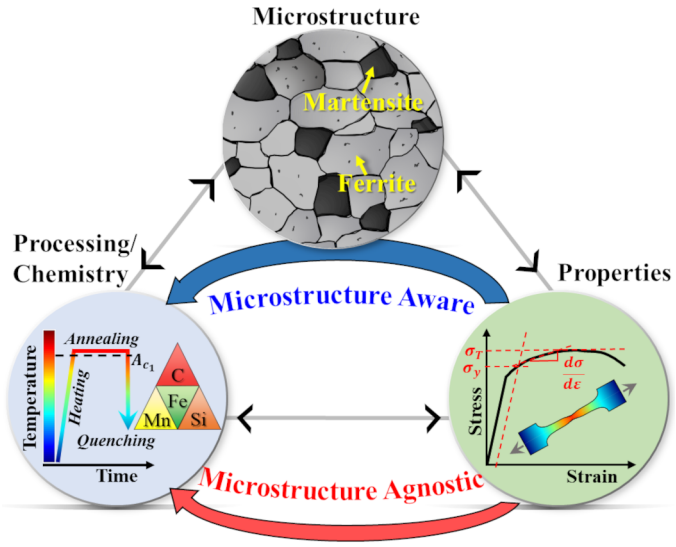

Figure 3.1: Processing/Chemistry-Microstructure-Property (PSP) paradigm in materials science. In the traditional, *microstructure agnostic*, approach the microstructure information is not directly exploited for material design, as shown. While in the proposed *microstructure aware* approach the microstructure information is directly exploited for material design, and it is shown that this *microstructure aware* approach helps us arrive at processing/chemistry conditions that yield optimum properties more efficiently than the traditional *microstructure agnostic* approach.

enhanced ductility by optimizing the material's chemistry. Here, microstructure characterization was only used to gain understanding and rationalize the impact of processing/chemistry on the mechanical properties of the alloy *a posteriori* but was not explicitly used to guide the step-by-step exploration of the material design space i.e., processing/chemistry. Similarly, the authors in ref. [16], experimentally designed a high-strength, low-cost nanostructured beta-titanium alloy consisting of homogeneous distribution of micron- and nano-scale α-phase precipitates within the β-phase matrix. Again, as in the previous case, analysis of the microstructure, after finding an optimal property, was used to uncover the ultimate cause for the superior mechanical properties. Another example of such efforts includes the work by authors in ref. [17], who were able to identify alloys defeating the strength-ductility trade-off by forming a dual-phase microstructure by engineering the phase metastability. In this case, the alloy design principle was based on a hypothesized enhancing mechanism verified, *a posteriori*, via experimental characterization.

While the examples just described expanded our knowledge of the materials performance space

by careful and ground-breaking analysis of the connections between processing/chemistry and resulting properties mediated by the material microstructure, the latter was not used as a direct input in the material design process. Rather, an analysis of the material microstructure state was carried out to explain the attained properties. Thus, even though our aspiration as material scientists is to unravel the principles that govern material properties and performance, from the practical engineering standpoint, explicit knowledge of the microstructure does not appear to be a necessary condition for a successful material design campaign. However, given the centrality of the PSP relationships to materials science as a field, it is worth investigating whether microstructural information can help us arrive at processing/chemistry conditions that yield optimum properties more efficiently than otherwise. If the answer ends up being negative, then, from an admittedly pragmatic point of view, the argument for building an explicit PSP relationship as a necessary condition towards accelerated material design is moot. The microstructure state of the system, thus, can be simply replaced by a 'black box' without affecting the outcome of the design process i.e., identification of the region in the material design space (processing/chemistry parameters) that yields optimal properties. Knowledge of the microstructure then will only serve to rationalize observations rather than assist in the decision-making process as one navigates the material design space. On the other hand, showing that microstructure information can be explicitly exploited to accelerate the material design process can have significant consequences in recent efforts to develop closed-loop iterative frameworks for material design [57, 9].

Herein, a rigorous analysis is carried out to probe the importance (if any) of the microstructure information in the material design process. The specific material design problem considered here involves finding the right combinations of material chemistry and processing conditions that maximizes the targeted mechanical property of a model dual-phase steel. The material design problem is first solved by following the traditional *microstructure agnostic* (Fig. 3.1) approach where the material design space includes the material chemistry and processing routes, and the microstructure information is only used to carry out multiscale simulations to establish PSP relationships. Next, the same material design problem is set up by following a novel *microstructure aware* (Fig. 3.1)

approach where the material design space not only includes the material chemistry and processing routes, but also the microstructure information. Note that apart from the explicit incorporation of the microstructure information in the materials design space in the latter, the two approaches are essentially the same. Nevertheless, incorporating the microstructure information in the material design space is not a trivial task. This is because, first, the microstructure information is a dependent variable as it depends on the independent variables– material chemistry and processing routes. Second, explicit incorporation of the microstructure information in the material design space increases the dimensionality of the problem. Here not only for the first time it is shown how to formulate and solve a *microstructure aware* material design problem but also the fundamental question i.e, whether microstructure information is important in the material design process or not is answered. The results clearly show that explicit incorporation of the microstructure information in the material design space significantly accelerates the material design process. Thus, knowledge of the microstructure not only rationalizes the observed properties but also assists in the decision-making process as one navigates the material design space. This *microstructure aware* closed-loop iterative material design framework can also be put into practice even for an entirely experimental material design campaign by using ever-growing high-throughput material processing and characterization techniques.

3.2 Methods

The importance of the microstructure information in the material design process is probed by considering a model material design problem that involves finding the right combinations of the parameters in the input (design) space, $\mathbf{X_I}$, that maximizes the output (objective), $\mathbf{X_O}$, Fig. 3.2. The input space in this problem includes the processing condition (intercritical annealing temperature, T_{IA}) and the material chemistry (the amount of alloying elements, Carbon, X_C, Silicon, X_{Si}, and Manganese, X_{Mn}); while the output is a targeted mechanical property (stress normalized strain hardening rate, $(1/\tau)\,(d\tau/d\varepsilon_{pl})$, with τ and ε_{pl} being the flow stress and the plastic strain, respectively) of a model (ferritic-martensitic) dual-phase steel. The targeted mechanical property, normalized strain hardening rate, is a useful mechanical performance metric, and a higher value of

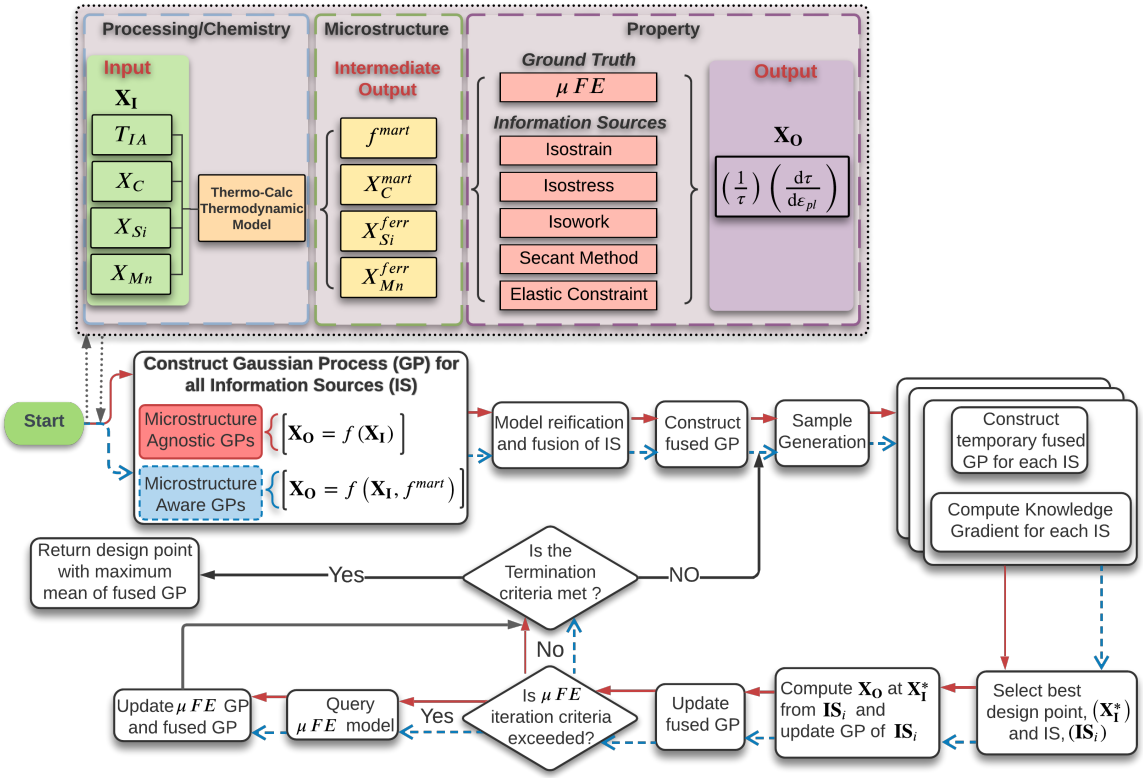

Figure 3.2: Schematic representation of the *microstructure agnostic* and *microstructure aware* closed-loop multi-information source fusion Bayesian Optimization approaches for the design of a model dual-phase (ferrite-martensite) steel. Here, $\mathbf{X_I}$ is the set of input variables with T_{IA} being the intercritical annealing temperature, X_C, X_{Si} and X_{Mn} being the Carbon, Silicon and Manganese content, respectively, while the targeted output, $\mathbf{X_O}$, is the stress normalized strain hardening rate $((1/\tau)\,(d\tau/d\varepsilon_{pl})$, with τ and ε_{pl} being the flow stress and the plastic strain, respectively). Also, f^{mart} is the volume fraction and X_C^{mart} is the Carbon content of the martensite phase; while X_{Si}^{ferr} and X_{Mn}^{ferr} are the Silicon and Manganese content, respectively, of the ferrite phase.

this parameter indicates better ductility and formability of the material. The feasible input space in the design problem is considered to be bounded i.e., we consider a material system that contains Carbon within 0.05 to 1 wt%, Silicon within 0.1 to 2 wt% and Manganese within 0.15 to 3 wt%, and is subjected to intercritical annealing heat-treatment at temperatures ranging from 650°C to 850°C.

Next, computational thermodynamics is employed using a commercial code Thermo-Calc™ as in refs. [58, 9] to compute the microstructure (characterized by the volume fraction, f^{mart}, of the martensite phase) and chemical composition (characterized by the Carbon content of the marten-

site phase, X_C^{mart}, and Silicon, X_{Si}^{ferr}, and Manganese, X_{Mn}^{ferr}, content of the ferrite phase) of the resultant phases as a function of $\mathbf{X_I}$, Fig. 3.2. The details of the dual-phase microstructure are then used to predict the mechanical properties using five low fidelity reduced-order micromechanical models, Isostrain, Isostress, Isowork, Secant Method and Elastic Constraint, referred to as 'information sources' and a high fidelity three-dimensional microstructure-based finite element model (μFE) referred to as the 'ground truth' (Fig. 3.2) [59, 9]. The first three low fidelity reduced-order mechanical models, Isotrain [38], Isostress [39] and Isowork [40], are based on different simplifying assumptions of how the strain, stress, or mechanical work, respectively, partition among the constituent phases in the dual-phase microstructure. The other two low fidelity models, the Secant Method and the Elastic Constraint models, are more sophisticated micromechanical models ref. [41]. The Secant Method is based on Hill's weakening constraint power in a plastically-deforming matrix; while the elastic constraint model is based on Kröner's treatment of the matrix-inclusion system under elastic constraints [41]. The 'ground truth' μFE model on the other hand utilizes a full field finite element analysis of a three-dimensional representative volume element (RVE) of the dual-phase microstructure [60, 13, 59, 9]. A typical finite element mesh of the RVE of the dual-phase microstructure employs 27,000 C3D8 brick elements from the ABAQUS/standard element library [42], and is subjected to a monotonically increasing uniaxial tensile deformation under fully periodic boundary conditions. A more detailed description of the μFE model can be found in refs. [60, 9].

The two constituent phases, ferrite and martensite, are discretely modeled in the the μFE analyses as isotropic elastic-plastic material with Young's modulus, $E = 200GPa$ and Poisson's ratio, $\nu = 0.3$, and constitutive relations (relating flow stress, τ, equivalent plastic strain, ε_{pl}, and the chemical composition, X_i^P, in weight fraction) as,

$$\tau = \tau_0^F + C_{Si}(X_{Si}^{ferr})^{1/2} + C_{Mn}(X_{Mn}^{ferr})^{1/2} + K^F(\varepsilon^{pl})^{n^F} \tag{3.1}$$

and

$$\tau = \tau_0^M + C_c(X_C^{mart})^{1/3} + K^M(\varepsilon^{pl})^{n^M} \tag{3.2}$$

for the ferrite and martensite phases, respectively, with $\tau_0^F = 200$MPa, $C_{Si} = 732$MPa, $C_{Mn} = 213$MPa, $K^F = 2200$MPa, $n^F = 0.5$, $\tau_0^M = 400$MPa, $C_c = 10^5$MPa, $K^M = 450$MPa and $n^M = 0.06$. The choice of the (representative) constitutive parameters in Eqs. (3.1) and (3.2) are based on the prior observations that the strength of the martensite phase predominantly depends on its carbon content and it does not exhibit significant strain-hardening; while the ferrite phase is softer than the martensite phase, exhibits significant strain-hardening and its strength depends on its silicon and manganese content [23, 61, 62]. All the five (low fidelity reduced-order) micromechanical models referred to as 'information sources' also use the same constitutive relations given in Eqs. (3.1) and (3.2) for the two constituent phases.

As shown schematically in Fig. 3.2, the established PSP relationship for the model dual-phase material can now be exploited using the closed-loop multi-information source fusion (multi-fidelity) Bayesian Optimization (BO) framework as demonstrated in chapter 2 to solve the goal-oriented material design problem by either following the traditional *microstructure agnostic* or a novel *microstructure aware* approach. Here, the closed-loop multi-fidelity BO framework is briefly described with a focus on highlighting the differences between the proposed *microstructure aware* approach and the traditional *microstructure agnostic* approach. A more complete description of the closed-loop multi-fidelity BO framework can be found in chapter 2 and in ref. [9]. In the *microstructure agnostic* approach, the decision-making process does not involve the knowledge of the material's microstructure and the optimization problem is simply posed as

$$\mathbf{x}^* = \arg\max_{\mathbf{x}\in\mathbf{X_I}} \mathbf{X_o}\left(\mathbf{x}\right) \tag{3.3}$$

where $\mathbf{x}^*$ is the optimal design vector in the feasible input space, $\mathbf{X_I} = [T_{IA}, X_C, X_{Si}, X_{Mn}]$. In the proposed *microstructure aware* approach the material design space not only includes the material chemistry and processing condition, but also the microstructure information; and the

decision-making process explicitly involves the knowledge of the material microstructure and the optimization problem is posed as

$$\mathbf{x}^* = \arg\max_{\mathbf{x}\in\mathbf{X_I}} \mathbf{X_o}\left(\mathbf{x}, f^{mart}\left(\mathbf{x}\right)\right) \tag{3.4}$$

with f^{mart} being dependent on the input vector, $\mathbf{x}$.

The closed-loop multi-fidelity BO framework for both the approaches first involves construction of surrogate models for all the 'information sources' and 'ground truth' based on the current knowledge of the connection between the design space and the predicted response. Herein, a Gaussian process model with squared exponential kernel is used as surrogates for all the 'information sources' and 'ground truth.' The Gaussian process model is chosen due to their useful mathematical properties such as their ability to predict the mean value as well as the variance of the quantity of interest, and the straightforward manner in which the causal correlation between the points in the design space and their response can be modeled [63]. The behavior of a Gaussian process surrogate model is controlled by the hyperparameters of the kernel and it is necessary to tune their values based on the current knowledge of the input-output connection. The optimum values of the hyperparameters in this work are estimated by maximizing the log marginal likelihood. Note that the Gaussian process surrogate model for the *microstructure agnostic* approach correlates the input $\mathbf{X_I}$ to output $\mathbf{X_O}$; while for the *microstructure aware* approach the input $\mathbf{X_I}$ is augmented with an extra dimension which is the volume fraction of the martensite phase, f^{mart}, to explicitly incorporate the microstructure information in the materials design process.

Since all the 'information sources' i.e., the low fidelity reduced-order micromechanical models attempt to describe the connection between the microstructural features and the mechanical response of the material, it is expected that they would exhibit some degree of correlation among themselves and also with the 'ground truth' i.e., the μFE model. Thus, by exploiting such statistical correlations through the 'reification' process [45, 46, 47, 64] a fused Gaussian process model is generated. This fused Gaussian process model is used to estimate the objective function that encompasses our current knowledge of the correlation between the design space and the objective

value. In a multi-fidelity iterative design optimization problem, one needs to answer two questions at every iteration: (i) where to sample next in the design/input space, and (ii) which 'information source' to use to query the selected point in the design space. To determine this, potential sample design points are generated using Latin hypercube sampling in the input design space and evaluated from each of the Gaussian process models of 'information sources' and then a temporary fused Gaussian process model for each 'information source' is constructed. Next, among these potential design points, it is sought to identify which design point and 'information source' to query such that it will lead to the maximum improvement in the knowledge of the maximum objective value. To quantify the expected change in the knowledge of the maximum objective value when evaluating the potential design point from each 'information source,' an expected value utility acquisition function based on the Knowledge Gradient [65] is used. Next, the Knowledge Gradient for the set of potential design points on the temporary fused Gaussian process model of each 'information source' is computed. The best pair of 'information source,' $\mathbf{IS_i}$ and design point, $\mathbf{X_I^*}$ that maximizes this Knowledge Gradient is selected to query next. Following this, the response of the selected 'information source,' $\mathbf{IS_i}$, by computing the input-output correlation at the selected design point, $\mathbf{X_I^*}$ is evaluated. After this evaluation of the selected 'information source,' $\mathbf{IS_i}$, the corresponding Gaussian process and fused Gaussian process models are updated. Now based on a criteria, the 'ground truth' model (μFE model) may also be queried to update the knowledge of the maximum objective value. The criteria to query the 'ground truth' model is set here to every ten design iterations. Using this evaluation of the 'ground truth' model, the Gaussian process model of the 'ground truth' as well as the fused Gaussian Process model are updated. This entire process is repeated until the end of the optimization is reached which in this case is a preset number of design iterations. Finally, at the end of the optimization, the best design point that maximizes the objective function is reported.

3.3 Results

The material design problem of finding the right combinations of the parameters in the input space, $\mathbf{X_I} = [T_{IA}, X_C, X_{Si}, X_{Mn}]$, that maximizes the output, $\mathbf{X_O} = [1/\tau\,(d\tau/d\varepsilon_{pl})]$, of a

model dual-phase steel is solved using the closed-loop multi-fidelity BO framework following both the traditional *microstructure agnostic* and the novel *microstructure aware* approaches, as shown schematically in Fig. 3.2. The first step to set up the design framework requires construction of Gaussian process models using the initial knowledge of the $\mathbf{X_I}$-$\mathbf{X_O}$ correlation. To this end, $\mathbf{X_I}$-$\mathbf{X_O}$ correlation at ninety sets of randomly selected parameters in the input space using computational thermodynamics and each of the low fidelity micromechanical models referred to as 'information sources' are evaluated. While the $\mathbf{X_I}$-$\mathbf{X_O}$ correlation is evaluated at only five sets of randomly selected parameters in the input space using computational thermodynamics and the high fidelity μFE model referred to as 'ground truth.' To avoid any bias in the design process due to the initial sets of randomly selected parameters in the input space, in particularly that of the five sets evaluated using the 'ground truth' model, five realizations of the design process are carried out. A realization here basically refers to different sets of initially known five 'ground truth' $\mathbf{X_I}$ - $\mathbf{X_O}$ correlations.

The overall performance of the two material design approaches are compared in Fig. 3.3. The plot in Fig. 3.3(a), compares the maximum objective value (i.e., the stress normalized strain hardening rate) achieved as a function of the number of design iterations for five realizations of the design process; while the plot in Fig. 3.3(b) compares the average number of design iterations required to reach an average maximum objective value over five realizations of the design process. In Fig. 3.3(a), the lines correspond to the average values and the shaded regions represent the variance over the five realizations of the design process. As can be seen in Fig. 3.3(a), at any design iteration the maximum objective value achieved using the *microstructure aware* approach is greater than that using the *microstructure agnostic* approach. An alternate representation of the same in Fig. 3.3(b) also shows that on average much fewer number of design iterations are needed to obtain the same average objective value using the *microstructure aware* approach compared to the *microstructure agnostic* approach. Furthermore, even though after large number (greater than 150) of design iterations the predictions of the *microstructure agnostic* approach tends to catch up with that of the *microstructure aware* approach, the maximum objective value achieved

by the *microstructure agnostic* approach at the end of the optimization (i.e., after 300 design iterations) is less than the value achieved by the *microstructure aware* approach. Thus, the results presented here clearly demonstrates that an explicit incorporation of the knowledge of the material microstructure in the design framework not only accelerates the material design process but also results in comparatively better design solutions.

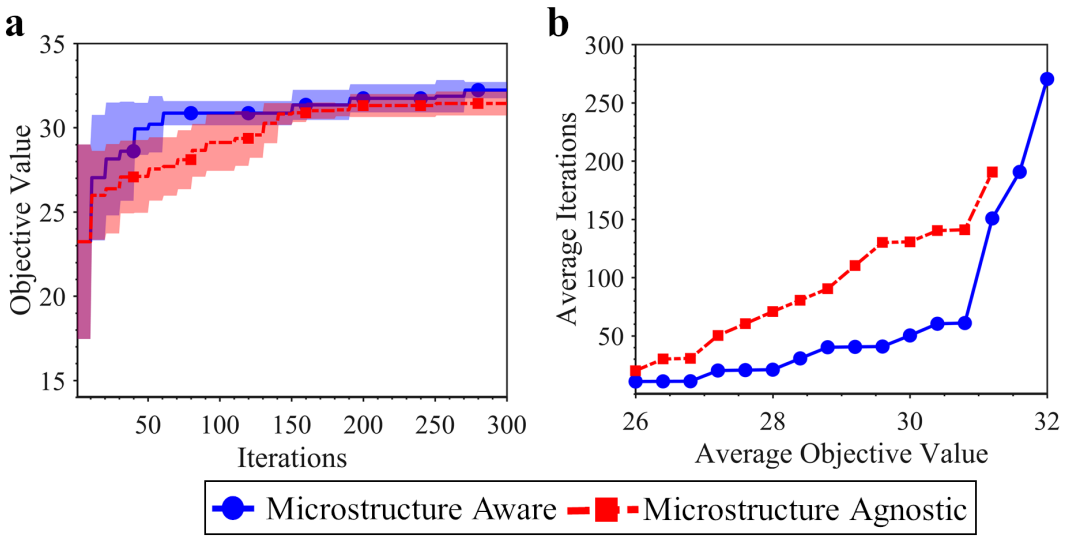

Figure 3.3: A comparison of the performance of the traditional *microstructure agnostic* and the novel *microstructure aware* material design approaches. (a) Comparing the maximum objective value found as a function of the number of design iterations for five realizations of the design process. (b) Comparing the average number of design iterations required to reach an average maximum objective value over five realizations of the design process.

Since the mechanical properties of a material are inherently controlled by the microstructure, analysis of how the two design approaches explore and converge in the material microstructure space during the design process is now shown. A comparison of the average value of the microstructural parameter i.e., volume fraction of the martensite phase, f^{mart}, that correspond to the average maximum objective value at each design iteration over five realizations of the design process as predicted by the *microstructure agnostic* and *microstructure aware* design approaches are

shown in Fig. 3.4. As can be seen in the figure, even though both the design approaches start the design process with the same knowledge of the $\mathbf{X_I}$-$\mathbf{X_O}$ correlation, the value of f^{mart} predicted by the two approaches during early stages of the design process are very different. The *microstructure agnostic* approach initially predicts a very small value of f^{mart} which then evolves as the design process/iteration continues and finally tends to saturate after a large number (greater than 150) of design iterations. On the contrary, the *microstructure aware* approach predicts a value of f^{mart} that is close to the saturation value of f^{mart} predicted by the *microstructure agnostic* approach since the beginning of the design process. This early knowledge of the feasible material microstructure space that corresponds to the maximum objective value enables the *microstructure aware* approach to be more efficient than the traditional *microstructure agnostic* approach.

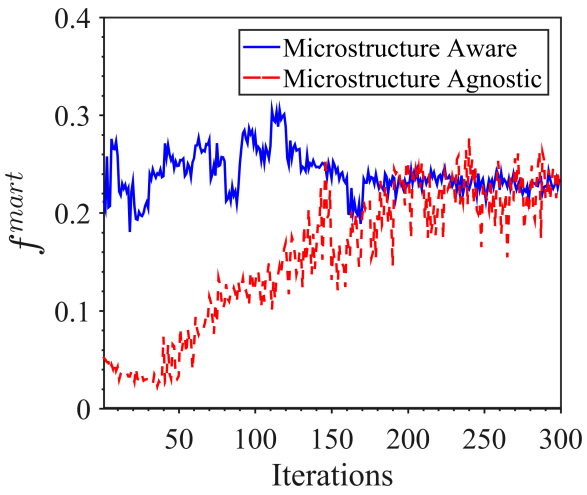

Figure 3.4: A comparison of the average value of the optimum microstructure parameter (characterized by the volume fraction of the martensite phase, f^{mart}) predicted by the traditional *microstructure agnostic* and the novel *microstructure aware* material design approaches at each design iteration over five realizations of the design process.

Next, the average values of the design (i.e., input) variables, intercritical annealing temperature, and the amount of alloying elements, Carbon, Manganese and Silicon that correspond to the average maximum objective value at each design iteration over five realizations of the design process as identified by the *microstructure agnostic* and *microstructure aware* design approaches

is compared in Fig. 3.5. In this particular problem, it is noted that irrespective of the design approach, the framework is expected to converge into a region rather than a unique point. This is because a particular objective value i.e., normalized strain hardening rate can be achieved by more than one combination of the processing condition and chemical composition [9]. As can be seen in Fig. 3.5, although the two design approaches are trying to maximize the same objective, they follow different routes and also on average converge to different set of parameters in the design space. For example, both *microstructure aware* and *microstructure agnostic* approaches identify similar intercritical annealing temperature in the early stages of the design process but the *microstructure aware* approach explores more in this design space in search of the optimum solution and finally converges to a lower value compared to the *microstructure agnostic* approach. On the contrary, the two approaches identify very different amount of the Carbon content in the early stages of the design process and the *microstructure agnostic* approach explores more in this design space in search of the optimum solution but finally converges to a value close to what is identified by the *microstructure aware* approach. Both the approaches, however, on average follow a similar route and also finally converge to a rather similar value of the amount of Manganese. While both the approaches identify similar amount of the Silicon content in the early stages of the design process, the *microstructure agnostic* approach explores more in this design space and finally converges to a lower value compared to the *microstructure agnostic* approach.

Our closed-loop multi-fidelity BO framework employs multiple 'information sources' to estimate the objective as described in Fig. 3.2. Thus, we now analyze the impact of the *microstructure aware* and *microstructure agnostic* design approaches on the selection of different 'information sources' during the design process. Note that none of the five low fidelity reduced-order micromechanical models referred here as 'information sources' are capable of reproducing the response predicted using the high fidelity μFE model referred here as 'ground truth' over the entire microstructure space [59]. Also recall that the criteria to query the 'ground truth' model is set here to every ten design iterations for both the design approaches. The results presented in Fig. 3.6 show the progression of queries made to different 'information sources' as function of design it-

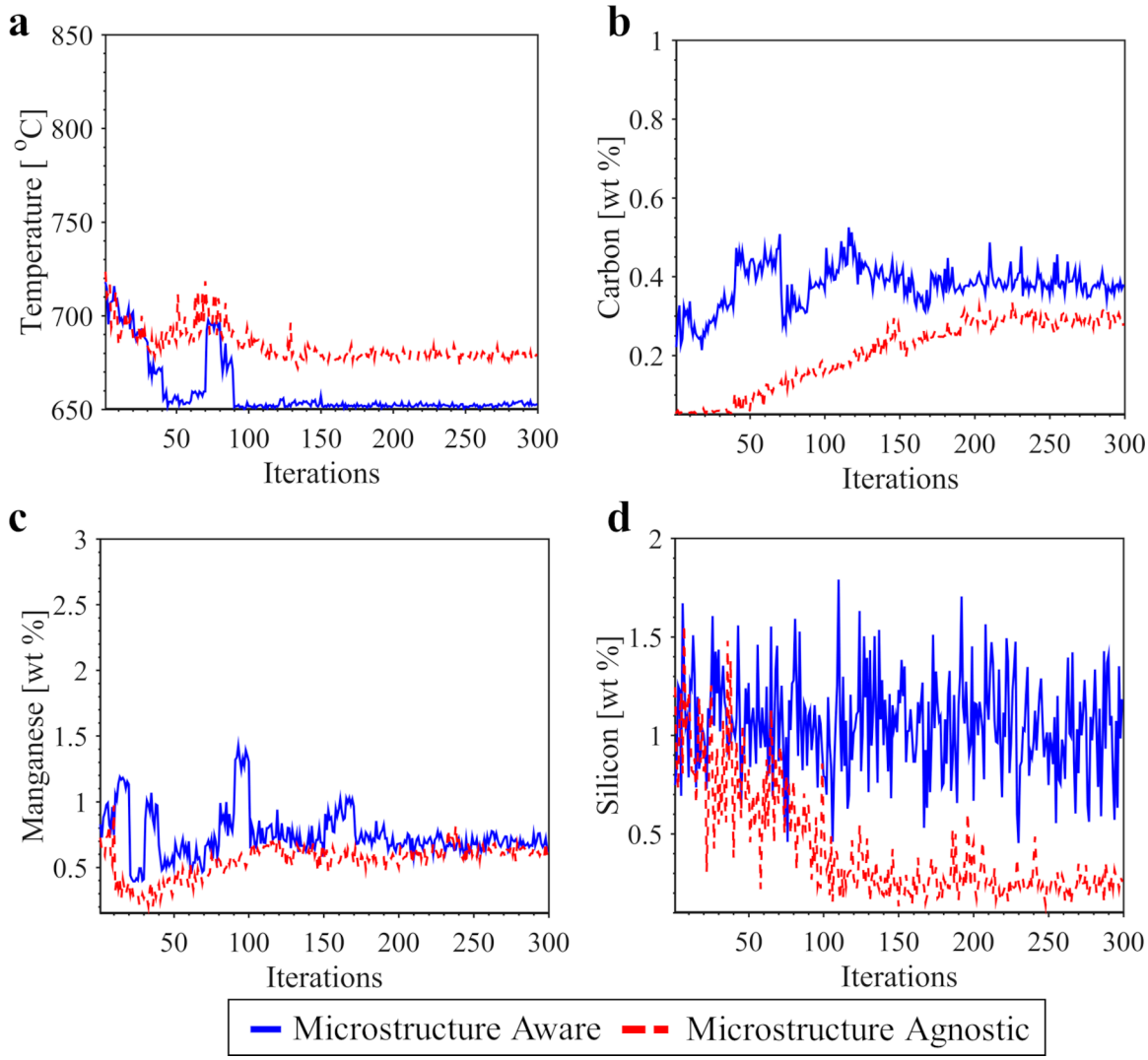

Figure 3.5: A comparison of the optimum processing/chemistry parameters identified by the traditional *microstructure agnostic* and the novel *microstructure aware* material design approaches. (a)-(d) Comparing the average optimal values of the processing parameter, intercritical annealing temperature, and the amount of alloying elements, Carbon, Manganese and Silicon that correspond to the average maximum objective value at each design iteration over five realizations of the design process.

erations for one realization of the design process. As shown in Fig. 3.6(a), the *microstructure aware* approach extensively queries the design space using more sophisticated Secant Method and Elastic Constraint models while the *microstructure agnostic* approach favors querying the design space using the simple Isostress model during the early stages of the design process. While at the later stages of the design process, both the approaches begin querying the design space through all

available ‘information sources.’

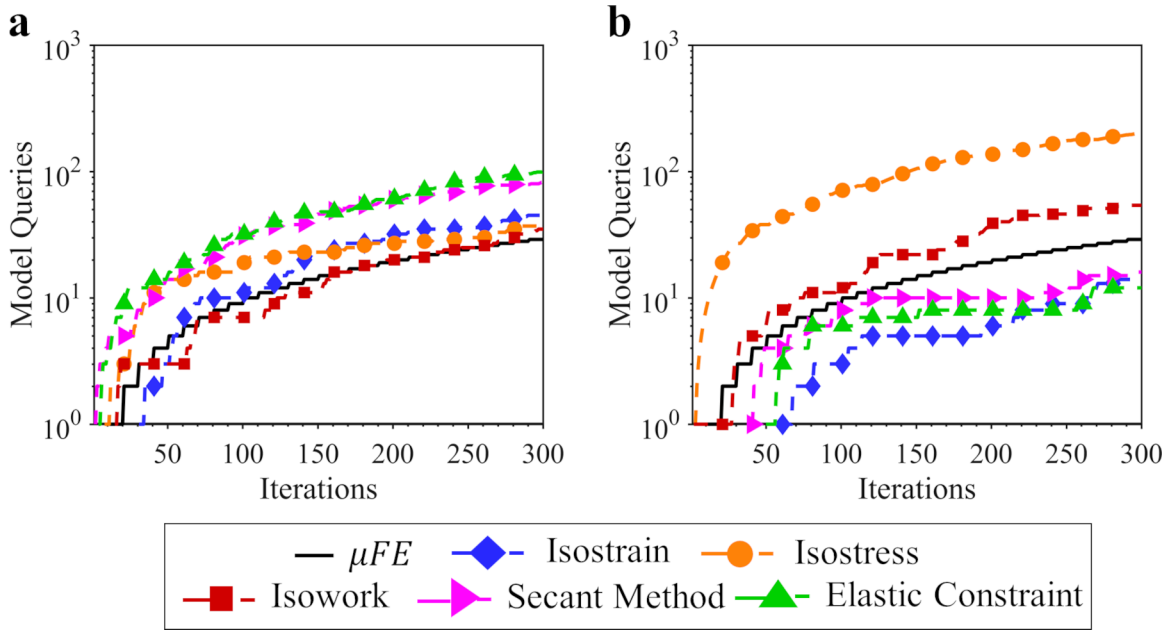

Figure 3.6: Exploitation of ‘information sources’ (Isostrain, Isostress, Isowork, Secant Method and Elastic Constraint reduced-order models) and the ‘ground truth’ (μFE) model at each design iteration by the (a) novel *microstructure aware* and the (b) traditional *microstructure agnostic* material design approaches. The results are shown for one realization of the design process.

The results presented thus far clearly demonstrates that the two design approaches not only take very different route in the design space but also utilize different ‘information sources’ to query the design space in search of the same objective. The results also demonstrate that the *microstructure aware* approach converges rapidly in the microstructure space and provides better design solution compared to the *microstructure agnostic* approach. Now to understand what enables the superior performance of the *microstructure aware* approach compared to the *microstructure agnostic* approach we compare the predictions of the initial (at the very first design iteration) fused Gaussian Process models built using the two approaches with that of the predictions of exhaustively querying the chain of computational thermodynamics and the ‘ground truth’ model in Fig. 3.7, for one realization of the design process. As shown in Figs. 3.7(a) and (b), despite the fact that the same

five sets of $\mathbf{X_I}$-$\mathbf{X_O}$ correlations are used to built the initial fused Gaussian Process models for both the approaches, the predictions of the initial fused Gaussian process model for the *microstructure aware* approach correlates extremely well with the 'ground truth' compared to the predictions of the initial fused Gaussian process model for the *microstructure agnostic* approach. The parity plots in Figs. 3.7(c) and (d) also highlight the quantitatively better correlation between the predictions of the initial fused Gaussian process model for the *microstructure aware* approach and the 'ground truth' compared to that of the *microstructure agnostic* approach. In conclusion, an explicit incorporation of the knowledge of the material microstructure in the design framework significantly enhances the initial knowledge of the microstructure - property correlations that in turn leads to more efficient and effective design process.

3.4 Discussion

Although as material scientists and engineers we aspire to unravel the underlying PSP relationship of materials, in practice the material microstructure information is not used as a direct input in a material design process, and only an analysis of the same is carried out *a posteriori* to rationalize the attained properties. This raises a fundamental question, can the intermediate microstructure information aid in the material design process. To answer this question, herein, a rigorous analysis has been carried out to probe the importance of the microstructure information in the material design process that involves finding the right combinations of material chemistry and processing condition that maximizes a targeted mechanical property of a model dual-phase steel using a closed-loop multi-fidelity BO framework. This material design problem is first solved by following the traditional *microstructure agnostic* approach where the material design space includes the material chemistry and processing condition, and the microstructure information is only used to carry out multiscale simulations to establish PSP relationships. Next, the same material design problem is solved by following a novel *microstructure aware* approach where the material design space not only includes the material chemistry and processing condition but also the microstructure information.

The results clearly show that an explicit incorporation of the knowledge of material microstruc-

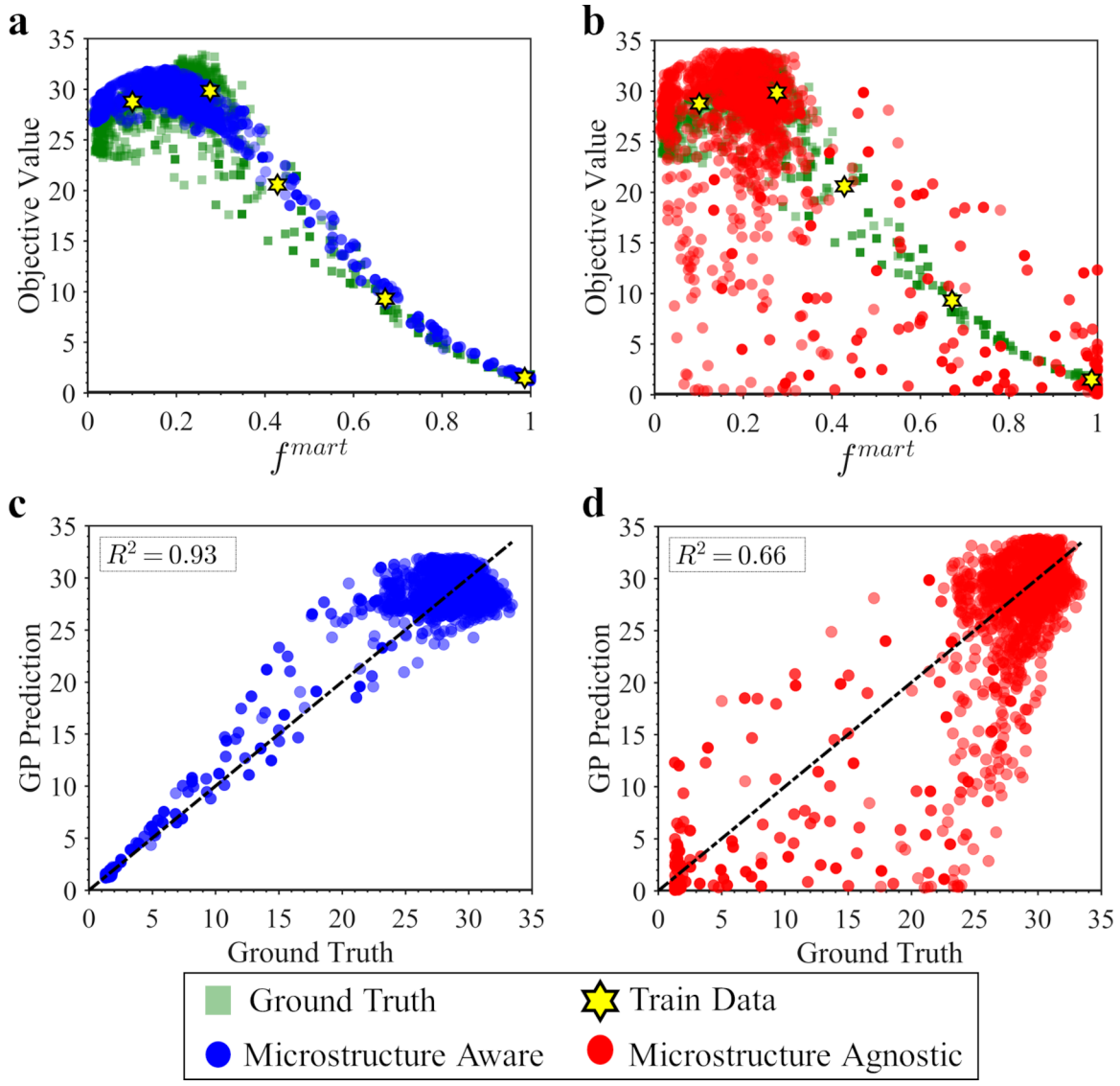

Figure 3.7: A comparison of the predicted variation of the objective value as a function of the material microstructure characterized by the volume fraction of the martensite phase, f^{mart}, obtained by exhaustively querying the chain of computational thermodynamics and 'ground truth' (μFE) model and by querying the initial (at the very first design iteration) fused Gaussian Process model for the (a) *microstructure aware* and (b) *microstructure agnostic* approaches. Parity plots of the objective value obtained by exhaustively querying the chain of computational thermodynamics and 'ground truth' and by querying the fused Gaussian Process model for the (c) *microstructure aware* and (d) *microstructure agnostic* approaches. The results are shown for one realization of the design process and the five initially known 'ground truth' information are marked with stars in (a) and (b).

ture in the decision-making process as one navigates the material design space not only accelerates the material design process but also results in comparatively better design solutions. A detailed

analyses of the material design process following the *microstructure agnostic* and *microstructure aware* approaches show that the two design approaches not only take very different route in the design space but also utilize different set of 'information sources' to query the design space in search of the same objective. The superior performance of the *microstructure aware* design approach compared to the *microstructure agnostic* design approach is rooted in the fact that an explicit incorporation of the knowledge of the material microstructure in the design framework significantly enhances our initial knowledge of the microstructure - property correlation that in turn leads to more efficient and effective design process.

Since it is the difference in the initial knowledge of the microstructure - property correlation that leads to the superior performance of the *microstructure aware* design approach compared to the *microstructure agnostic* design approach, it is warranted to compare their performance for a range of known initial design space (input) - objective (output) correlations used to initiate the design process. To this end, the performance of the two design approaches by setting up the design framework using only one, ten or twenty five randomly selected sets of initially known input - output correlations is compared. Also, to avoid any bias in the design process due to the initial sets of randomly selected input - output correlations, five realizations of the design process for each sets of initially known input - output correlations are carried out. The results of this exercise are given in the Appendix A, Figs. A1-A15. The results clearly show that irrespective of the number of initially known input - output correlations used to initiate the design process, the performance of the *microstructure aware* design approach is always better than the *microstructure agnostic* design approach. Furthermore, the results also show that the relative performance of the *microstructure aware* design approach is even better than the *microstructure agnostic* design approach when fewer number of initially known input - output correlations are used to initiate the design process.

Note that incorporating the microstructure information in the material design space increases the dimensionality of the problem, however, the results show a positive impact on the decision-making process with increasing the dimensionality of the design space. The positive impact of increasing the dimensionality of a given problem has been explored and exploited in a variety of

scientific and engineering problems. For example, the so-called 'kernel trick' of machine learning [66], which replaces inner products with kernel functions to enable nonlinear learning, effectively raises the dimensionality of a machine learner from low dimension to high and even infinite dimensions [67]. This is especially very common when using support vector machines for classification. In model order reduction, recent methods for lifting maps [68, 69] introduce auxiliary variables to a system model to provide more mathematical structure. For example, the introduction of auxiliary variables through lifting maps can lead to polynomial systems of differential-algebraic equations or in other cases, system dynamics with quadratic structure. The resulting well-behaved mathematical structure of the problem caused by the increase in dimensionality leads to far more efficient solution strategies enabling larger problems to be tackled computationally [70]. The identification of new, relevant dimensions in a given problem can also have a profound impact on an entire fields of study. For example, the celebrated Buckingham π theorem [71] from the study of dimensional analysis [72] states on physical grounds that physics-based equations may be rewritten in terms of dimensionless parameters providing there is some physical connection among the variables in the equation. This identification of a latent governing parameter or set of parameters has had a profound impact on the field of fluid mechanics, where parameters such as the Reynolds number, the Mach number, and the Froude number have been discovered. These parameters are all derived from the original variables of a given problem, and therefore, even though they increase the dimensionality of the problem, it leads to a dramatic increase in the physical understanding of the phenomena at play.

While the proposed *microstructure aware* closed-loop multi-fidelity BO framework for material design is demonstrated here to be extremely efficient and effective in realizing goal-oriented material design using a combination of models and simulation techniques, this design framework can also be put into practice even for an entirely experimental material design campaign by using ever-growing high-throughput material processing and characterization techniques. It is also important to note that since each 'information source' is represented in the design framework as a stochastic model (i.e., Gaussian Process) and thus there is no fundamental limitation on using a

combination of experimental, modeling and/or simulation based 'information sources.' The proposed material design framework can also be further enhanced by utilizing more sophisticated thermodynamics/kinetics-based modeling schemes (e.g., phase-field simulations [**?**]) to not only predict the phase volume fraction and composition but also size and morphology of the constituent phases, and by incorporating them explicitly in the decision-making process. Another future direction to enhance the performance of the proposed material design framework will be to incorporate adaptive active subspace method to efficiently handle the large dimensionality of the design space [73, 74] by taking advantage of the fact that in materials design problems the objective function in general is more sensitive to some design variables compared to others.

3.5 Summary

In this work, a *microstructure aware* closed-loop multi-information source fusion (multi-fidelity) Bayesian Optimization (BO) framework for goal-oriented materials design has been presented. The specific material design problem considered here involved finding the right combinations of material chemistry and processing condition that maximizes a targeted mechanical property of a model dual-phase steel. This material design problem is first solved by using both the traditional *microstructure agnostic* approach where the microstructure information is only used to establish PSP relationships and the proposed *microstructure aware* approach where the microstructure information is also used in decision-making as we navigate through the material design space. The analysis clearly show that these two design approaches not only take very different route in the design space but also utilize different 'information sources' to query the design space in search of the same objective. Furthermore, it is shown that explicit incorporation of the knowledge of the material microstructure information in the *microstructure aware* approach significantly enhances the initial knowledge of the microstructure - property correlation that in turn leads to more efficient and effective design process compared to the *microstructure agnostic* approach.

Although explicitly incorporating the microstructure information in the material design framework increases the dimensionality of the problem, the results show exceptional positive impact of this increase in dimensionality on the design process. The positive impact of increasing the dimen-

sionality of a given problem has been explored and exploited in a variety of scientific and engineering problems. These additional parameters (for instance, microstructural information in this particular case) are derived from original parameters of the problem, and therefore, even though they increase the dimensionality of the problem, they lead to a dramatic increase in the physical understanding of the phenomena at play.

While the efficiency and effectiveness of the proposed *microstructure aware* closed-loop multi-fidelity BO framework for materials design using a combination of models and simulation techniques is demonstrated, this design framework can also be put into practice even for an entirely experimental material design campaign by using ever-growing high-throughput material processing and characterization techniques. Also, since each 'information source' is represented as a stochastic model in the design framework, there is no fundamental limitation on using a combination of experimental, modeling and/or simulation results as independent 'information sources.'

4. DUCTILE FRACTURE PREDICTION USING EVOLVING GRAPHS

4.1 Introduction

Solving a variety of physical problems involves finding the optimal path. One such example is finding the optimum driving directions using a navigation application. This is essentially an optimization problem of finding the shortest path or weighted (e.g., based on traffic conditions or speed limits) shortest path between a source and a target in a well-defined network of paths or simply a graph constituting nodes and edges. However, for several physical problems, either the graph or the target, or both are unknown a priori. An example of a problem where the source and the target are known, but the graph is not known is, a path search in a complex evolving social networking site such as Facebook, LinkedIn, or Twitter. For example, if a person is trying to connect with a friend, Facebook tries to find the shortest path to reach that friend in a network where the connections between the source person and target person are not unknown a priori. Similarly, a scenario of a problem involving optimal path search where the source and the graph are known, but the target is not known, is intergranular crack growth in a material microstructure with known distribution consisting of grain boundary connections. In such problems, the source, i.e., the initial location of the crack and graph i.e., the microstructural network is known, but the target i.e., the end of the crack is not known a priori. An example of a more complex physical problem that involves path search where only the knowledge of source is known but both the target and graph are not known is, optimal path-planning of mobile robots in rescue missions which entails searching a path from the source to a hidden target in an unknown network.

For simple problems where the knowledge of the source, target, and the graph are all known a priori, the optimal path between the source and target can be easily found using classical pathfinding algorithms such as Dijkstra's algorithm [75], shortest path algorithm [76], and breadth-first search algorithm [77]. For example, the problem of search for a stable chemical reaction pathway starting from a precursor to a target to accelerate the synthesis of solid-state materials [78].

Here, the search for the stable reaction path i.e., the lowest-cost path in the known network of all possible reactions is enabled by using breadth-first search algorithm [77]. However, these classical pathfinding algorithms are insufficient to solve pathfinding problems in which the source and target are known, but the graph is not known. As outlined above in the preceding paragraph, the problem of optimal path search in a social networking site where the connections between all nodes in the graph are not known a priori is not possible using the classical pathfinding algorithms as they require the knowledge of graphs in which the search for an optimal path is carried out. Kleinberg et al. proposed methodologies to solve such problems by finding the optimal path from a source to a target through establishing local connections, starting from the source node and then progressing through all the nodes until the complete network is established [79, 80]. Similarly, Kim et al. and Jeong et al. proposed pathfinding strategies to search for an optimal path where the global information of the networks is not accessible, and only the local information on the connectivity is known [81, 82].

The algorithms [79, 80, 81, 82] described in the preceding paragraph merely provide a guideline to establish a network, i.e., all possible connections between a source and a target but fail when the target is unknown. For example, the problem of crack growth in a microstructure that can be represented as a graph involves finding an optimal crack path from a source to an unknown target with the knowledge of the graph. In a previous work [83], authors focused on a scenario involving ductile intergranular crack growth where the problem of the shortest path prediction was to predict the path of a growing crack in a microstructure of grain boundary network with each grain boundary junction represented as nodes of a graph and each grain boundary represented as edges of a graph. The weight of each grain boundary segment corresponded to that of energy required for the crack to propagate through the respective grain boundary and the authors hypothesized that for a given grain boundary segment with a known position, orientation, and length, the crack growth resistance could be calculated using a series of unit event microstructure-based finite element calculations. Here, the search for the optimal path i.e., the crack path of least crack growth resistance was then found using the collection of each local least energy possible path ob-

tained at each grain boundary junction from the initial crack tip until the end of the microstructure. Similarly, in Ref. [84] the authors developed an approach based on graph theory to model brittle fracture and predict the crack path in a polycrystalline material. Here, the approach involves first representing the finite element mesh of a material microstructure as a graph. The crack path is then predicted based on an energy minimization principle with the cracks total energy as the cost. Similarly, several other physical problems entail an optimal search of an unknown target in a vastly complex network, such as searching for an unknown target in a DNA network by proteins promoters [85]. In Ref. [85], a random walk search strategy based on an algorithm of search of a hidden target on dendritic tree-type networks developed in Ref. [86] is employed to find an optimal path for DNA-binding proteins to specific DNA sites.

This work focuses on one of the most complex physical problem of path search i.e., optimal path search from a source to an unknown target without a priori knowledge of the graph. More specifically, the problem of path selection to predict the crack growth in heterogeneous materials where in general, only the source i.e., the initial position of the crack is known but the target i.e., end of the crack and the graph i.e., connections between microstructural features is not known. A novel model based on evolving graphs is proposed to predict the crack path and its crack growth resistance in a material microstructure. To illustrate the approach, two physical problems are considered: (i) growth of a ductile crack in two-phase microstructure with a matrix phase having second phase particles or inclusions distributed in it (a disconnected type of microstructure). (ii) Growth of an intergranular ductile crack in a two-phase microstructure consisting of grains and grain boundaries (a connected type of microstructure). The efficacy of the proposed approach is demonstrated by comparing its predictions with full-field microstructure-based finite element calculations.

4.2 Methods

4.2.1 Microstructure-based finite element boundary value problem formulation

The growth of a ductile crack in both Disconnected and Connected types of microstructural networks is first modeled through the finite element analysis of transient three-dimensional boundary value problem. The finite element formulation is based on the dynamic principle of virtual work written as

$$\int_V \boldsymbol{\tau} : \delta\mathbf{D}\, dV = \int_S \mathbf{T}\cdot\mathbf{u}\, dS - \int_V \rho\frac{\partial^2\mathbf{u}}{\partial t^2}\, dV \tag{4.1}$$

where $\mathbf{u}$ is the displacement vector, t is time, V is the volume of the region analyzed in the reference configuration, S is its surface in the reference configuration, ρ is the density in the reference configuration, $\boldsymbol{\tau}$ is the Kirchhoff stress tensor, and $\mathbf{T} = \boldsymbol{\tau}\cdot\mathbf{n}$ with $\mathbf{n}$ being normal to S.

Similar to works in Refs. [83, 87, 88, 89], a mode I small-scale yielding boundary value problem is analyzed for a slice of a material with an initial crack as shown in Figure 4.1. Initial and boundary displacements and velocities corresponding to the isotropic linear elastic mode I plane strain singular field are applied in such a way to minimize dynamic effects. Remote displacement boundary conditions corresponding to the quasi-static linear isotropic elastic mode I crack tip stress intensity factor K_I are prescribed. The stress intensity factor K_I is considered to increase monotonically with time and the values of $\dot{K}_I$ used are 4×10^6 MPa $\sqrt{\text{m}}\text{s}^{-1}$ and 1.2×10^7 MPa $\sqrt{\text{m}}\text{s}^{-1}$ for disconnected and connected microstructural networks. The constitutive framework used is a rate-dependent modified Gurson constitutive relation [90] for a progressively cavitating solid with the flow potential given by

$$\Phi = \frac{\sigma_e^2}{\bar{\sigma}^2} + 2q_1 f^* \cosh\left(\frac{3q_2\sigma_h}{2\bar{\sigma}}\right) - 1 - \left(q_1 f^*\right)^2 = 0 \tag{4.2}$$

where, σ_e is the Mises effective stress, σ_h is the hydrostatic stress, $\bar{\sigma}$ is the material flow strength and $q_1 = 1.25$, $q_2 = 1.0$ are the parameters introduced in Refs. [91, 92]. In Equation 4.2, f^* is the effective void volume fraction given by

$$f^* = \begin{cases} f, & f < f_c \\ f_c + (1/q_1 - f_c)(f - f_c)/(f_f - f_c), & f \geq f_c \end{cases} \tag{4.3}$$

where, f is the void volume fraction, f_c is the critical void volume fraction to void coalescence and f_f is the void volume fraction at failure. The value of f_c and f_f for disconnected microstructure modeling are taken as 0.1 and 0.2 respectively as in Ref. [88] and value of f_c and f_f for connected microstructure modeling are taken as 0.12 and 0.25, respectively.

The rate of deformation tensor is given by

$$\mathbf{d} = L^{-1} : \hat{\boldsymbol{\sigma}} + \mathbf{d}^p \tag{4.4}$$

where, L is the isotropic elastic moduli tensor, $\hat{\sigma}$ is the Jaumann rate of Cauchy stress tensor and $\mathbf{d}^p$ is the viscoplastic part of the deformation tensor and is given by

$$\mathbf{d}^p = \left[\frac{(1-f)\bar{\sigma}\dot{\bar{\epsilon}}}{\boldsymbol{\sigma} : \frac{\partial \Phi}{\partial \boldsymbol{\sigma}}} \right] \frac{\partial \Phi}{\partial \boldsymbol{\sigma}} \tag{4.5}$$

here, $\dot{\bar{\epsilon}}$ is the plastic strain rate of the matrix and is given by

$$\dot{\bar{\epsilon}} = \dot{\epsilon}_0 \left[\frac{\bar{\sigma}}{g(\bar{\epsilon})} \right]^{1/m} \quad g(\bar{\epsilon}) = \sigma_0 \left[1 + \bar{\epsilon}/\epsilon_0 \right]^N \tag{4.6}$$

where, $\bar{\epsilon} = \int \dot{\bar{\epsilon}} dt$, $\dot{\epsilon_0} = 10^3 s^{-1}$ is the reference strain rate, $m = 0.01$ is the strain rate sensitivity exponent, σ_0 is the reference flow strength, $\epsilon_0 = \sigma_0 / E$ is the reference strain and $N = 0.1$ is the strain hardening exponent.

The evolution of void volume fraction, $\dot{f}$, accounting for both void growth and void nucleation is given by

$$\dot{f} = (1-f)\mathbf{d}^p : \mathbf{I} + \dot{f}_{nucl} \tag{4.7}$$

4.2.2 Disconnected Microstructural Network modeling

For the disconnected type of microstructural network (i.e. a two phase microstructure with a matrix phase having second phase particles or inclusions distributed in it), the elastic and plastic properties of the matrix phase and the inclusions are taken to be same, with values of Youngs Modulus, $E = 70$ GPa, Poissons ratio, $\nu = 0.3$ and initial flow strength, $\sigma_0 = 300$ MPa. Next, the material microstructure is characterized by two populations of void nucleating particles: (i) uniformly distributed small particles that are modeled as plastic strain controlled void nucleation sites; and (ii) large particles or inclusions that are modeled as stress controlled void nucleation sites. The plastic strain and stress controlled nucleation are given as

$$\dot{f}_{nucl}^{\text{strain}} = \frac{f_N^{\text{strain}}}{s_N^{\text{strain}}\sqrt{2\pi}} \exp\left[-\frac{1}{2}\left(\frac{\bar{\epsilon}-\epsilon_N}{s_N^{\text{strain}}}\right)^2\right]\dot{\bar{\epsilon}} \tag{4.8}$$

$$\dot{f}_{nucl}^{\text{stress}} = \frac{f_N^{\text{stress}}}{s_N^{\text{stress}}\sqrt{2\pi}} \exp\left[-\frac{1}{2}\left(\frac{\bar{\sigma}+\sigma_h-\sigma_N}{s_N^{\text{stress}}}\right)^2\right](\dot{\bar{\sigma}} + \dot{\sigma}_h) \tag{4.9}$$

Here, $f_N^{strain} = 0.04$, $s_N^{strain} = 0.1$, $\epsilon_N = 0.3$, $f_N^{stress} = 0.04$, $s_N^{stress} = 0.2\sigma_0$, $\sigma_N = 1.5\sigma_0$ are the constitutive parameters used for both the strain and stress based nucleation criteria in Equations 4.8 and 4.9 respectively.

Based on the deformation and hydrostatic stress history of the inclusions or large particles, voids nucleate when value of $\bar{\sigma} + \sigma_h$ is greater than a critical value. Similarly a critical strain value controls the nucleation of voids at the homogeneously distributed small particles.

The finite element mesh used here consists a single element through the thickness. A uniform in-plane $(x_1 - x_2)$ plane mesh with in-plane element dimension $100\mu m \times 100\mu m$ is used in a region, $A_{incl} = 0.02m \times 0.006m$ immediately in front of the initial crack tip. The finite element mesh consists of a total number of 68928 twenty-node brick elements. To create these disconnected microstructural network, predetermined number of inclusion, N_{incl} with centers (x_1, x_2) are first randomly generated in this uniform mesh region, A_{incl} such that the center to center distance of two neighboring inclusions is at least twice the radius, r_0 of inclusions, with $r_0 = 150\mu m$. Finally,

the mean inclusion spacing, l_{incl} is estimated as $l_{incl} = \sqrt{A/N_{incl}}$.

4.2.3 Connected Microstructural Network modeling

For the connected type of microstructural network, (i.e. a two phase microstructure consisting of hard grains and soft grain boundaries), the elastic constants of the grains and the grain boundaries are taken to be same, with $E = 116$ GPa, $\nu = 0.3$ and initial flow strength of grains is taken as, $\sigma_0 = 1200$ MPa and the flow strength of softer grain boundary layers is taken as $\sigma_0^l = 800$ MPa. Next, the soft grain boundaries are modeled as both plastic strain and stress controlled nucleation sites, following Equations 4.8 and 4.9. The hard grains are modeled as plastic-strain controlled nucleation sites using Equation 4.8. Here the values of constitutive parameters used for both the strain and stress based nucleation criteria in Equations 4.8 and 4.9 are, $f_N^{strain} = 0.04$, $s_N^{strain} = 0.2$, $\epsilon_N = 0.2$, $f_N^{stress} = 0.06$, $s_N^{stress} = 0.3\sigma_0^l$, $\sigma_N = 1.5\sigma_0^l$.

Similar to finite element mesh of disconnected microstructural network model, the finite element mesh of the entire connected microstructural networks model consists a single element through the thickness. Next, the connected microstructural network is modeled in a region, $A_{GB} = 0.01m \times 0.006m$ ahead of the initial crack tip with uniform in-plane $(x_1 - x_2)$ plane mesh having element dimension $10\mu m \times 10\mu m$. Total number of elements used in the finite element mesh here consists 760,000 twenty-node node brick elements. To create a connected microstructural network with a uniform grain size distribution, the microstructure is generated using Dirichlet tessellation N_g random points chosen in the fine mesh region, A_{GB} in front of the initial crack tip. Next, this fine mesh region, A_{GB} is partitioned with the N_g random points to form N_g Voronoi cells with one generator inside each cell. Each Voronoi cell corresponds to a grain. The grain boundary layers are generated along each grain with a thickness of $20\mu m$. The finite element Gauss integration points in the fine mesh region are assigned to the material properties associated with a grain or a grain boundary layer depending on where they are located, Voronoi cell or grain boundary layer. This method generates N_g grains having an average grain size, $l_{GB} = \sqrt{A/N_g}$.

4.3 Results

Here, a methodology is proposed to find an optimal path in physical problems where both the knowledge of the graph and the target are unknown a priori. More specifically, the problem of finding the path of a growing crack in a material microstructure with an initial notch (Figure 4.1) is considered. Here, the knowledge of the target i.e., end of the growing crack is not known a priori. Furthermore, there are several material microstructures which cannot be represented as graphs as the connections between the microstructural features is not known a priori. For example, a disconnected microstructural network i.e., a material microstructure with a discrete distribution of second phase particles or inclusions in matrix of material. It is well established that ductile fracture in such microstructures occurs by nucleation of voids at these second phase particles followed by growth and coalescence of voids ultimately leading to fracture. However, there is no way of knowing how these inclusions are connected for the crack to grow a priori. Here, it is hypothesized that the growth of the crack occurs locally from its initial location i.e., initial notch and then progress in a similar fashion until it reaches the end of the material microstructure. To demonstrate the proposed approach (Figure 4.1) for finding the path of a growing crack in a material microstructure with an initial notch which involves optimal path search where only the source is known and both target and graph are unknown, two types of microstructural network are considered in which the path of the crack growth is predicted. Disconnected microstructural network, which consists of distribution of discrete inclusions or second-phase particles. These inclusions act as nodes in a graph through which the crack propagates and the connections i.e., the edges between these nodes in not known a priori. The second type of network is a disconnected microstructural network and contains fully resolved grains and grain boundaries within which the crack propagates. Here, the grain boundary junctions act as nodes and grain boundary as edges connecting these nodes. The crack path prediction in both microstructural network involves search for an optimal path starting from the source, the initial crack tip as depicted in Figure 4.1.

The first step in the proposed approach involves building connections between the source i.e., the initial crack tip and the inclusions ahead of the initial crack tip. In a given disconnected mi-

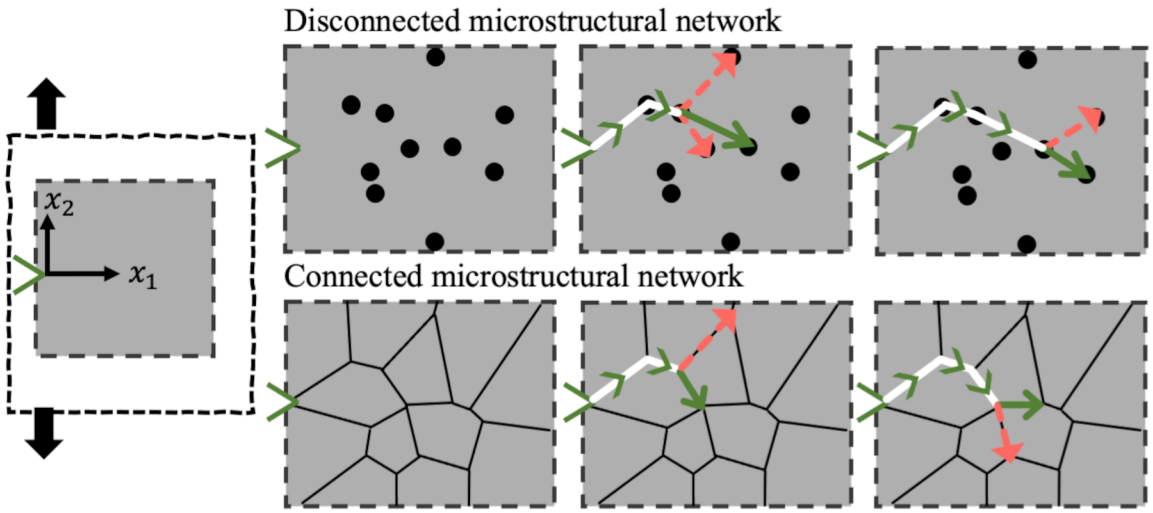

Figure 4.1: Schematic representation of the evolving graph framework to predict crack path in material under mode-I loading with two model microstructures, Disconnected and connected type of microstructural network. For a disconnected microstructural network with a random inclusion distribution, the procedure of finding a path of least crack growth resistance involves, (i) building a local graph at an inclusion or node and (ii) selection of a path or edge using the graph model (shown as solid green line) among the possible paths or edges (shown as red dashed lines) and then (iii) the progression of crack (shown as solid white lines) occurs through accumulation of the predictions from these individual events of local graphs. For a connected type of microstructure, for the prediction of crack path, a local graph is built from the existing network of grain boundaries at each grain boundary junction and then a path or grain boundary is selected (shown as solid green line) among the possible grain boundaries or edges (shown in red dashed line). The propagation of crack occurs through prediction of paths in these individual local graphs built at the grain boundary junctions.

crostructural network consisting of N_{incl} inclusions with their center located at points P_i (where $i = 1, \ldots, N_{incl}$), at a time step t, a local directed graph is built starting from the current crack tip location, $P_c^t \in P_i$ (Note: at time $t = 0$, the crack tip location is simply the initial crack tip). To this end, a search is carried out for all inclusions with center located at points, P_j, that meet the following condition,

$$l_j\left(P_j, P_c^t\right) < 2l_{incl} \quad and \quad x_1\left(P_j\right) > x_1\left(P_c^t\right) \tag{4.10}$$

where, $l_j\left(P_j, P_c^t\right)$ is the distance between the inclusion center, P_j, and the current crack tip location, P_c^t, and l_{incl} is the mean inclusion spacing. Next, edge vectors, $\vec{E_j}$ are defined as line

vectors connecting P_c^t to all P_j.

Similarly, for any given connected microstructural network, at given time step t, a local directed graph is built starting from the current crack tip location, P_c^t (which is always assumed to start at a grain boundary triple junction. Recall, that fracture process in connected microstructural network is that of intergranular fracture.). At a given current crack tip location, P_c^t, the grain boundary segments branching out to the very next grain boundary triple junctions P_j are defined as edge vectors, $\vec{E}_j$.

Finally, in both the microstructural networks, in the time step $t+1$, the path chosen for the crack to grow is along one of the edge, $\vec{E}_c^{t+1} \in \vec{E}_j$, determined as follows,

$$\vec{E}_c^{t+1} = \arg\min_j g\left(\vec{E}_j\right) \quad ; \quad g\left(\vec{E}_j\right) = \Delta J\left(l_j, \theta_j\right) \tag{4.11}$$

where, $l_j = |\vec{E}_j|$ and $\theta_j = \cos^{-1}\left(\vec{E}_j \cdot x_1 / \left(|\vec{E}_j||x_1|\right)\right)$ and $g\left(\vec{E}_j\right) = \Delta J\left(l_j, \theta_j\right)$ is the energetic cost (or the crack growth resistance) required to propagate the crack along the edge vector $\vec{E}_j$ or between the two nodes, P_c^t and P_j. Note, x_1 is the direction of the projected crack growth.

To estimate the energetic cost, $g\left(\vec{E}_j\right) = \Delta J\left(l_j, \theta_j\right)$ required to propagate the crack along the edge vector $\vec{E}_j$ or between the two nodes, P_c^t and P_j, crack growth is modeled as a series of microstructural unit events of disconnected and connected microstructural networks. As illustrated in Figure 4.2, disconnected microstructural networks are generated by varying the inclusion spacing, l_{incl} and the angle θ with respect to the crack tip. Similarly, connected microstructural network series of unit events are generated for various angles, θ and grain boundary segment length, l_{GB}. To this end, small scale yielding finite element calculations are carried out for these series of disconnected and connected microstructural network unit events. Remote displacement boundary conditions corresponding to the quasi-static linear isotropic elastic mode I crack tip stress intensity factor K_I are prescribed. In the disconnected microstructural network unit evets, the growth of the crack is along inclusions 0, 1 and 2. To calculate the crack growth resistance (J-R) curves, i.e. plot of J versus Δa, the value of J is calculated from the applied stress intensity factor K_I using the

relation given by [93],

$$J = K_I^2 \left(\frac{1 - \nu^2}{E} \right) \tag{4.12}$$

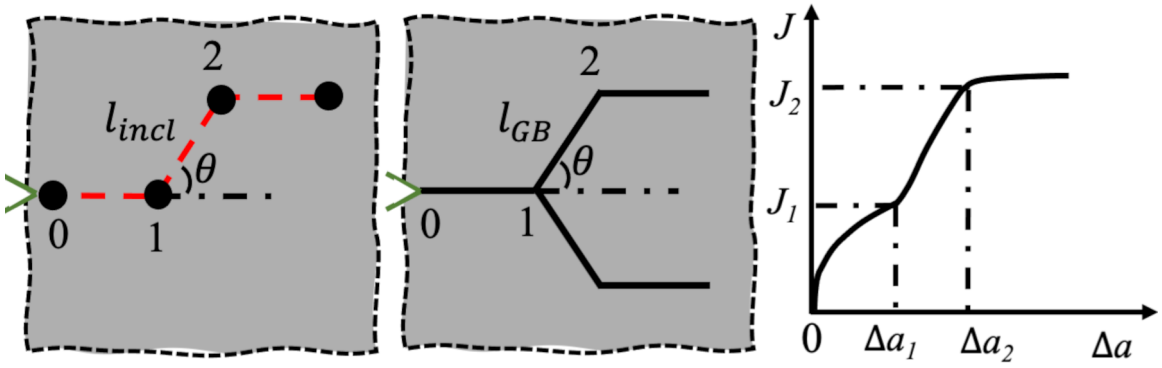

Figure 4.2: Schematic representation of microstructural unit events to calculate energetic cost required to propagate the crack along the edge. Microstructural unit event models for Disconnected (left) and Connected Microstructural network (center) and a representation of crack growth resistance (right) for these unit event microstructures are shown. Unit event results for the disconnected microstructural network are generated by varying the inclusion spacing, l_{incl} and the angle θ with respect to the crack tip. For connected microstructural network, series of unit events are generated for various angles, θ and grain boundary segment lengths, l_{GB}. Estimation of crack growth resistance, ΔJ required by the crack to propagate from inclusion 1 at Δa_1 to inclusion 2 at Δa_2 is computed as $J_2 - J_1$. The ΔJ required by the crack to propagate from grain boundary junction 1 at Δa_1 to end of the grain boundary segment, 2 at Δa_2 is computed as $l_{GB} \cos\theta \left(\frac{dJ}{d(\Delta a)} \right)_{[1,2]}$

Using, Equation 4.12, the crack growth resistance $(J - R)$ curves for the growth of crack along inclusions 0, 1 and 2 is estimated and showed schematically in Figure 4.2(right). Similarly, in connected microstructural network unit events, the growth of crack is along a grain boundary connected to the current crack tip, marked as 0-1, following the grain boundary placed symmetrically at angle , marked as 1-2 in the Figure 4.2 (center). Next, estimation of energetic cost of propagating crack between inclusion 1 at Δa_1 and inclusion 2 at Δa_2, $\Delta J(l_{incl}, \theta)$ is computed as $J_2 - J_1$. Similarly, the energetic cost required to propagate the crack between the grain boundary junction 1 at Δa_1 to end of the grain boundary segment, 2 at Δa_2, $\Delta J(l_{GB}, \theta)$ is computed as

$l_{GB} \cos\theta \left(\frac{dJ}{d(\Delta a)}\right)_{[1,2]}$.

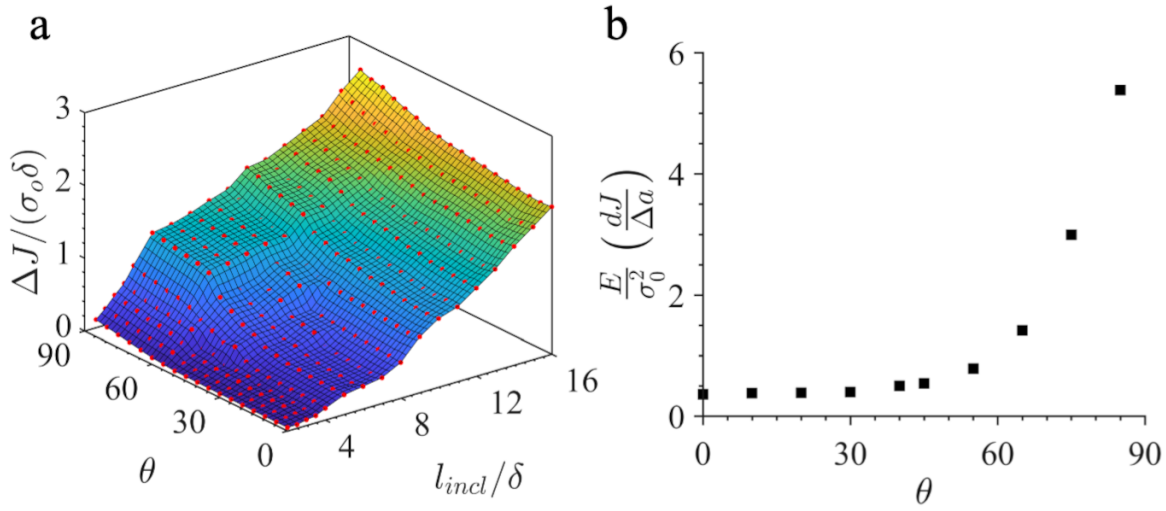

Figure 4.3: Energetic cost to propagate the crack between two nodes of a edge vector. (a)Normalized energetic cost, $\Delta J/\left(\sigma_0 \delta\right)$ to propagate crack between two inclusions along edge vector $\vec{E}_j$ with $|\vec{E}_j| = l_j$ and angle θ with respect respect to the plane of crack propagation. (b) Normalized energetic cost, $\frac{E}{\sigma_0^2}\left(\frac{dJ}{d(\Delta a)}\right)$ to propagate crack along a grain boundary oriented at angle θ with respect to the plane of crack propagation.

Next, using the energetic cost information of propagating crack between two nodes from microstructural unit events of both disconnected and connected microstructural networks, as shown in Figure 4.3, the optimization problem as posed in Equation 4.11 is solved.

The final path traversed by the growing crack at any time $t > 0$ is the combination of all edges, $\vec{E}_c$ as shown schematically in Figure 4.1 and is given by,

$$\Delta a^t = \sum_t \vec{E}_c^t \cdot x_1 \tag{4.13}$$

Finally, for the crack path Δa^t the crack growth resistance, J is given by,

$$J^t = \sum_t g\left(\vec{E}_c^t\right) \tag{4.14}$$

Results of crack path prediction using evolving graph coupled with microstructural discrete unit and path predicted by full-field microstructure-based finite element calculations for a disconnected microstructural network consisting of a discrete distribution of inclusions with mean inclusion spacing, $l_{incl} = 6\delta$ (The parameter $\delta = 200\mu m$ is used a normalization length in all the results presented further) are shown in Figure 4.4. Specifically, the procedure of path prediction by the proposed approach is shown by highlighting the progression of crack growth at three progressing time steps at crack path locations, $\Delta a/\delta \approx 22.5$, 40 and 60 in the disconnected microstructural network. Here, as the crack starts to grow from an initial notch shown in Figure 4.4(a), using the proposed approach as described earlier, a local graph is constructed at this initial notch and a crack path (or edge) and the next inclusion (or node) is selected from all the possible paths. The possible crack paths (edges) of the local graph are represented by dashed red lines and the selected crack path i.e., the edge with least crack growth resistance, ΔJ among these edges is represented by the solid green line. The decision-making process to choose the path with least crack growth resistance follows the procedure described in the above. Figure 4.4(b) shows the crack path prediction from finite element analysis at the same location, $\Delta a/\delta \approx 22.5$ as in Figure 4.4(a). As the crack propagates through building of local graph and then selection of crack path with minimum ΔJ, Figure 4.4(c), shows the selected crack path among all possible paths in the local graph built at $\Delta a/\delta \approx 40$ and Figure 4.4(d) shows crack path prediction obtained from finite element analysis. Finally, as the crack propagates towards the end of the microstructure, at $\Delta a/\delta \approx 60$, Figure 4.4(e) shows the path with minimum ΔJ selected among all the possible paths in the local graph built at this inclusion. Figure 4.4(f) shows that the path prediction from finite element analysis follows the same path selected using the proposed approach.

Figure 4.5 compares the normalized crack growth resistance $(J - J_0)/(\sigma_0\delta)$, versus normalized crack extension $(\Delta a - \Delta a_0)/\delta$ for the disconnected microstructure in Figure 4.4 with mean inclusion spacing, $l_{incl} = 6\delta$ computed from finite element calculations and crack growth resistance curves obtained from the proposed approach calculated based on the selected path, following Equation 4.14. In Figure 4.5, the focus is on the effect of microstructure on crack growth following

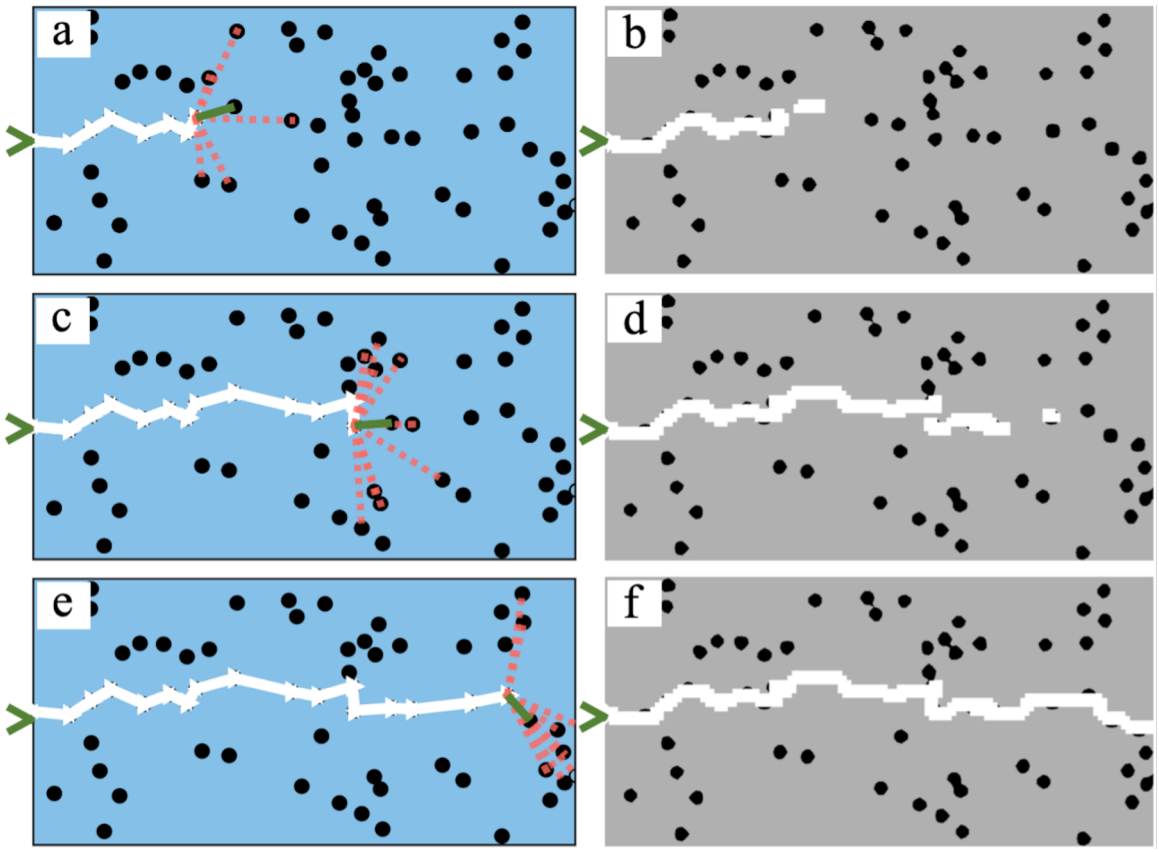

Figure 4.4: Comparisons of crack path predicted using evolving graph method and microstructure-based finite element model for disconnected microstructural network with mean inclusion spacing, , $l_{incl} = 6\delta$ shown at three different time steps. (a) construction of a local graph at a inclusion by building the edges (possible crack paths) that connect to this particular inclusion and then the selection of a crack path with least crack growth resistance, ΔJ. Possible crack paths are highlighted as red dashed lines and the selected crack path is shown in solid green line. The solid white line shows the propagation of crack till this inclusion. (b) shows the path predicted using the finite element calculation till $\Delta a/\delta \approx 22.5$. (c) shows the another instance of construction of a local graph at this inclusion and then selection of the path with minimum ΔJ. (d) shows the path predicted from finite element calculations till $\Delta a/\delta \approx 40$. Similarly (e) and (f) show path predicted from graph model and finite element calculations as the crack reaches $\Delta a/\delta \approx 60$. Here the propagation of crack occurs through collection of predictions of paths from the local graphs built at the inclusions.

crack initiation so that the value of crack growth resistance J_0 corresponding to growth of crack from initial crack tip to the first inclusion chosen in the predicted crack path at location Δa_0 are subtracted from the values of J and Δa respectively. The dotted lines labeled (b) and (d) in Figure 4.5 indicate the location of the microstructures shown in Figure 4.4(b) and Figure 4.4(d). The

crack growth resistance curves from finite element analysis and from evolving graph method are nearly identical to each other except near the end of the microstructure, $(\Delta a - \Delta a_0)/\delta \geq 35$.

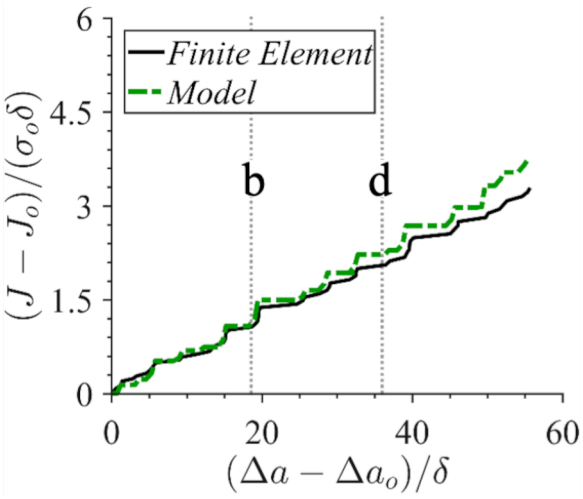

Figure 4.5: Comparisons of crack growth resistance curves predicted using evolving graph method and microstructure-based finite element model for disconnected microstructural network with a discrete distribution of inclusions with mean inclusion spacing, $l_{incl} = 6\delta$. Comparison of curves of normalized J, $(J - J_0)/(\sigma_0 \delta)$, versus normalized crack extension $(\Delta a - \Delta a_0)/\delta$ computed from finite element calculations (solid line) and evolving graph method (dashed green line). The dotted grey lines, marked as b and d correspond to the locations of propagation of crack in Figure 4.4(b) and Figure 4.4(d). From the collection of paths selected at every local graph built, the crack growth resistance for the graph model is computed as the cumulative sum of crack growth resistances for these individual selected paths, as given in Equation 4.14.

Next, the focus is on connected type of microstructures, where a network is already known. In these types of microstructures, the grain boundaries act as the network. However, a priori knowledge of target i.e., the end of the crack is unknown. Results of intergranular crack path predictions from the proposed approach are compared against the finite element calculations for a connected type of microstructure with average grain size, $D_g = 5\delta$ as shown in Figure 4.6. Similar to the results for disconnected microstructural network, the procedure of path prediction using the evolving graph method is presented by highlighting the progression of crack growth at three locations, $\Delta a/\delta \approx 12.5$, 25 and 30. As the crack propagates through the first grain boundary located the

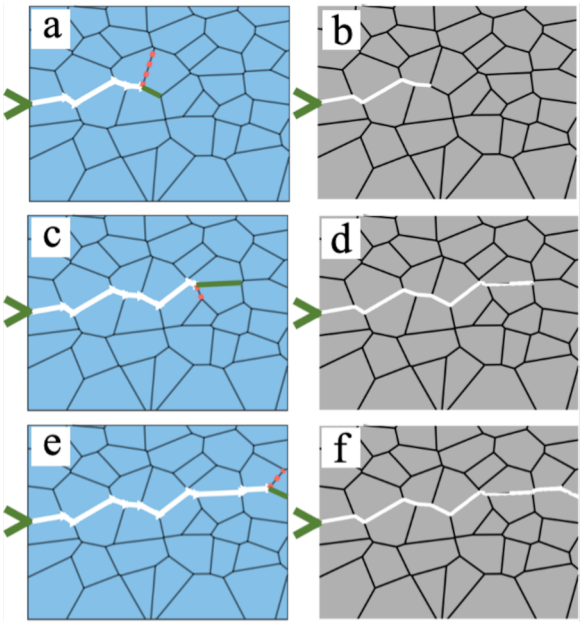

Figure 4.6: Comparisons of crack path predicted using evolving graph method and microstructure-based finite element model for connected microstructural network with average grain size, $d_g = 5\delta$ shown at three different time steps. (a) construction of a local graph at the grain boundary junction from the network of grain boundaries at this particular junction and then the selection of a crack path with least crack growth resistance, ΔJ. The edges or the possible paths are highlighted as red dashed lines and the selected crack path is shown in solid green line. The solid white line shows the propagation of crack till this grain boundary junction where the local graph is built. (b) shows the path predicted using the finite element calculation till $\Delta a/\delta \approx 12.5$. (c) shows the another instance of construction of a local graph at this inclusion and then selection of the path with minimum ΔJ. (d) shows the path predicted from finite element calculations till $\Delta a/\delta \approx 25$. Similarly (e) and (f) show path predicted from graph model and finite element calculations as the crack reaches $\Delta a/\delta \approx 30$. Here the propagation of crack occurs through collection of predictions of paths from the local graphs built at these grain boundary junctions.

initial notch indicated in Figure 4.6, a local graph is built at the first grain boundary triple junction and then a next crack path (grain boundary or edge) to propagate is selected among the two possible crack paths of the local graph built, using the procedure described above. Figure 4.6(a) shows an instance where a local graph is built at a particular grain boundary junction and a crack path selected, shown in solid green line among the other possible edge of the local graph, shown in dashed red line, at $\Delta a/\delta \approx$12.5. The solid white line represents the crack path prediction from the proposed approach till this grain boundary junction where the local graph is built. Figure 4.6(b)

shows the prediction from the finite element calculations at $\Delta a/\delta \approx$12.5 and it is observed that, the path predictions from the proposed approach is identical to that of the finite element calculations. Similarly, as the crack propagates, another instance of the process of the selection of crack path at the local graph built is shown in Figure 4.6(c). Figure 4.6(d) shows the finite element prediction of the crack path at $\Delta a/\delta \approx$25. Finally, the progression of the crack path selection as the crack reaches near the end of the microstructure region at $\Delta a/\delta \approx$30, from the proposed approach is shown in Figure 4.6(e) and from finite element calculations is shown in Figure 4.6(f).

Figure 4.7 compares the normalized crack growth resistance $J, (J - J_0)/(\sigma_0\delta)$, versus normalized crack extension $\Delta a/\delta$ for the connected microstructural network with average grain size, $d_g = 5\delta$ as shown in Figure 4.6, from finite element calculations computed from Equation 4.12 and crack growth resistance curves obtained from graph model calculated based on the selected path, following Equation 4.14. The dotted lines labeled marked as (b) and (d) in the Figure 4.7 indicate the location of the microstructures shown in Figure 4.6(b) and Figure 4.6(d). The crack growth resistance curves from finite element analysis and from graph model are nearly coincide with each other.

4.4 Discussion

Many physical problems involve search for an optimal path from a source to unknown target without the knowledge of the graph i.e., the connections between the physical environment in which the search is carried out. In such scenarios, classical pathfinding algorithms fail to provide a solution and thus new methodologies are required to tackle such physical problems. To solve a problem of optimal path search from a source to an unknown target without the knowledge of the graph, herein, a methodology is proposed involving finding the path of a growing a crack in a material microstructure where the only the knowledge of the source i.e., the start of the crack is known. More specifically, finding the path of a crack in two types of microstructures, a disconnected microstructural network and a connected microstructural network is considered. A disconnected microstructural network constituted of a discrete distribution of inclusions in matrix of material where the connections between the inclusions are not known a priori. The second one, a

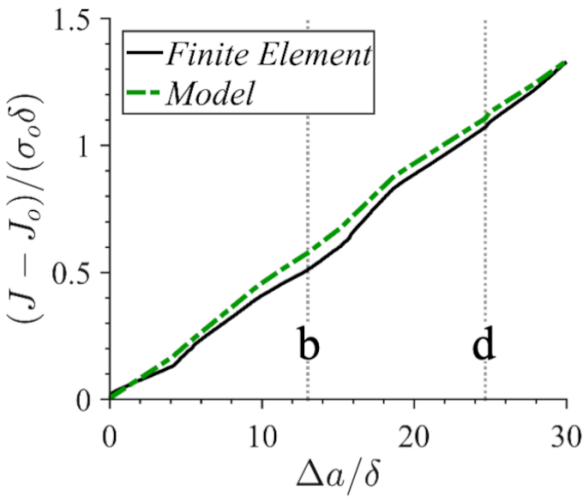

Figure 4.7: Comparisons of crack growth resistance curves predicted using evolving graph method and microstructure-based finite element model for connected microstructural network with average grain size, $d_g = 5\delta$. Comparison of curves of normalized $J, (J - J_0)/(\sigma_0 \delta)$, versus normalized crack extension $\Delta a/\delta$ computed from finite element calculations (solid line) and graph model (dashed green line) for the connected microstructural network in Figure 4.6. The dotted grey lines, b and d correspond to the locations of propagation of crack in Figure 4.6(b) and Figure 4.6(d). From the collection of paths selected at every local graph built, the crack growth resistance for the graph model is computed as the cumulative sum of crack growth resistances for these individual selected paths, as given in Equation 4.14.

connected microstructural network which constituted of fully resolved grains and grain boundaries within which the crack propagates. Herein a novel approach to find the crack path and the energy required to propagate the crack is proposed. It is hypothesized that the growth of a occurs locally i.e., the total crack path is a collection of local crack paths. The search for local crack path is done by building local graphs and the optimal path is then estimated using the knowledge of energetic cost to propagate the crack between two nodes which estimated using microstructural unit event finite element calculations. This process is repeated until the end of the microstructure is reached, and the final crack path is nothing, but the collection of the local crack paths predicted. Next, using the knowledge of the energetic cost of each local crack path, to this end, the total energy required to propagate the crack is estimated as the algebraic sum of energetic cost of each local crack paths. Finally, the crack path and its crack growth resistance in two types of microstructures using microstructure-based finite element calculations is estimated.

The results clearly show that the path predicted by the proposed approach correlates extremely well with that of the predictions from microstructure-based finite element calculations. Not only that, also the energy required to propagate that crack along the predicted crack path i.e., the crack growth resistance curves match extremely well with that of the crack growth resistance curves obtained by microstructure-based finite element calculations. To show the efficacy of the proposed approach, to this end the crack path and its crack growth resistance is predicted for disconnected microstructures with three different distributions of inclusions with mean inclusion spacing, $l_{incl} = 4\delta$, 6δ and 8δ. For each mean inclusion spacing, two realizations of disconnected microstructures with random inclusions distributions were generated. The results of this exercise are given in Appendix B, Figs. B1-B10. Similar exercise is carried out to predict the crack path and its crack growth resistance for connected microstructures with three different grain size distributions with average grain size, $d_g = 2.5\delta$, 5δ and 7.5δ. For each grain size, two realizations of connected microstructure with random grain distributions were generated. The results of these predictions are given in Appendix B, Figs. B11-B20. The results clearly show that the proposed novel approach based on evolving graph and microstructural unit events can predict the crack path and crack growth resistance in different type of microstructures and the predictions correlate extremely well with that of microstructure-based finite element calculations.

4.5 Summary

Finding optimal path under the circumstances where the knowledge of the target and/or well-connected graph/network is unknown a priori has remained a challenge. In this work, an attempt is made to tackle such a challenge in the context of predicting crack path and crack growth resistance of material microstructures in which fracture is dominated either by a distribution of discrete second-phase particles or grain-boundary networks. Specifically, a novel path search method based on evolving graphs and microstructural unit events has been formulated to predict crack path and crack growth resistance of these microstructures. The predictions of the path search method are thoroughly validated against the results of full-field microstructure-based finite element calculations of fracture. This novel path search method is also extremely computationally expensive

and is well suited for any iterative, non-gradient topological optimization scheme to design fracture resistant material microstructures. Furthermore, this inexpensive path search method can also be used to predict the overall crack growth resistance of materials with a known distribution of second-phase particles or grain boundaries.

5. INFLUENCE OF GRAIN SIZE DISTRIBUTION ON DUCTILE INTERGRANULAR CRACK GROWTH RESISTANCE *

5.1 Introduction

Several physical processes can be viewed as a problem of path selection, for example, flow of a river stream [94] or crack growth in a complex heterogeneous material microstructure [21, 95, 96]. Although the problems of path selection for flow of a river stream and of crack growth in a heterogeneous material involve very different length-scales, their solutions share common features. For example, path selection criteria based on fracture mechanics can be used to predict growth of streams in a diffusion field [94], while a directed graph constructed using microstructure specific discrete unit events can be used to predict crack growth in heterogeneous materials [96]. Intuitively, one expects that the path of a physical process involving path selection can be controlled by engineering the discrete unit events.

It has been shown that it is possible to engineer crack paths by controlling the distribution of second phase particles in a ductile matrix to increase the material's crack growth resistance [95]. In [95], the controlled microstructure was characterized by various sinusoidal distributions of particles with fixed mean particle spacing. The results presented in [95] indicate that the crack path can be engineered to increase the crack growth resistance by appropriately adding or removing particles that guide the crack path.

Although near room temperature ductile fracture in polycrystalline metals and alloys is typically transgranular, several materials of technological interest that have a high specific strength (strength to weight ratio), such as, Al-Li alloys [97] and metastable β Ti alloys [98] undergo intergranular ductile fracture near room temperature. Furthermore, several technologically important multiphase materials, such as multiphase advanced high strength steels undergo ductile fracture along the interface between the hard and the soft phase [99, 100].

*Reprinted with permission from "Influence of grain size distribution on ductile intergranular crack growth resistance" by Molkeri, A., Srivastava, A., Osovski, S. and Needleman, A., 2020. Journal of Applied Mechanics, 87(3), p.031008. Copyright 2020 by ASME

Here, the focus is on a scenario involving ductile intergranular (or interfacial) crack growth. In particular, the possibility of engineering the crack path is explored to increase the material's crack growth resistance by controlling the grain size distribution. Experiments have shown that the grain size distribution of a variety of materials can be controlled by advanced processing routes [98, 101, 102, 103, 104, 105]. Experiments have also shown that a controlled grain size distribution, such as a bimodal grain size distribution, can enhance the crack growth resistance of brittle ceramics [106], the fatigue properties of titanium alloys [107] and the corrosion resistance of steels [108].

Following such experimental observations, analyses of ductile intergranular crack growth in material microstructures with unimodal and bimodal grain size distributions are carried out. The bimodal grain size distributions are characterized by varying grain sizes in layers. Ductile intergranular crack growth is analyzed using both microstructure-based finite element crack growth calculations based on a constitutive framework for a progressively cavitating ductile solid with an isotropic and isotropically hardening matrix material as in [21], and a simple model based on discrete unit events and graph search developed in [96]. In [96], the key unit event associated with intergranular crack propagation was found to be the interaction of a grain boundary crack with a grain boundary segment located at an angle with the initial crack plane. Finite element calculations are also carried out for various orientations of a single grain boundary segment with the initial crack plane to characterize the unit events.

The calculations show that increasing the overall grain size in microstructures with unimodal and bimodal grain size distributions can result in an increase in the crack growth resistance. However, decreasing the grain size in one layer and increasing the grain size in another layer, such that the overall grain size is fixed, can give an even greater increase in the crack growth resistance. Furthermore, the predictions of the simple model based on discrete unit events and graph search are found to be in general agreement with the results of full field microstructure-based finite element crack growth calculations. This suggests that the computationally efficient unit event based graph search model can provide a tool for designing material microstructures with improved intergranular crack growth resistance.

5.2 Methods

5.2.1 Microstructure-based finite element boundary value problem formulation

The material model and the numerical implementation are the same as described in Section 4.2.1. The finite element formulation is based on the finite deformation dynamic principle of virtual work. As in Chapter 4, a mode I small scale yielding boundary value problem is analyzed for a slice of material with an initial crack at $x = 0$ and $y = 0$, as shown in Fig. 5.1.

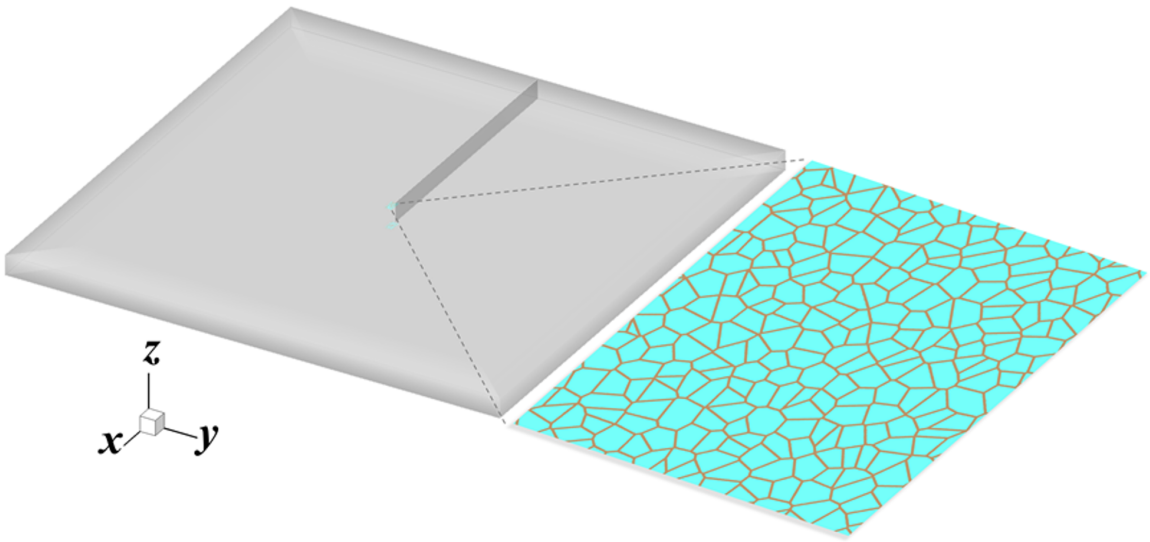

Figure 5.1: Sketch of the initially cracked slice of material analyzed, showing the grain boundary distribution in the region in front of the initial crack tip.

5.2.2 Microstructure generation

For a uniform grain size distribution, the microstructure is generated using Dirichlet tessellation [109] with N_g random points chosen in the fine mesh region in front of the initial crack tip. The fine mesh region of dimensions $A = 1000e \times 600e$ is partitioned with the N_g random points to form N_g Voronoi cells with one generator inside each cell. Each Voronoi cell corresponds to a grain. The

grain boundary layers are generated along each grain with a thickness of $4e$. The finite element Gauss integration points in the fine mesh region are assigned the material properties associated with a grain or a grain boundary layer depending on where they are located, Vornoi cell or grain boundary layer. This method generates N_g grains having an average grain size, $D_g = \sqrt{A/N_g}$.

For microstructures with a bimodal grain size distribution, the fine mesh region is divided into five regions of equal area. In terms of e, the area of each subdivided region is $A_s = 200e \times 600e$. Along the $x-$axis these regions lie in $(K-1)200e \leq x \leq K200e$, where $K = 1, 3, 5$, for regions I and $K = 2, 4$ for regions II. The regions I and II are partitioned with N_g^I and N_g^{II} random points, respectively, and the microstructure is generated following the procedure used to generate uniform grain size distribution. This results in average grain size $D_g = \sqrt{A_s/N_g^I}$ in regions I and $D_g = \sqrt{A_s/N_{II}}$ in regions II. This forms a layered microstructure with regions I having one average grain size and regions II having a different average grain size. Subsequently, these are referred as type I regions and type II regions, respectively.

5.2.3 Unit event modeling

As in Chapter 4, crack growth is modeled as a series of unit events comprising growth of a crack along a grain boundary connected to the current crack tip placed symmetrically at angle θ to the current crack, as illustrated in the inset of Fig.5.2.

Small scale yielding calculations are carried out for various angles θ. There is an initial increase in J without any increase in crack length, as sketched in the inset in going from A to B. The value of ΔJ on the right side axis of Fig.5.2 is defined as $(J_B - J_A)$. Eventually, crack growth occurs along the grain boundary so that the direction of crack growth changes by θ and the crack grows to point 2.

The tearing modulus, T_R, [110] defined as

$$T_R = \left(\frac{E}{\sigma_0^2}\right) \frac{dJ}{d(\Delta a)} \tag{5.1}$$

is calculated by identifying dJ with $(J_2 - J_1)$ and identifying Δa with $(\Delta a_2 - \Delta a_1)$ where points

1 and 2 are shown in the inset of Fig. 5.2. The length of the unit event grain boundary facet is taken to be such that $\Delta a_2 - \Delta a_1 = 100e/\tan\theta$.

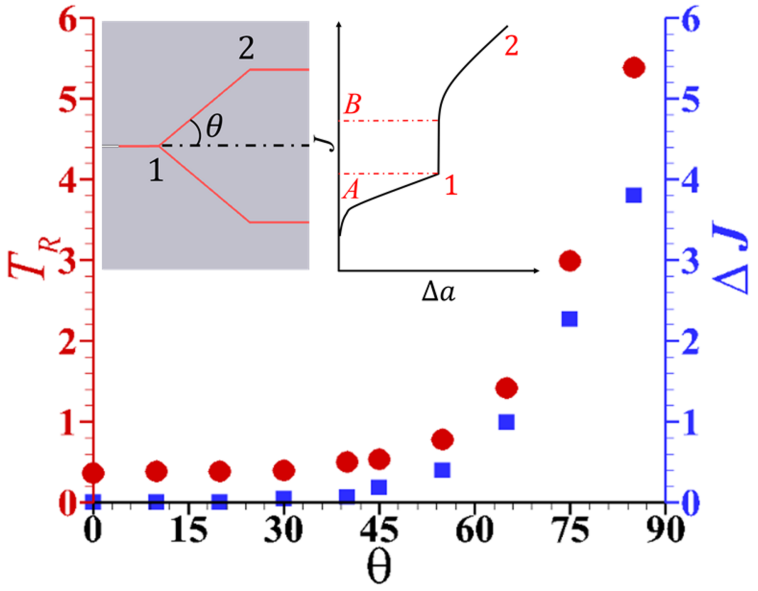

Figure 5.2: The tearing modulus, T_R (circles) of a crack propagating along a grain boundary oriented at angle θ with respect to the plane of crack propagation and the increment in $J/(\sigma_0 e)$, ΔJ (squares) arising from the crack reaching triple junction, as shown in the inset.

5.2.4 Intergranular fracture prediction as graph search

The aim is to calculate the crack path and crack growth resistance in a microstructure for which the position, orientation and segment length of each grain boundary is known. To this end, the graph search procedure used here is described in more detail in [21, 96]. With each grain boundary junction taken to be a node on a graph, all crack growth trajectories through the microstructure are obtained using a breadth-first search algorithm [111]. The crack growth resistance curve for a given crack path through the grain boundary network is obtained from a similar graph built in $J-$resistance space using the unit event crack growth resistance data in Fig. 5.2. Once constructed, the graph contains information regarding the crack growth resistance for every possible crack path in a given microstructure. The path of least resistance for a specified amount of crack growth can

then be found using Dijkstra's algorithm [112]. Dijkstra's algorithm is a graph search algorithm that produces the minimal distance between two nodes. The distances in this case are the increments in J for a crack traversing between two nodes. The current unit event based graph search model does not account for the crack branching that can sometimes occur.

5.3 Results

Here, results for the crack path and the crack growth resistance predicted using both the microstructure-based finite element calculations and the unit event based graph search model are presented. For the model based on discrete unit events and graph search the crack growth resistances are shown for three crack paths: (i) a path termed 'Local minimum - T_R' where at each grain boundary junction the path with the smallest value of T_R for one of the junction grain boundaries is chosen; (ii) a path termed 'Local minimum - ΔJ' where at each grain boundary junction the path with the smallest value of ΔJ for crack growth over two grain boundary junctions (calculations were also carried out using the 'Local minimum - ΔJ' criterion for growth over one grain boundary but the resulting crack paths differed little from those obtained using the 'Local minimum - T_R' criterion so only the results for growth over two grain boundaries are shown); and (iii) a path termed 'Global minimum' which is the path with the global minimum crack growth resistance using the 'Local minimum-ΔJ' criterion for all possible crack paths from the initial crack tip location to the end of the fine mesh region. Once the crack path is chosen, the unit event based normalized value of $\Delta J/\sigma_0 e$ is computed for each increment of normalized crack growth, $\Delta a/e$, where Δa is the change in crack length projected onto the $x-$axis.

The modeling aims to isolate the influence of variations in grain size distribution on the crack growth resistance. Crystallographic anisotropy or changes are not accounted for in material response that may change with grain size, for example, a layer may have a crystallographic texture and a Hall-Petch effect may lead to different grain sizes having different flow strengths. In the calculations, the grains are isotropic and the flow strength is independent of grain size.

For both the full field finite element calculations and the unit event based graph search model, predicted crack path and crack growth resistance curves are shown for $\Delta a \leq 800e$ in order to

avoid effects arising from the change in element size at the end of the fine mesh region which occurs at $\Delta a = 1000e$. In addition, for the calculations here, the main crack path is confined within $-300e \leq y \leq 300e$ which defines the fine mesh region in the $y-$direction.

5.3.1 Effect of grain size

Full field finite element calculations are carried out for three microstructures with unimodal grain size distributions and with values of the average grain size $D_g = 37.5e$, $D_g = 40e$ and $D_g = 43e$. Fig. 5.3 shows the computed crack growth resistance curves, J computed from Eq. (**??**), versus $\Delta a/e$. The value of $J/(\sigma_0 e)$ increases with increasing grain size, varying at $\Delta a/e = 800$ from 44 for $D_g = 37.5e$ to 54 for $D_g = 43e$, an increase of about 23%.

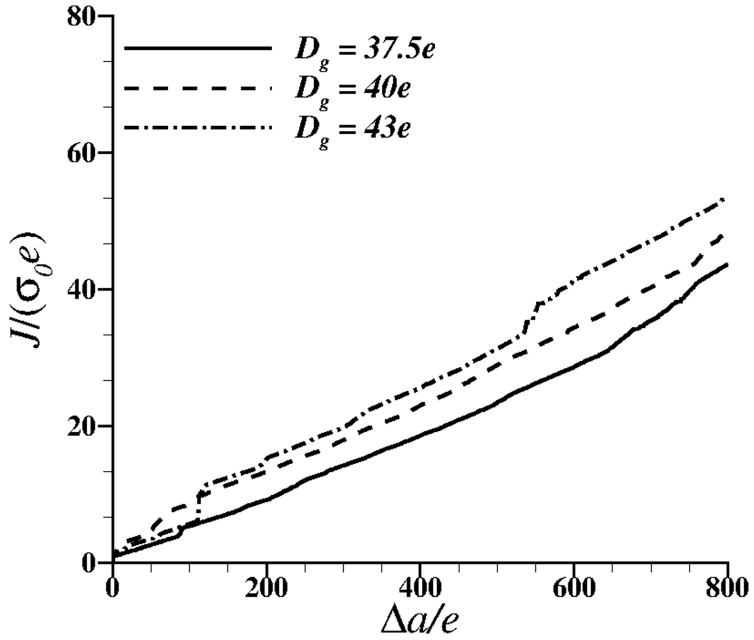

Figure 5.3: Comparison of normalized J, $J/(\sigma_0 e)$, versus normalized crack extension, $\Delta a/e$, curves from full field finite element calculations for three unimodal grain size distributions with average grain sizes, $D_g = 37.5e$, $D_g = 40e$ and $D_g = 43e$.

Fig. 5.4 compares the full field finite element predictions for crack growth resistance and crack path with those of the simple model based on unit events and graph search. Fig. 5.4(a) shows the

comparisons for $D_g = 37.5e$ while Fig. 5.4(b) shows the comparisons for $D_g = 43e$. The black line shows the predictions of the full field finite element analysis. The model predictions of the normalized value of J, $J/(\sigma_0 e)$, are shown along with three crack paths: (i) the green line is the crack path predicted by the "global minimum" criterion, (ii) the red line is the crack path predicted by the local minimum T_R criterion and (iii) the blue line is the crack path predicted by the local minimum ΔJ criterion.

With $D_g = 37.5e$, Fig. 5.4(a), the full field finite element results and the global minimum based unit event model predictions nearly coincide. This is because the full field finite element crack path and that obtained from the global minimum based unit event model nearly coincide except near the end of the region shown, $\Delta a/e \geq 650$, where the full field finite element results show crack branching. However, this only leads to a small difference in the crack growth resistance. At $\Delta a/e = 800$, $J/(\sigma_0 e)$ is 43 for the full field finite element calculation and 40 for the global minimum based unit event model crack path. The crack path obtained using the local minimum T_R criterion and the crack path obtained using the local minimum ΔJ criterion give increased values of $J/(\sigma_0 e)$. For example, at $\Delta a/e = 800$, the local minimum ΔJ criterion predicts $J/(\sigma_0 e) = 47$ and that using the local minimum T_R criterion gives $J/(\sigma_0 e) = 50$.

Fig. 5.4(b) shows corresponding results for $D_g = 43e$. In this case, the full field finite element crack path and that obtained from the global minimum based unit event model coincide until $\Delta a/e \approx 300$ and differ significantly thereafter. The predicted values for the crack growth resistance, $J/(\sigma_0 e)$, at $\Delta a/e = 800$ are 54 for the finite element calculation, 55 for the crack path obtained using the local minimum T_R criterion and 48 for the crack path obtained using the local minimum ΔJ criterion.

Fig. 5.4 shows that which unit event based graph search model gives the best fit to a particular finite element calculation can vary with grain size. Nevertheless, the full field finite element calculations and the unit event based graph search model predictions agree that a change in average grain size from $D_g = 37.5e$ to $D_g = 43e$ gives an increase in crack growth resistance. However, it is important to note that the results here are obtained for a single realization of a statistical

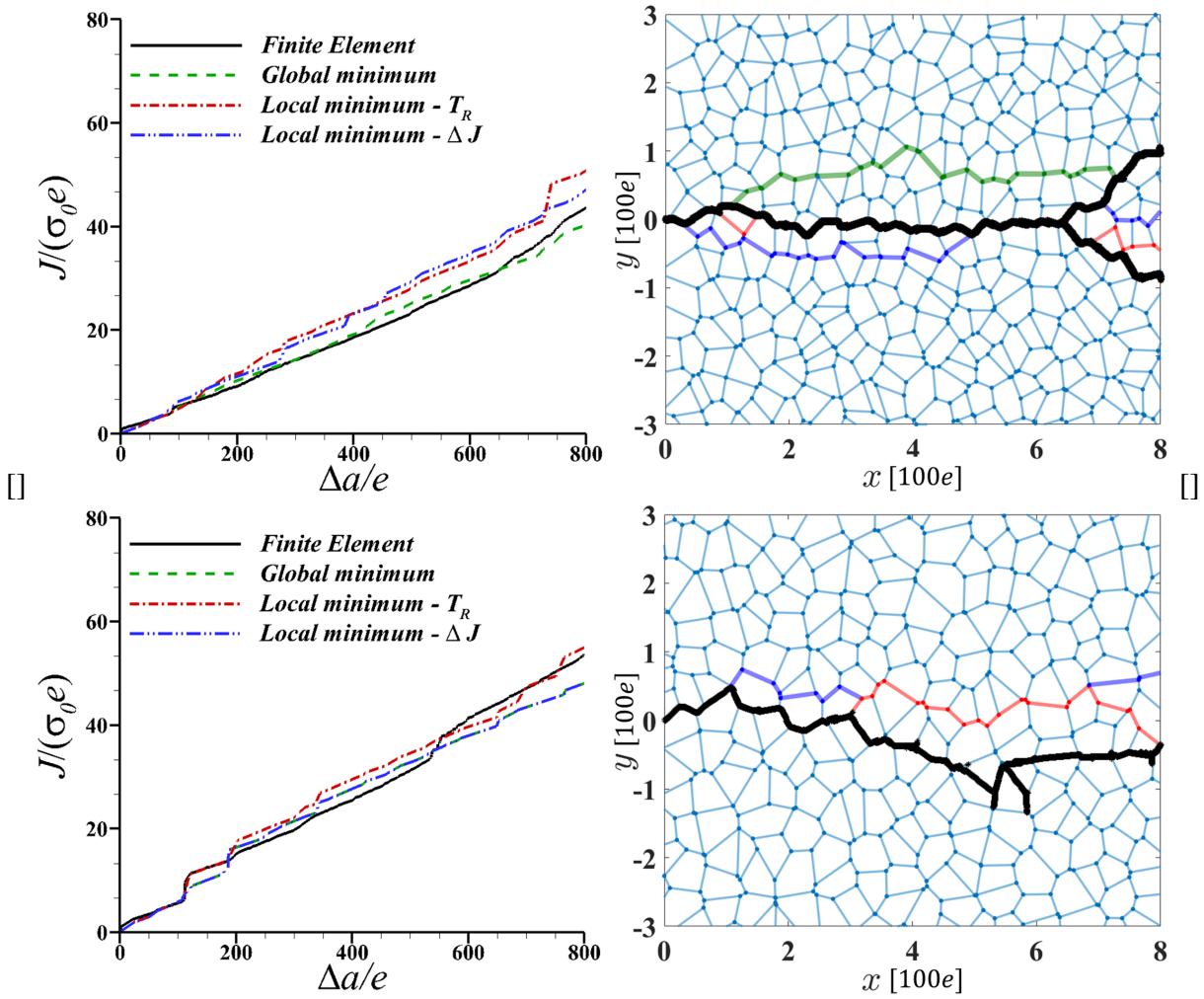

Figure 5.4: Comparison of curves of normalized J, $J/(\sigma_0 e)$, versus normalized crack extension, $\Delta a/e$ for unimodal grain siize distributions. Unit event based graph search model results are shown for the global minimum path; the local minimum path using the T_R criterion; and the local minimum path using the ΔJ criterion. Also, the crack path obtained from full field finite element calculations (black) is compared with the crack path obtained using the local minimum-T_R criterion (red), the local minimum-J criterion (blue) and the global crack path (green). Portions of these crack paths overlap. (a) $D_g = 37.5e$ and (b) $D_g = 43e$.

distribution with a specified mean grain size.

5.3.2 Bimodal grain size distribution - increasing average grain size

Fig. 5.5 shows full field finite element calculation results for crack growth resistance curves for three bimodal grain size distributions. The grain size in the type I regions have an average grain

size of $37.5e$. The bimodal grain size distributions have average grain sizes of $41.4e$, $48.9e$ and $58.5e$ in the type II regions. For comparison purposes, the results for a uniform grain size of $37.5e$ are also shown. The crack growth resistance increases with increasing heterogeneity. The value of $J/(\sigma_0 e)$ at $\Delta a = 800e$ increases from 44 for the uniform distribution to 58 for the case where the average grain size in the type II regions is $58.5e$, about a 31% increase. By way of contrast, the values $J/(\sigma_0 e)$ at $\Delta a = 800e$ show only a relatively small increase for the cases with average grain sizes of $41.4e$ and $48.9e$ in the type II regions being $J/(\sigma_0 e) = 48$ and $J/(\sigma_0 e) = 49$, respectively.

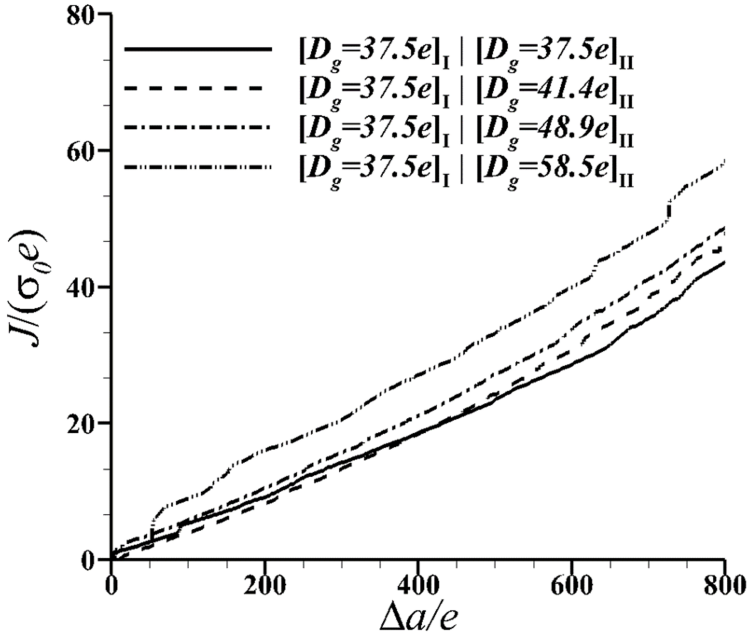

Figure 5.5: Comparison of normalized J, $J/(\sigma_0 e)$, versus normalized crack extension, $\Delta a/e$, curves computed from full field finite element calculations for four bimodal grain size distributions with a fixed average grain size in region I and an increased grain size distribution in region II, as shown in Fig.5.6.

The crack growth resistance curves and the crack paths for the cases with an average grain size of $37.5e$ in the type I regions and average grain sizes of $41.4e$ and $58.5e$ in the type II regions are shown in Fig. 5.6. In Fig. 5.6(a), where average grain size in the type II regions is $41.4e$, the

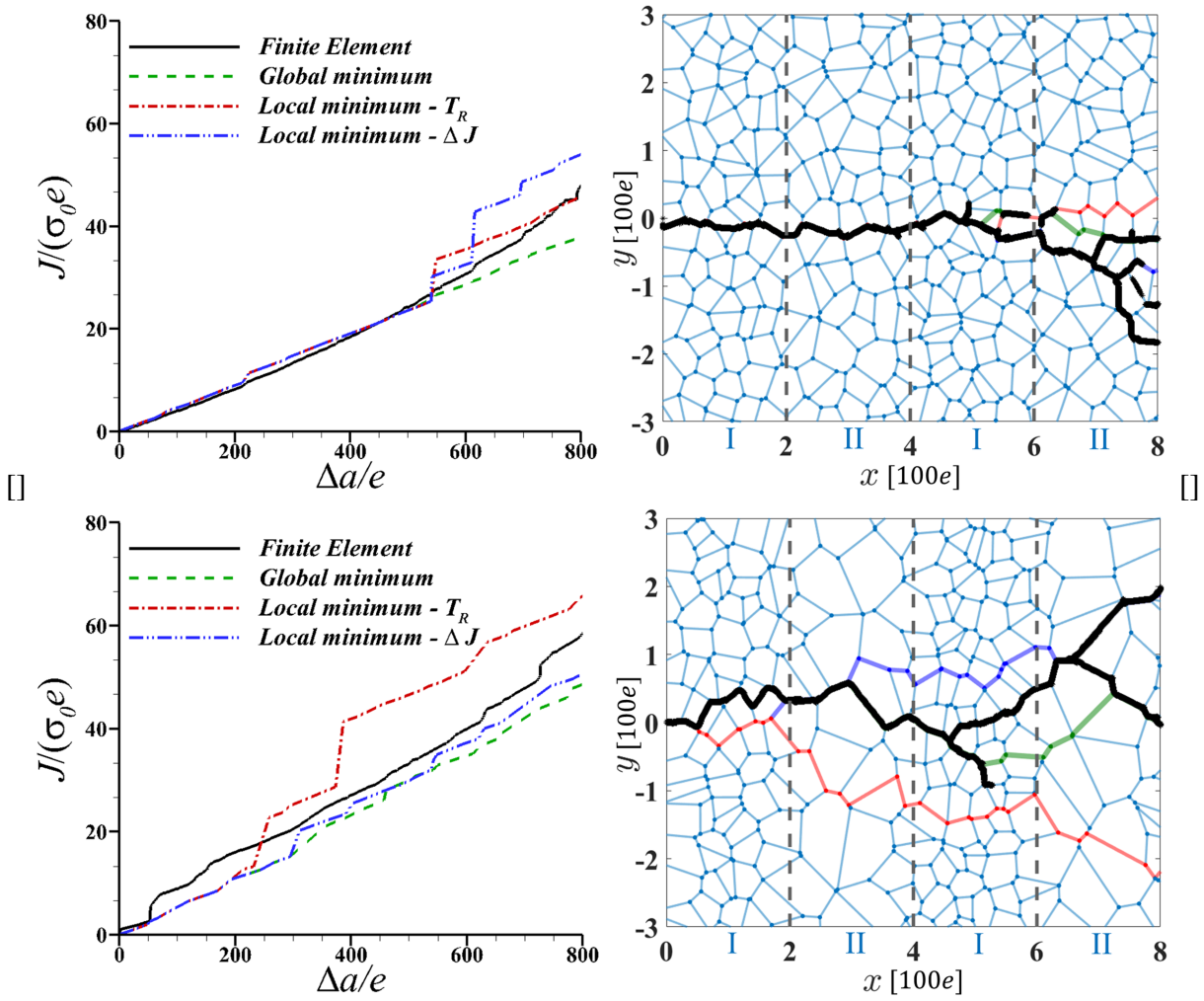

Figure 5.6: Comparison of curves of normalized J, $J/(\sigma_0 e)$, versus normalized crack extension, $\Delta a/e$ for bimodal grain size distributions with a fixed average grain size in region I and an increased grain size distribution in region II. Unit event based graph search model results are shown for the global minimum path; the local minimum path using the T_R criterion; and the local minimum path using the ΔJ criterion. Also, the crack path obtained from full field finite element calculations (black) is compared with the crack path obtained using the local minimum-T_R criterion (red), the local minimum-J criterion (blue) and the global minimum criterion (green). Portions of these crack paths overlap. (a) $D_g = 37.5e$ in region I and $D_g = 41.4e$ in region II. (b) $D_g = 37.5e$ in region I and $D_g = 58.5e$ in region II.

full field finite element predictions and all three predictions obtained from the unit event based graph search models are in close agreement until $\Delta a/e \approx 600$, the beginning of the second type II region. The predicted crack growth resistance curves then begin to differ considerably. In this case

the finite element predictions most closely agree with the simple model results obtained using local minimum T_R criterion. At $\Delta a/e = 800$, the value of $J/(\sigma_0 e)$ obtained using the global minimum criterion is about 38 while the local minimum ΔJ criterion is 54. The full field finite element calculations give $J/(\sigma_0 e) = 47$ while the simple model based on local minimum T_R criterion predicts 46.

In Fig. 5.6(a), the predicted crack path using all the unit event based graph search model are in good agreement with the full field finite element results until $\Delta a/e \approx 550$ at which point the simple model prediction using local minimum T_R criterion predicts a rather abrupt increase in $J/(\sigma_0 e)$. The associated predicted crack path (red curve) obtained using the local minimum T_R criterion follows a small grain boundary segment that results in a very small change in Δa whereas the full field finite element calculation leads to short micro-cracks along that path while the main crack follows another path. The value of $J/(\sigma_0 e)$ predicted using the local minimum ΔJ criterion gives a smaller increase at this point. This difference is probably associated with the 'Local minimum - T_R' crack path being based on one grain boundary segment whereas the 'Local minimum - ΔJ' is based on two grain boundary segments.

Fig. 5.6(b) shows the results for a case where the average grain size in the type I regions is $37.5e$, same as in Fig. 5.6(a), but the average grain size in type II regions is $58.5e$. The $J/(\sigma_0 e)$ versus Δa curve obtained from the full field finite element calculation shows increases in $J/(\sigma_0 e)$ associated with crack branching. The simple model prediction using local minimum T_R criterion also shows fairly abrupt increase in $J/(\sigma_0 e)$ correlated with the boundaries of the first type II region which are not seen in the full field finite element result. In the finite element results, having a larger grain size in the type II regions leads to more extended branched cracks which increases the crack growth resistance.

In Fig. 5.6(a) the unit event based graph search model using the local minimum ΔJ criterion significantly over predicts the crack growth resistance. On the other hand, in Fig. 5.6(b) the simple model using local minimum T_R criterion significantly over predicts the crack growth resistance, whereas the unit event model using the local minimum ΔJ criterion under predicts the crack

growth resistance and is close to the prediction of the global minimum criterion. Also, for certain type I region/type II region interfaces a local minimum criterion predicts a more abrupt increase in $J/\left(\sigma_0 e\right)$ than obtained in the full field finite element calculation.

5.3.3 Bimodal grain size distribution - fixed average grain size

Results of three full field finite element calculations for bimodal grain size distributions where the average grain size is fixed at $37.5e$ are shown in Fig. 5.7. In the type I regions, the values of average grain size are $D_g = 34.6e$, $D_g = 31.6e$ and $D_g = 29.8e$. The corresponding grain sizes in the type II regions are $D_g = 41.4e$, $D_g = 48.9e$ and $D_g = 58.5e$, respectively. For comparison purposes, the crack growth resistance curve for a uniform grain size distribution with $D_g = 37.5e$ is also shown.

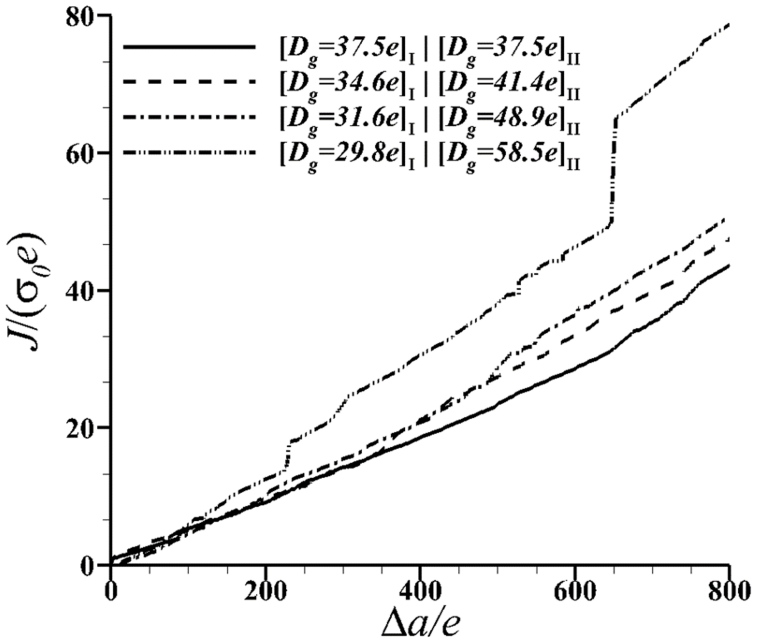

Figure 5.7: Comparison of curves of normalized J, $J/\left(\sigma_0 e\right)$, versus normalized crack extension, $\Delta a/e$, computed from full field finite element calculations for four bimodal grain size distributions with a decreased grain size in region I and an increased grain size distribution in region II, as shown in Fig.5.8.

Increasing the difference in grain size between the regions can significantly increase the crack growth resistance. With the bimodal distribution $[D_g = 34.6e]_I$, $[D_g = 41.4e]_{II}$ the value of $J/(\sigma_0 e)$ at $\Delta a/e = 800$ is 47. The corresponding value of $J/(\sigma_0 e)$ with $[D_g = 31.6e]_I$, $[D_g = 48.9e]_{II}$ is 51 and with $[D_g = 29.8e]_I$, $[D_g = 58.5e]_{II}$ is 79. For comparison, with a uniform grain size $D_g = 37.5e$, $J/(\sigma_0 e) = 44$ at $\Delta a/e = 800$.

The value of $J/(\sigma_0 e) = 79$ at $\Delta a/e = 800$ with $[D_g = 29.8e]_I$, $[D_g = 58.5e]_{II}$ may be a numerical artifact since (as seen in Fig. 5.8) the path of one of the crack branches at $\Delta a/e \approx 600$ reaches the upper, $y = 300e$, boundary of the fine mesh region. Nevertheless, even discounting this large jump, the crack growth resistance curve for $[D_g = 29.8e]_I$, $[D_g = 58.5e]_{II}$ shows that a large grain size difference in a bimodal grain size distribution can significantly increase the crack growth resistance. For example, at $\Delta a/e = 500$, $J/(\sigma_0 e) = 24$ for a uniform grain size of $D_g = 37.5e$, while $J/(\sigma_0 e) = 38$ for the bimodal distribution with $[D_g = 29.8e]_I$, $[D_g = 58.5e]_{II}$, which is about a 58% increase.

Fig. 5.8 shows comparisons between full field finite element calculations and unit event based graph search model predictions for $[D_g = 34.6e]_I$, $[D_g = 41.4e]_{II}$, Fig. 5.8(a), and for $[D_g = 29.8e]_I$, $[D_g = 58.5e]_{II}$, Fig. 5.8(b). In Fig. 5.8(a), the full field finite element crack path and the simple model based on global minimum criterion crack path nearly coincide as do the crack growth resistance curves. On the other hand in Fig. 5.8(b) the full field finite element crack path exhibits branching and associated with each branch is a jump in $J/(\sigma_0 e)$. As a consequence, none of the crack path predicted using the unit event based graph search model coincide with the finite element predictions. As noted previously, one of the branches impinges on the fine mesh region boundary $y = 300e$ at $\Delta a/e \approx 650$ which probably accounts for the very large jump in $J/(\sigma_0 e)$ at this value of $\Delta a/e$.

The full field finite element results for a bimodal layered microstructure in Figs. 5.5 and 5.7 show that if the difference in grain size is sufficiently large, a significant increase in crack growth resistance for materials that fail by grain boundary crack growth can be achieved. Furthermore, the crack paths in Figs. 5.6 and 5.8 show that a bimodal layered grain size distribution enhances

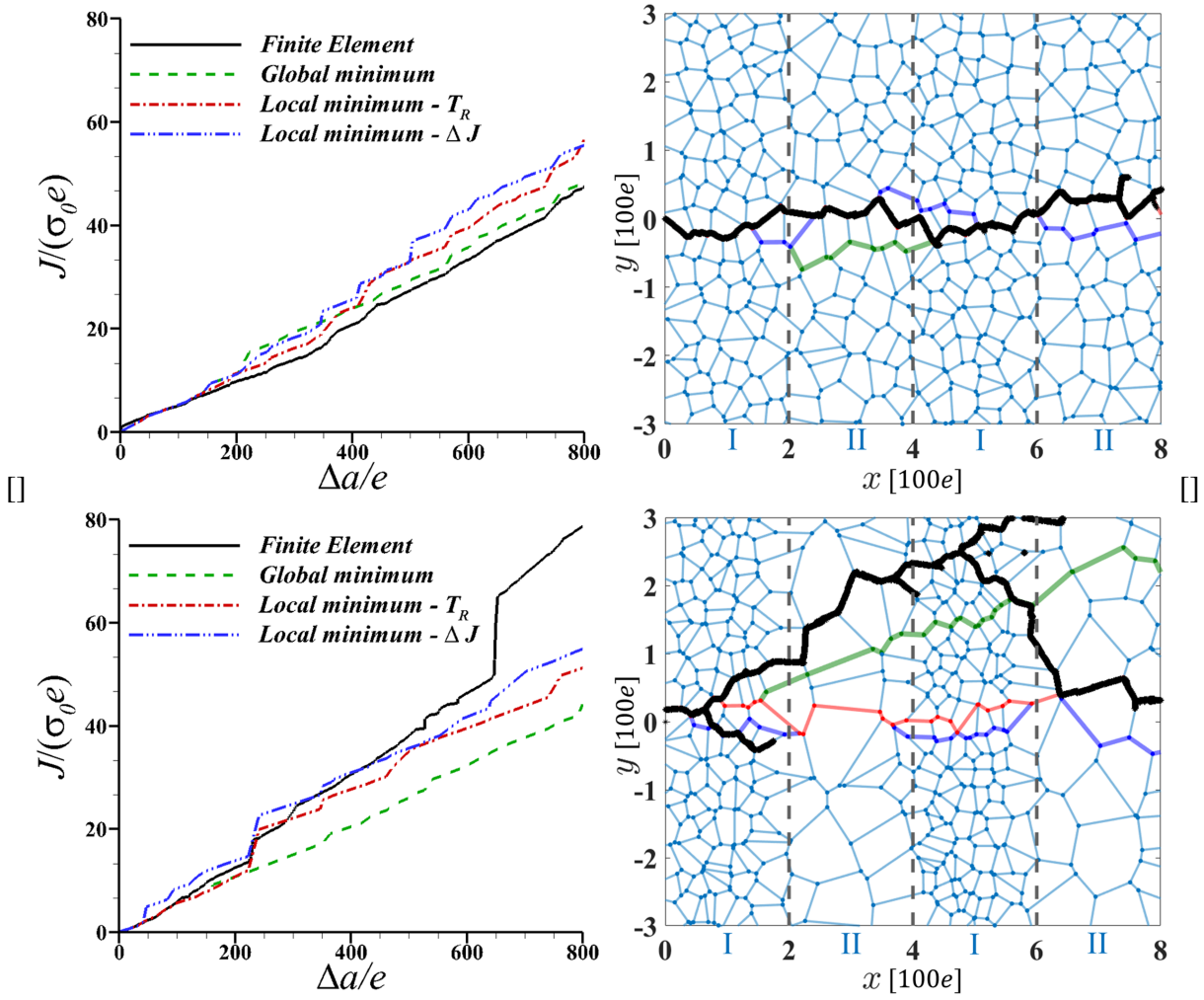

Figure 5.8: Comparison of curves of normalized J, $J/(\sigma_0 e)$, versus normalized crack extension, $\Delta a/e$, for bimodal grain size distributions with a decreased grain size in region I and an increased grain size distribution in region II. Unit event based graph search model results are shown for the global minimum path; the local minimum path using the T_R criterion; and the local minimum path using the ΔJ criterion. Also, the crack path obtained from full field finite element calculations (black) is compared with the crack path obtained using the local minimum-T_R criterion (red), the local minimum-J criterion (blue) and the global minimum criterion (green). Portions of these crack paths overlap. (a) $D_g = 34.6e$ in region I and $D_g = 41.4e$ in region II. (b) $D_g = 29.8e$ in region I and $D_g = 58.5e$ in region II.

the crack growth resistance by altering the crack path near the interfaces and by crack branching. These results indicate that by arranging the grains with different average grain sizes in layers is advantageous for materials that undergo grain boundary fracture, as seen experimentally for other

materials and other fracture mechanisms, e.g. [106, 107, 108].

5.4 Summary

Analyses of ductile intergranular crack growth are carried out with the aim of isolating the influence of variations in grain size distribution on crack growth resistance. Analyses were carried out for three grain size distributions; (i) a unimodal distribution; (ii) a bimodal layered distribution consisting of alternate layers with the grain size in one layer type held fixed and with an increased grain size in the other layer type; and (iii) a bimodal layered distribution consisting of alternate layers with a decreased grain size in one layer type and an increased grain size in the other layer type. In (ii) the overall average grain size increases while in (iii) the overall average grain size is fixed.

The results show that for both unimodal and bimodal grain size distributions, the crack growth resistance increases with increasing overall average grain size. For the bimodal distribution where the overall average grain size is fixed, the crack growth resistance increases with an increasing difference between the average grain size in the two layer types. Hence, a combination of layered smaller grain size regions that have a lower crack growth resistance together with larger grain size regions that have greater crack growth resistance can lead to a material with greater crack growth resistant than a uniform microstructure with large grains. It is worth noting that a wide variety of natural materials rely on a structure consisting of alternating regions of reduced and enhanced crack growth resistance to attain superior overall crack growth resistance [113, 114, 115, 116].

In [96], for unimodal grain size distributions, in the absence of crack branching, the unit event based graph search model with a local minimum ΔJ crack path selection criterion gave good quantitative agreement with the full field finite element predictions. In the calculations here, for the unit event based graph search model, all criteria considered are in qualitative agreement with the full field finite element calculations but none of the criteria used with the unit event based graph search model gave a good quantitative agreement with the full field finite element results for all grain microstructures analyzed. One possible reason for this is that the thickness of the grain boundaries here is greater than that in [96], so that finite deformation effects may play a greater

role in the full field finite element calculations, leading, for example, to plastic deformations at some crack tips along the path extending over more grains in some distributions than in others. Nevertheless, the global minimum criterion does provide a lower estimate of the crack growth resistance in all cases analyzed.

A grain size distribution that maximizes the dissipation during crack growth can be realized, at least in principle, by some sort of iterative optimization method. One way to calculate the crack growth resistance through a grain size distribution is to carry out microstructure-based full field finite element calculations. However, such calculations, especially for three dimensional grain distributions, are extremely time consuming. For an iterative optimization scheme what is needed is a computationally efficient procedure that can correctly rank the crack growth resistance of possible grain size distributions. The computationally efficient simple model based on discrete unit events and graph search developed in [96], and used here, holds promise for this purpose. A more generally predictive crack path selection criterion would enhance the utility of the discrete unit event and graph search model for microstructure optimization purposes.

The results in [96] and here indicate that the unit event based graph search model can at least provide a qualitative prediction of the crack growth resistance when crack branching does not occur. However, the full field finite element results show that crack branching can play a significant role in the increased crack growth resistance of the layered grain size microstructures. Incorporating crack branching into the model will increase its predictive capability so that it can become an engineering tool for optimizing material microstructures to enhance crack growth resistance.

6. CONCLUDING REMARKS AND FUTURE WORK

6.1 Concluding Remarks

In this work, an attempt was made to develop and demonstrate novel material design approaches to enable accelerated goal-oriented materials design. The focus of a goal-oriented material design process is to predict the combinations of material chemistry and processing route that yields a material with targeted properties which is enabled by understanding and exploiting processing/chemistry - microstructure - property (PSP) relationships. The state-of-the art design frameworks to carry out goal-oriented material design tend to use a single source of information/data to exploit the PSP relationship. However, often there are multiple information sources (experiments, computational models, empirical models) with varying degrees of fidelity and cost that can be used to potentially exploit the PSP linkages to carry out a goal-oriented material design. Following this, in Chapter 2, the applicability of a closed-loop multi-fidelity Bayesian Optimization framework capable of exploiting multiple information/data sources with varying fidelity and cost to efficiently carry out goal-oriented material design is demonstrated. The material design framework utilized the Knowledge Gradient metric to efficiently balance the need to explore and exploit knowledge of the materials design space in order to find an optimal solution in as efficient manner as possible. The framework also enabled the selection of the most cost-effective information source to query the material design space under budget constraint.

While fundamentally materials science involves the study of processing/chemistry - microstructure - property correlations, in practice, material design involves finding optimum processing/chemistry that yields desired properties, and the microstructure information is either only used to establish the PSP linkage for simulations or rationalize the final observations or both. This raises a fundamental question, can the intermediate microstructural information aid in searching for optimum processing/chemistry that yield desired properties more efficiently than otherwise. To answer this question, in Chapter 3, a novel microstructure aware closed-loop multi-fidelity Bayesian Optimization

framework is formulated to probe the importance of microstructure information on a goal-oriented design process. The results show that explicitly including the microstructure information in the decision-making process can significantly accelerate the material design process.

Furthermore, there are several material design problems in which the target property is sensitive to the topological details of the material microstructure. For example, crack growth resistance of a material microstructure. Materials design problems involving optimization of the crack growth resistance through microstructure design requires systematic optimization of the topological features of the material's microstructure. While existing methodologies such as microstructure-based finite element calculations to correlate relevant features of a material's microstructure and its resistance to crack growth are reasonably accurate, they tend to be computationally expensive. Thus, closed-loop design of material microstructures targeting crack growth resistance using such expensive microstructure-based finite element calculations is impractical and requires computationally efficient methods to predict the crack path and its crack growth resistance in a given material microstructure. To address this need, in Chapter 4, a novel computationally efficient method utilizing evolving graphs and microstructural unit events is proposed to predict crack path and crack growth resistance. The predictions from the method based on evolving graphs and microstructural unit events are compared with the results of full-field microstructure-based finite element calculations of ductile fracture. Finally, this approach is used to design material microstructures with enhanced intergranular crack growth resistance in Chapter 5.

6.2 Future Work

The work presented in this dissertation provides a motivation for several directions to be investigated in the future.

- In most materials design problems, the objective function is more sensitive to some input variables compared to others. Exploiting such information can lead to even faster and more efficient materials design process. For example, in Chapter 3, not all dimensions of the material design space are equally influential in optimization of the target property. This points

to a possible strategy to make this framework even faster and more efficient: find and follow directions (i.e. subspaces) in the design space along which the gradient of objective function is highest. This approach, known as the active subspace method [73, 74], decomposes the design space in such a way that at any time only the most influential or active subspaces are considered when trying to find the optimum in a multi-dimensional space. Effectively, this approach would reduce the dimension of the problem, accelerating the rate at which the solution is approached. Active subspace approach in conjunction with microstructure aware approach could be used to accelerate the design process even further.

- Engineering design problems more often than not require optimization of more than one material properties for desired application. Thus, the material design design framework developed in Chapter 3 could be extended to handle multiple objectives.

- The novel approach based on evolving graphs and microstructural unit events proposed in Chapter 4 could be used in a closed-loop optimization framework to accelerate the process of designing fracture resistant materials.

- The proposed novel approach in Chapter 4 based on evolving graphs and microstructural unit events focused on assessing the crack growth resistance of two-dimensional material microstructures. Hence, am immediate next step will be to generalize this method to account for three-dimensional material microstructures.

REFERENCES

[1] G. B. Olson, "Computational design of hierarchically structured materials," *Science*, vol. 277, no. 5330, pp. 1237–1242, 1997.

[2] G. B. Olson, "Designing a new material world," *Science*, vol. 288, no. 5468, pp. 993–998, 2000.

[3] D. L. McDowell, "Simulation-assisted materials design for the concurrent design of materials and products," *JOM*, vol. 59, no. 9, pp. 21–25, 2007.

[4] J. Allison, "Integrated computational materials engineering: A perspective on progress and future steps," *JOM*, vol. 63, no. 4, pp. 15–18, 2011.

[5] N. R. Council *et al.*, *Integrated computational materials engineering: a transformational discipline for improved competitiveness and national security*. National Academies Press, 2008.

[6] J. P. Holdren *et al.*, "Materials genome initiative for global competitiveness," *National Science and Technology Council OSTP. Washington, USA*, 2011.

[7] The Minerals Metals & Materials Society (TMS), *Modeling Across Scales: A Roadmapping Study for Connecting Materials Models and Simulations Across Length and Time Scales*. Warrendale, PA: TMS, 2015.

[8] L. Lin and W. Ren, "An implementation of icme in materials information exchanging interfaces," *Materials discovery*, vol. 12, pp. 9–19, 2018.

[9] D. Khatamsaz, A. Molkeri, R. Couperthwaite, J. James, R. Arróyave, D. Allaire, and A. Srivastava, "Efficiently exploiting process-structure-property relationships in material design by multi-information source fusion," *Acta Materialia*, vol. 206, p. 116619, 2021.

[10] A. Talapatra, S. Boluki, T. Duong, X. Qian, E. Dougherty, and R. Arróyave, "Autonomous efficient experiment design for materials discovery with bayesian model averaging," *Physical Review Materials*, vol. 2, no. 11, p. 113803, 2018.

[11] A. Solomou, G. Zhao, S. Boluki, J. K. Joy, X. Qian, I. Karaman, R. Arróyave, and D. C. Lagoudas, "Multi-objective bayesian materials discovery: Application on the discovery of precipitation strengthened niti shape memory alloys through micromechanical modeling," *Materials & Design*, vol. 160, pp. 810–827, 2018.

[12] P. V. Balachandran, D. Xue, J. Theiler, J. Hogden, and T. Lookman, "Adaptive strategies for materials design using uncertainties," *Scientific reports*, vol. 6, 2016.

[13] S. F. Ghoreishi, A. Molkeri, A. Srivastava, R. Arroyave, and D. Allaire, "Multi-information source fusion and optimization to realize icme: Application to dual-phase materials," *Journal of Mechanical Design*, vol. 140, no. 11, p. 111409, 2018.

[14] B. Peherstorfer, K. Willcox, and M. Gunzburger, "Survey of multifidelity methods in uncertainty propagation, inference, and optimization," *Siam Review*, vol. 60, no. 3, pp. 550–591, 2018.

[15] S. Wei, S. J. Kim, J. Kang, Y. Zhang, Y. Zhang, T. Furuhara, E. S. Park, and C. C. Tasan, "Natural-mixing guided design of refractory high-entropy alloys with as-cast tensile ductility," *Nature Materials*, vol. 19, no. 11, pp. 1175–1181, 2020.

[16] A. Devaraj, V. V. Joshi, A. Srivastava, S. Manandhar, V. Moxson, V. A. Duz, and C. Lavender, "A low-cost hierarchical nanostructured beta-titanium alloy with high strength," *Nature communications*, vol. 7, no. 1, pp. 1–8, 2016.

[17] Z. Li, K. G. Pradeep, Y. Deng, D. Raabe, and C. C. Tasan, "Metastable high-entropy dual-phase alloys overcome the strength–ductility trade-off," *Nature*, vol. 534, no. 7606, pp. 227–230, 2016.

[18] J.-W. Yeh, S.-K. Chen, S.-J. Lin, J.-Y. Gan, T.-S. Chin, T.-T. Shun, C.-H. Tsau, and S.-Y. Chang, "Nanostructured high-entropy alloys with multiple principal elements: novel alloy

design concepts and outcomes," *Advanced Engineering Materials*, vol. 6, no. 5, pp. 299–303, 2004.

[19] Y. Liu, D. Fan, S. P. Bhat, and A. Srivastava, "Ductile fracture of dual-phase steel sheets under bending," *International Journal of Plasticity*, vol. 125, pp. 80–96, 2020.

[20] A. Srivastava, S. Osovski, and A. Needleman, "Engineering the crack path by controlling the microstructure," *Journal of the Mechanics and Physics of Solids*, vol. 100, pp. 1–20, 2017.

[21] S. Osovski, A. Srivastava, J. C. Williams, and A. Needleman, "Grain boundary crack growth in metastable titanium β alloys," *Acta Materialia*, vol. 82, pp. 167–178, 2015.

[22] A. Srivastava, H. Ghassemi-Armaki, H. Sung, P. Chen, S. Kumar, and A. F. Bower, "Micromechanics of plastic deformation and phase transformation in a three-phase trip-assisted advanced high strength steel: Experiments and modeling," *Journal of the Mechanics and Physics of Solids*, vol. 78, pp. 46–69, 2015.

[23] A. Srivastava, A. Bower, L. Hector Jr, J. Carsley, L. Zhang, and F. Abu-Farha, "A multi-scale approach to modeling formability of dual-phase steels," *Modelling and Simulation in Materials Science and Engineering*, vol. 24, no. 2, p. 025011, 2016.

[24] P. Voorhees, G. Spanos, *et al.*, "Modeling across scales: a roadmapping study for connecting materials models and simulations across length and time scales," tech. rep., Tech. rep., The Minerals, Metals & Materials Society (TMS), 2015.

[25] S. Reddy, B. Gautham, P. Das, R. R. Yeddula, S. Vale, and C. Malhotra, "An ontological framework for integrated computational materials engineering," in *Proceedings of the 4th World Congress on Integrated Computational Materials Engineering (ICME 2017)*, pp. 69–77, Springer, 2017.

[26] V. Savic, L. Hector, U. Basu, A. Basudhar, I. Gandikota, N. Stander, T. Park, F. Pourboghrat, K. S. Choi, X. Sun, *et al.*, "Integrated computational materials engineering (ICME)

multi-scale model development for advanced high strength steels," tech. rep., SAE Technical Paper, 2017.

[27] M. Diehl, M. Groeber, C. Haase, D. A. Molodov, F. Roters, and D. Raabe, "Identifying structure–property relationships through dream. 3D representative volume elements and DAMASK crystal plasticity simulations: An integrated computational materials engineering approach," *JOM*, vol. 69, no. 5, pp. 848–855, 2017.

[28] R. Potyrailo, K. Rajan, K. Stoewe, I. Takeuchi, B. Chisholm, and H. Lam, "Combinatorial and high-throughput screening of materials libraries: review of state of the art," *ACS combinatorial science*, vol. 13, no. 6, pp. 579–633, 2011.

[29] S. K. Suram, J. A. Haber, J. Jin, and J. M. Gregoire, "Generating information-rich high-throughput experimental materials genomes using functional clustering via multitree genetic programming and information theory," *ACS combinatorial science*, vol. 17, no. 4, pp. 224–233, 2015.

[30] M. L. Green, C. Choi, J. Hattrick-Simpers, A. Joshi, I. Takeuchi, S. Barron, E. Campo, T. Chiang, S. Empedocles, J. Gregoire, *et al.*, "Fulfilling the promise of the materials genome initiative with high-throughput experimental methodologies," *Applied Physics Reviews*, vol. 4, no. 1, p. 011105, 2017.

[31] S. Curtarolo, G. L. Hart, M. B. Nardelli, N. Mingo, S. Sanvito, and O. Levy, "The high-throughput highway to computational materials design," *Nature materials*, vol. 12, no. 3, pp. 191–201, 2013.

[32] A. Talapatra, S. Boluki, T. Duong, X. Qian, E. Dougherty, and R. Arroyave, "Towards an autonomous efficient materials discovery framework: An example of optimal experiment design under model uncertainty," *arXiv preprint arXiv:1803.05460*, 2018.

[33] M. Rashid, "Dual phase steels," *Annual Review of Materials Science*, vol. 11, no. 1, pp. 245–266, 1981.

[34] P. Chen, H. Ghassemi-Armaki, S. Kumar, A. Bower, S. Bhat, and S. Sadagopan, "Microscale-calibrated modeling of the deformation response of dual-phase steels," *Acta Materialia*, vol. 65, pp. 133–149, 2014.

[35] D. Gerbig, A. Srivastava, S. Osovski, L. G. Hector, and A. Bower, "Analysis and design of dual-phase steel microstructure for enhanced ductile fracture resistance," *International Journal of Fracture*, pp. 1–24, 2017.

[36] F. Feyel, "Multiscale fe2 elastoviscoplastic analysis of composite structures," *Computational Materials Science*, vol. 16, no. 1-4, pp. 344–354, 1999.

[37] E. Weinan, B. Engquist, X. Li, W. Ren, and E. Vanden-Eijnden, "Heterogeneous multiscale methods: a review," *Commun. Comput. Phys*, vol. 2, no. 3, pp. 367–450, 2007.

[38] W. Voigt, "On the relation between the elasticity constants of isotropic bodies," *Ann. Phys. Chem*, vol. 274, pp. 573–587, 1889.

[39] A. Reuss, "Berechnung der fließgrenze von mischkristallen auf grund der plastizitätsbedingung für einkristalle.," *ZAMM-Journal of Applied Mathematics and Mechanics/Zeitschrift für Angewandte Mathematik und Mechanik*, vol. 9, no. 1, pp. 49–58, 1929.

[40] O. Bouaziz and P. Buessler, "Mechanical behaviour of multiphase materials: an intermediate mixture law without fitting parameter," *Revue de Métallurgie–International Journal of Metallurgy*, vol. 99, no. 1, pp. 71–77, 2002.

[41] G. Weng, "The overall elastoplastic stress-strain relations of dual-phase metals," *Journal of the Mechanics and Physics of Solids*, vol. 38, no. 3, pp. 419–441, 1990.

[42] Dassault Systemes, *ABAQUS user's mannual*, 2017.

[43] S. Nemat-Nasser and M. Hori, *Micromechanics: overall properties of heterogeneous materials*, vol. 37. Elsevier, 2013.

[44] C. K. Williams and C. E. Rasmussen, "Gaussian processes for machine learning," *The MIT Press*, 2006.

[45] R. L. Winkler, "Combining probability distributions from dependent information sources," *Management Science*, vol. 27, no. 4, pp. 479–488, 1981.

[46] D. Allaire and K. Willcox, "Fusing information from multifidelity computer models of physical systems," in *Information Fusion (FUSION), 2012 15th International Conference on*, pp. 2458–2465, IEEE, 2012.

[47] W. D. Thomison and D. L. Allaire, "A model reification approach to fusing information from multifidelity information sources," in *19th AIAA Non-Deterministic Approaches Conference*, p. 1949, 2017.

[48] P. Frazier, W. Powell, and S. Dayanik, "The knowledge-gradient policy for correlated normal beliefs," *INFORMS Journal on Computing*, vol. 21, no. 4, pp. 599–613, 2009.

[49] J. H. Perepezko, "The hotter the engine, the better," *Science*, vol. 326, no. 5956, pp. 1068–1069, 2009.

[50] J. J. Bertin and R. M. Cummings, "Fifty years of hypersonics: where we've been, where we're going," *Progress in Aerospace Sciences*, vol. 39, no. 6-7, pp. 511–536, 2003.

[51] J. Knaster, A. Moeslang, and T. Muroga, "Materials research for fusion," *Nature Physics*, vol. 12, no. 5, pp. 424–434, 2016.

[52] B. Gautham, R. Kumar, S. Bothra, G. Mohapatra, N. Kulkarni, and K. Padmanabhan, "More efficient icme through materials informatics and process modeling," in *Proceedings of the 1st World Congress on Integrated Computational Materials Engineering (ICME)*, p. 35, Wiley Online Library, 2011.

[53] M. F. Horstemeyer, *Integrated Computational Materials Engineering (ICME) for metals: using multiscale modeling to invigorate engineering design with science*. John Wiley & Sons, 2012.

[54] D. L. McDowell and S. R. Kalidindi, "The materials innovation ecosystem: a key enabler for the materials genome initiative," *Mrs Bulletin*, vol. 41, no. 4, p. 326, 2016.

[55] R. Arróyave and D. L. McDowell, "Systems approaches to materials design: past, present, and future," *Annual Review of Materials Research*, vol. 49, pp. 103–126, 2019.

[56] W. Y. Wang, B. Tang, D. Lin, C. Zou, Y. Zhang, S.-L. Shang, Q. Guan, J. Gao, L. Fan, H. Kou, *et al.*, "A brief review of data-driven icme for intelligently discovering advanced structural metal materials: Insight into atomic and electronic building blocks," *Journal of Materials Research*, vol. 35, no. 8, pp. 872–889, 2020.

[57] R. Couperthwaite, A. Molkeri, D. Khatamsaz, A. Srivastava, D. Allaire, and R. Arròyave, "Materials design through batch bayesian optimization with multisource information fusion," *JOM*, vol. 72, no. 12, pp. 4431–4443, 2020.

[58] R. Couperthwaite, D. Allaire, and R. Arróyave, "Utilizing gaussian processes to fit high dimension thermodynamic data that includes estimated variability," *Computational Materials Science*, vol. 188, p. 110133, 2021.

[59] S. F. Ghoreishi, A. Molkeri, R. Arróyave, D. Allaire, and A. Srivastava, "Efficient use of multiple information sources in material design," *Acta Materialia*, vol. 180, pp. 260–271, 2019.

[60] D. Gerbig, A. Srivastava, S. Osovski, L. G. Hector, and A. Bower, "Analysis and design of dual-phase steel microstructure for enhanced ductile fracture resistance," *International Journal of Fracture*, vol. 209, no. 1-2, pp. 3–26, 2018.

[61] X. Zheng, H. Ghassemi-Armaki, K. T. Hartwig, and A. Srivastava, "Correlating prior austenite grain microstructure, microscale deformation and fracture of ultra-high strength martensitic steels," *Metals*, vol. 11, no. 7, p. 1013, 2021.

[62] Y. Liu, D. Fan, R. Arróyave, and A. Srivastava, "Microstructure-based modeling of the effect of inclusion on the bendability of advanced high strength dual-phase steels," *Metals*, vol. 11, no. 3, p. 431, 2021.

[63] C. E. Rasmussen and C. K. I. Williams, *Gaussian Processes for Machine Learning (Adaptive Computation and Machine Learning)*. The MIT Press, 2005.

[64] S. F. Ghoreishi and D. L. Allaire, "A fusion-based multi-information source optimization approach using knowledge gradient policies," in *2018 AIAA/ASCE/AHS/ASC Structures, Structural Dynamics, and Materials Conference*, p. 1159, 2018.

[65] W. B. Powell and I. O. Ryzhov, *Optimal Learning*, vol. 841. John Wiley & Sons, 2012.

[66] J. Mercer, "Functions of positive and negative type, and their connection the theory of integral equations," *Philosophical transactions of the royal society of London. Series A, containing papers of a mathematical or physical character*, vol. 209, no. 441-458, pp. 415–446, 1909.

[67] B. E. Boser, I. M. Guyon, and V. N. Vapnik, "A training algorithm for optimal margin classifiers," in *Proceedings of the fifth annual workshop on Computational learning theory*, pp. 144–152, 1992.

[68] B. Kramer and K. E. Willcox, "Nonlinear model order reduction via lifting transformations and proper orthogonal decomposition," *AIAA Journal*, vol. 57, no. 6, pp. 2297–2307, 2019.

[69] E. Qian, B. Kramer, B. Peherstorfer, and K. Willcox, "Lift & learn: Physics-informed machine learning for large-scale nonlinear dynamical systems," *Physica D: Nonlinear Phenomena*, vol. 406, p. 132401, 2020.

[70] E. Qian, B. Kramer, A. N. Marques, and K. E. Willcox, "Transform & learn: A data-driven approach to nonlinear model reduction," in *AIAA Aviation 2019 Forum*, p. 3707, 2019.

[71] E. Buckingham, "On physically similar systems; illustrations of the use of dimensional equations," *Physical review*, vol. 4, no. 4, p. 345, 1914.

[72] J. W. Strutt and J. W. S. B. Rayleigh, *The theory of sound*, vol. 1. Macmillan, 1877.

[73] S. F. Ghoreishi, S. Friedman, and D. L. Allaire, "Adaptive dimensionality reduction for fast sequential optimization with gaussian processes," *Journal of Mechanical Design*, vol. 141, no. 7, 2019.

[74] D. Khatamsaz, A. Molkeri, R. Couperthwaite, J. James, R. Arróyave, A. Srivastava, and D. Allaire, "Adaptive active subspace-based efficient multifidelity materials design," *Materials & Design*, p. 110001, 2021.

[75] E. W. Dijkstra *et al.*, "A note on two problems in connexion with graphs," *Numerische mathematik*, vol. 1, no. 1, pp. 269–271, 1959.

[76] A. V. Goldberg and C. Harrelson, "Computing the shortest path: A search meets graph theory.," in *SODA*, vol. 5, pp. 156–165, Citeseer, 2005.

[77] S. S. Skiena, *The algorithm design manual*. Springer International Publishing, 2020.

[78] M. J. McDermott, S. S. Dwaraknath, and K. A. Persson, "A graph-based network for predicting chemical reaction pathways in solid-state materials synthesis," *Nature communications*, vol. 12, no. 1, pp. 1–12, 2021.

[79] J. Kleinberg, "The small-world phenomenon: An algorithmic perspective," in *Proceedings of the thirty-second annual ACM symposium on Theory of computing*, pp. 163–170, 2000.

[80] J. M. Kleinberg, "Navigation in a small world," *Nature*, vol. 406, no. 6798, pp. 845–845, 2000.

[81] B. J. Kim, C. N. Yoon, S. K. Han, and H. Jeong, "Path finding strategies in scale-free networks," *Physical Review E*, vol. 65, no. 2, p. 027103, 2002.

[82] J. Jeong and P. Berman, "Low-cost search in scale-free networks," *Physical Review E*, vol. 75, no. 3, p. 036104, 2007.

[83] S. Osovski, A. Needleman, and A. Srivastava, "Intergranular fracture prediction and microstructure design," *International Journal of Fracture*, vol. 216, no. 2, pp. 135–148, 2019.

[84] S. Srivastava, M. Yaghoobi, and V. Sundararaghavan, "A graph-theoretic approach for multiscale modeling and prediction of crack propagation in polycrystalline materials," *Engineering Fracture Mechanics*, vol. 241, p. 107406, 2021.

[85] S. E. Halford and J. F. Marko, "How do site-specific dna-binding proteins find their targets?," *Nucleic acids research*, vol. 32, no. 10, pp. 3040–3052, 2004.

[86] J. M. Newby and P. C. Bressloff, "Directed intermittent search for a hidden target on a dendritic tree," *Physical Review E*, vol. 80, no. 2, p. 021913, 2009.

[87] A. Srivastava, L. Ponson, S. Osovski, E. Bouchaud, V. Tvergaard, and A. Needleman, "Effect of inclusion density on ductile fracture toughness and roughness," *Journal of the Mechanics and Physics of Solids*, vol. 63, pp. 62–79, 2014.

[88] Y. Liu, X. Zheng, S. Osovski, and A. Srivastava, "On the micromechanism of inclusion driven ductile fracture and its implications on fracture toughness," *Journal of the Mechanics and Physics of Solids*, vol. 130, pp. 21–34, 2019.

[89] S. Osovski, A. Srivastava, L. Ponson, E. Bouchaud, V. Tvergaard, K. Ravi-Chandar, and A. Needleman, "The effect of loading rate on ductile fracture toughness and fracture surface roughness," *Journal of the Mechanics and Physics of Solids*, vol. 76, pp. 20–46, 2015.

[90] A. L. Gurson, *Plastic flow and fracture behavior of ductile materials incorporating void nucleation, growth and interaction*. PhD thesis, Brown University, Providence, RI, 1975.

[91] V. Tvergaard, "Influence of voids on shear band instabilities under plane strain conditions," *International Journal of Fracture*, vol. 17, pp. 389–407, 1981.

[92] V. Tvergaard, "On localization in ductile materials containing spherical voids," *International Journal of Fracture*, vol. 18, pp. 237–252, 1982.

[93] J. R. Rice, "A path independent integral and the approximate analysis of strain concentration by notches and cracks," 1968.

[94] Y. Cohen, O. Devauchelle, H. F. Seybold, S. Y. Robert, P. Szymczak, and D. H. Rothman, "Path selection in the growth of rivers," *Proceedings of the National Academy of Sciences*, vol. 112, pp. 14132–14137, 2015.

[95] A. Srivastava, S. Osovski, and A. Needleman, "Engineering the crack path by controlling the microstructure," *Journal of the Mechanics and Physics of Solids*, vol. 100, pp. 1–20, 2017.

[96] S. Osovski, A. Needleman, and A. Srivastava, "Intergranular fracture prediction and microstructure design," *Int. J. Fract.*, vol. 216, pp. 135–148, 2019.

[97] S. P. Lynch, "Fracture of 8090 al-li plate i. short transverse fracture toughness," *Materials Science and Engineering: A*, vol. 136, pp. 25–43, 1991.

[98] G. Lüjtering and J. C. Williams, "Titanium (engineering materials and processes), second ed., springer verlag, berlin," vol. 2007.

[99] V. Uthaisangsuk, U. Prahl, and W. Bleck, "Characterisation of formability behaviour of multiphase steels by micromechanical modelling," *Int. J. Fract.*, vol. 157, pp. 55–69, 2009.

[100] D. Gerbig, A. Srivastava, S. Osovski, L. G. Hector, and A. Bower, "Analysis and design of dual-phase steel microstructure for enhanced ductile fracture resistance," *Int. J. Fract.*, vol. 209, pp. 3–26, 2018.

[101] S. Kikuchi, Y. Nakamura, A. Ueno, and K. Ameyama, "Low temperature nitriding of commercially pure titanium with harmonic structure," *Materials Transactions, Y-M*, vol. 2015822, 2015.

[102] M. Ota, S. K. Vajpai, R. Imao, K. Kurokawa, and K. Ameyama, "Application of high pressure gas jet mill process to fabricate high performance harmonic structure designed pure titanium," *Materials Transactions, M*, vol. 2014280, 2015.

[103] G. J. Fan, H. Choo, P. K. Liaw, and E. J. Lavernia, "Plastic deformation and fracture of ultrafine-grained al–mg alloys with a bimodal grain size distribution," *Acta Mater*, vol. 54, pp. 1759–1766, 2006.

[104] H. D. Kim, B. D. Han, D. S. Park, B. T. Lee, and P. F. Becher, "Novel twostep sintering process to obtain a bimodal microstructure in silicon nitride," *Journal of the American Ceramic Society*, vol. 85, pp. 245–252, 2002.

[105] Y. Fang, F. Yu, and K. W. White, "Bimodal microstructure in silicon nitride–barium aluminum silicate ceramicmatrix composites by pressureless sintering," *Journal of the American Ceramic Society*, vol. 83, pp. 1828–1830, 2000.

[106] P. F. Becher, E. Y. Sun, K. P. Plucknett, K. B. Alexander, C. H. Hsueh, H. T. Lin, S. B. Waters, C. G. Westmoreland, E. S. Kang, K. Hirao, and M. E. Brito, "Microstructural design of silicon nitride with improved fracture toughness: I, effects of grain shape and size," *Journal of the American Ceramic Society*, vol. 81, pp. 2821–2830, 1998.

[107] S. Kikuchi, Y. Hayami, T. Ishiguri, B. Guennec, A. Ueno, M. Ota, and K. Ameyama, "Effect of bimodal grain size distribution on fatigue properties of ti-6al-4v alloy with harmonic structure under four-point bending," *Materials Science and Engineering: A*, vol. 687, pp. 269–275, 2017.

[108] J. Saini, H. S. Arora, H. S. Grewal, G. Perumal, A. Ayyagari, R. Salloom, and S. Mukherjee, "Excellent corrosion resistance of dualphase bimodal stainless steel. steel research international," vol. 90, no. 18005, p. 54, 2019.

[109] A. Bowyer, "Computing dirichlet tessellations," *The computer journal*, vol. 24, pp. 162–166, 1981.

[110] P. C. Paris, H. Tada, A. Zahoor, and H. Ernst, "The theory of instability of the tearing mode of elastic-plastic crack growth," *Elastic-plastic fracture*, vol. 21, pp. 5–36, 1979.

[111] C. Y. Lee, "An algorithm for path connections and its applications," *IRE transactions on electronic computers*, vol. 3, pp. 346–365, 1961.

[112] E. W. Dijkstra, "A note on two problems in connexion with graphs," *Numerische Mathematik*, vol. 1, pp. 269–271, 1959.

[113] A. P. Jackson, J. F. Vincent, and R. M. Turner, "The mechanical design of nacre. proceedings of the royal society of london," *Series B. Biological sciences*, vol. 234, pp. 415–440, 1988.

[114] P. Fratzl and R. Weinkamer, "Nature's hierarchical materials," *Progress in materials Science*, vol. 52, pp. 1263–1334, 2007.

[115] H. Chai, J. J. W. Lee, P. J. Constantino, P. W. Lucas, and B. R. Lawn, "Remarkable resilience of teeth," *Proceedings of the National Academy of Sciences*, vol. 106, pp. 7289–7293, 2009.

[116] M. E. Launey and R. O. Ritchie, "On the fracture toughness of advanced materials," *Advanced Materials*, vol. 21, pp. 2103–2110, 2009.

APPENDIX A

SUPPLEMENTARY MATERIALS FOR:

IMPORTANCE OF MICROSTRUCTURE IN MATERIAL DESIGN

This appendix includes:

Supplementary Figures A.1 to A.15.

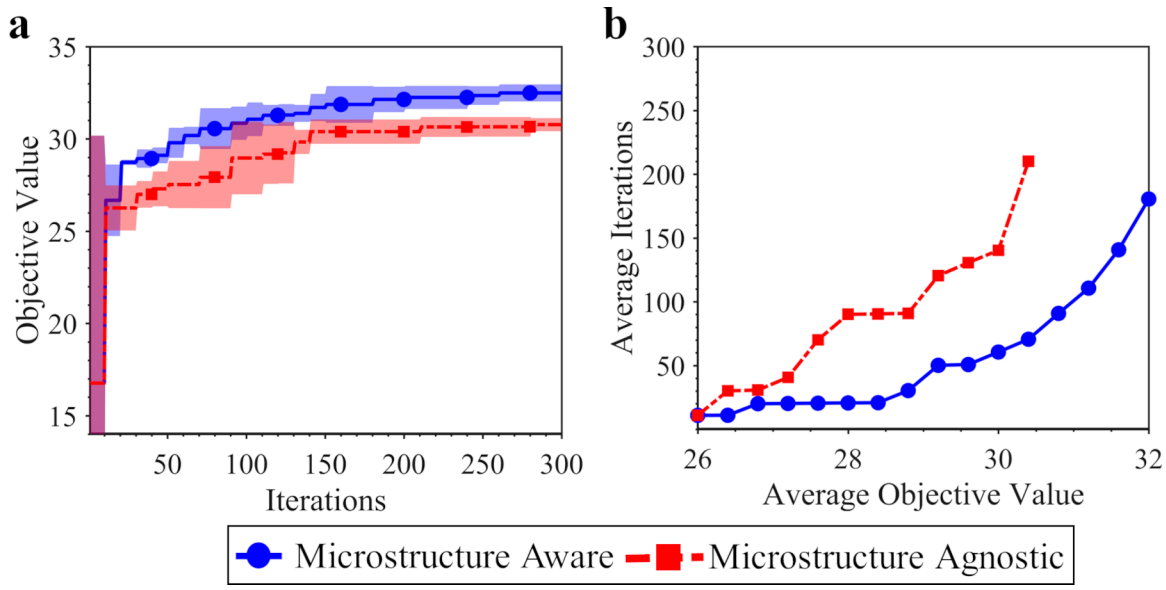

Figure A.1: A comparison of the performance of the traditional *microstructure agnostic* and the novel *microstructure aware* material design approaches when at the beginning of the design process the 'ground truth' information of the input $(\mathbf{X_I})$ - output $(\mathbf{X_O})$ correlation is known at only one set of parameters in the input space. (a) Comparing the maximum objective value found as a function of the number of design iterations for five realizations of the design process. (b) Comparing the average number of design iterations required to reach an average maximum objective value over five realizations of the design process. A realization here refers to different sets of known 'ground truth' $\mathbf{X_I}$ - $\mathbf{X_O}$ correlation at the beginning of the design process.

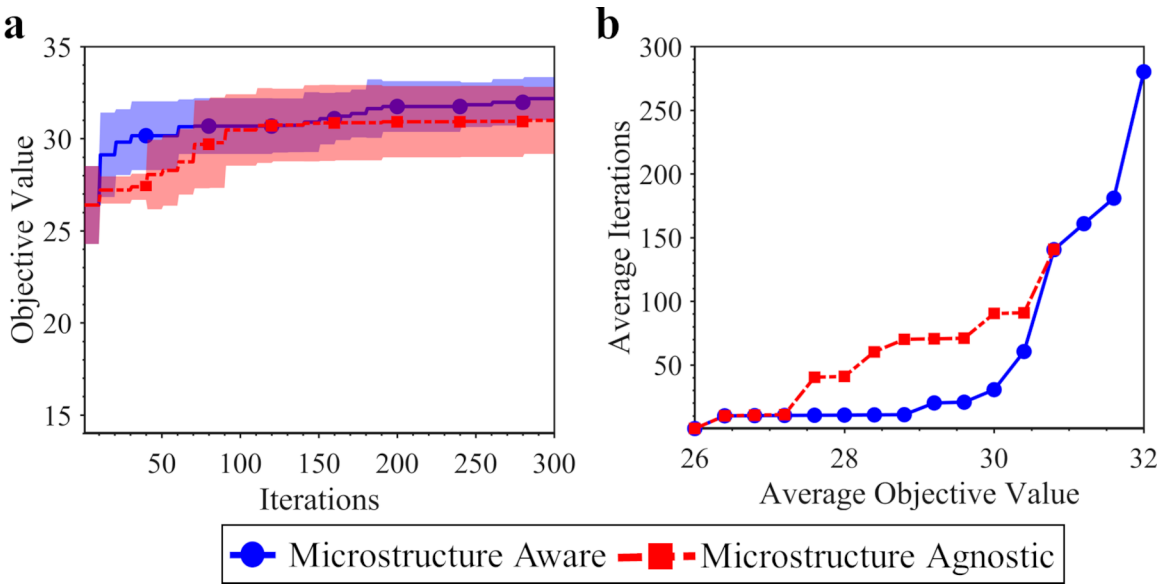

Figure A.2: A comparison of the performance of the traditional *microstructure agnostic* and the novel *microstructure aware* material design approaches when at the beginning of the design process the 'ground truth' information of the input $(\mathbf{X_I})$ - output $(\mathbf{X_O})$ correlation is known at only ten sets of parameters in the input space. (a) Comparing the maximum objective value found as a function of the number of design iterations for five realizations of the design process. (b) Comparing the average number of design iterations required to reach an average maximum objective value over five realizations of the design process. A realization here refers to different sets of known 'ground truth' $\mathbf{X_I}$ - $\mathbf{X_O}$ correlation at the beginning of the design process.

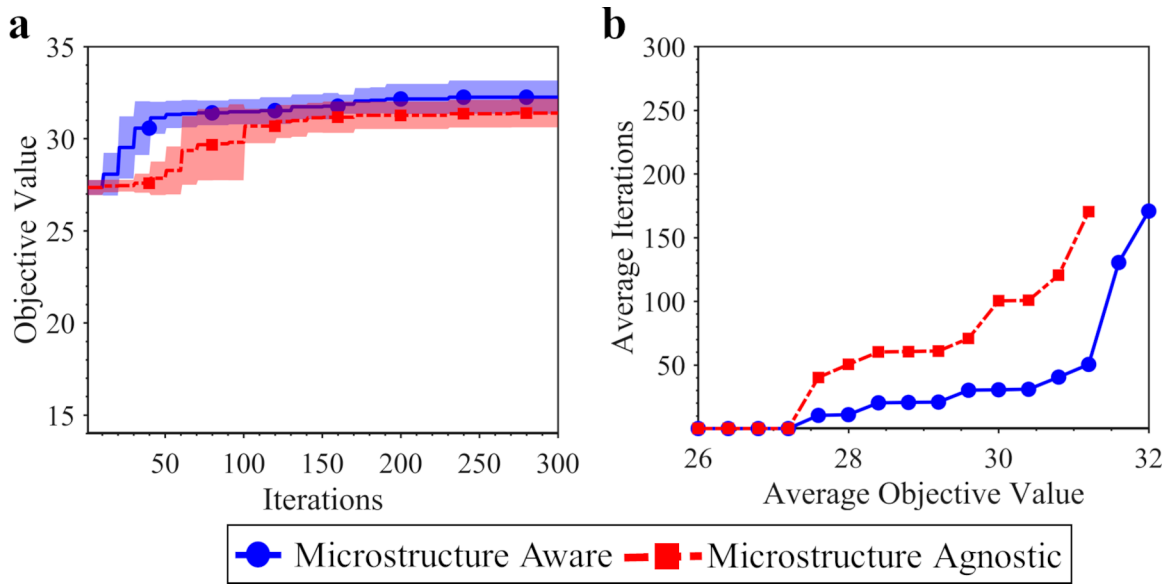

Figure A.3: A comparison of the performance of the traditional *microstructure agnostic* and the novel *microstructure aware* material design approaches when at the beginning of the design process the 'ground truth' information of the input $(\mathbf{X_I})$ - output $(\mathbf{X_O})$ correlation is known at only twenty five sets of parameters in the input space. (a) Comparing the maximum objective value found as a function of the number of design iterations for five realizations of the design process. (b) Comparing the average number of design iterations required to reach an average maximum objective value over five realizations of the design process. A realization here refers to different sets of known 'ground truth' $\mathbf{X_I}$ - $\mathbf{X_O}$ correlation at the beginning of the design process.

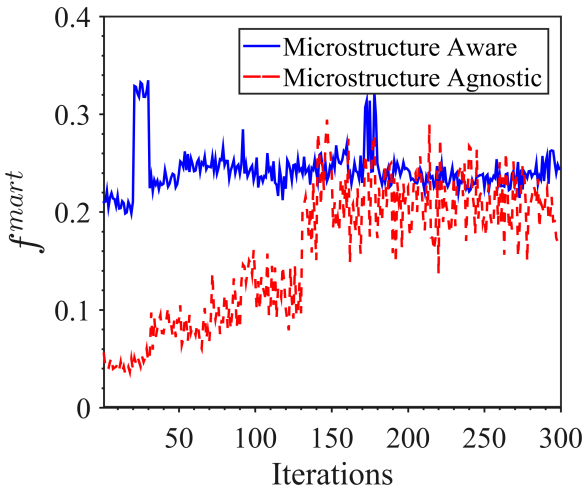

Figure A.4: A comparison of the average value of the optimum microstructure parameter (characterized by the volume fraction of the martensite phase, f^{mart}) identified by the traditional *microstructure agnostic* and the novel *microstructure aware* material design approaches at each design iteration over five realizations of the design process, when at the beginning of the design process the 'ground truth' information of the input $(\mathbf{X_I})$ - output $(\mathbf{X_O})$ correlation is known at only one set of parameters in the input space. A realization here refers to different sets of known 'ground truth' $\mathbf{X_I}$ - $\mathbf{X_O}$ correlation at the beginning of the design process.

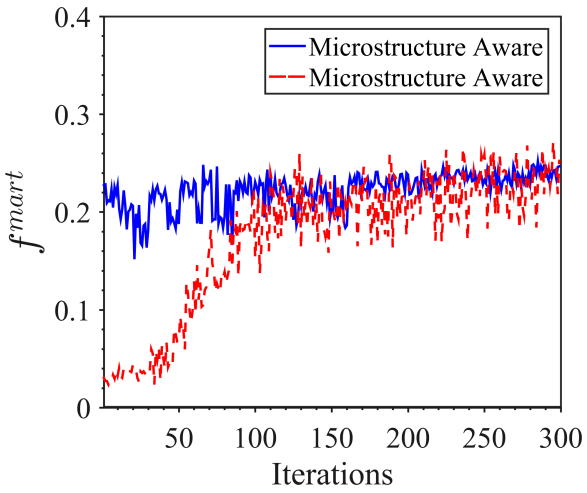

Figure A.5: A comparison of the average value of the optimum microstructure parameter (characterized by the volume fraction of the martensite phase, f^{mart}) identified by the traditional *microstructure agnostic* and the novel *microstructure aware* material design approaches at each design iteration over five realizations of the design process, when at the beginning of the design process the 'ground truth' information of the input $(\mathbf{X_I})$ - output $(\mathbf{X_O})$ correlation is known at only ten sets of parameters in the input space. A realization here refers to different sets of known 'ground truth' $\mathbf{X_I}$ - $\mathbf{X_O}$ correlation at the beginning of the design process.

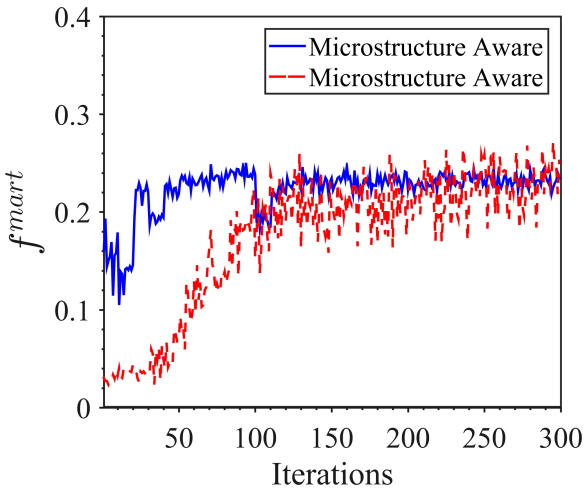

Figure A.6: A comparison of the average value of the optimum microstructure parameter (characterized by the volume fraction of the martensite phase, f^{mart}) identified by the traditional *microstructure agnostic* and the novel *microstructure aware* material design approaches at each design iteration over five realizations of the design process, when at the beginning of the design process the 'ground truth' information of the input $(\mathbf{X_I})$ - output $(\mathbf{X_O})$ correlation is known at only twenty five sets of parameters in the input space. A realization here refers to different sets of known 'ground truth' $\mathbf{X_I}$ - $\mathbf{X_O}$ correlation at the beginning of the design process.

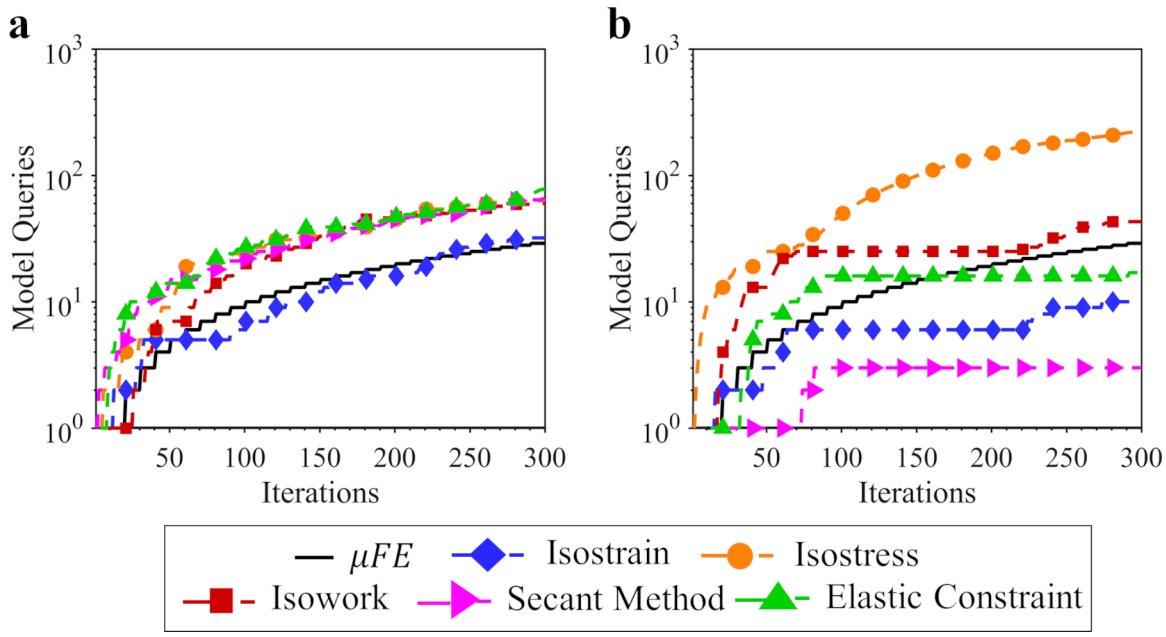

Figure A.7: Exploitation of information sources (Isostrain, Isostress, Isowork, Secant Method and Elastic Constraint reduced-order models) and the 'ground truth' (μFE) model at each design iteration by the (a) novel *microstructure aware* and the (b) traditional *microstructure agnostic* material design approaches when at the beginning of the design process the 'ground truth' information of the input $(\mathbf{X_I})$ - output $(\mathbf{X_O})$ correlation is known at only one set of parameters in the input space. The results are shown for one realization of the design process.

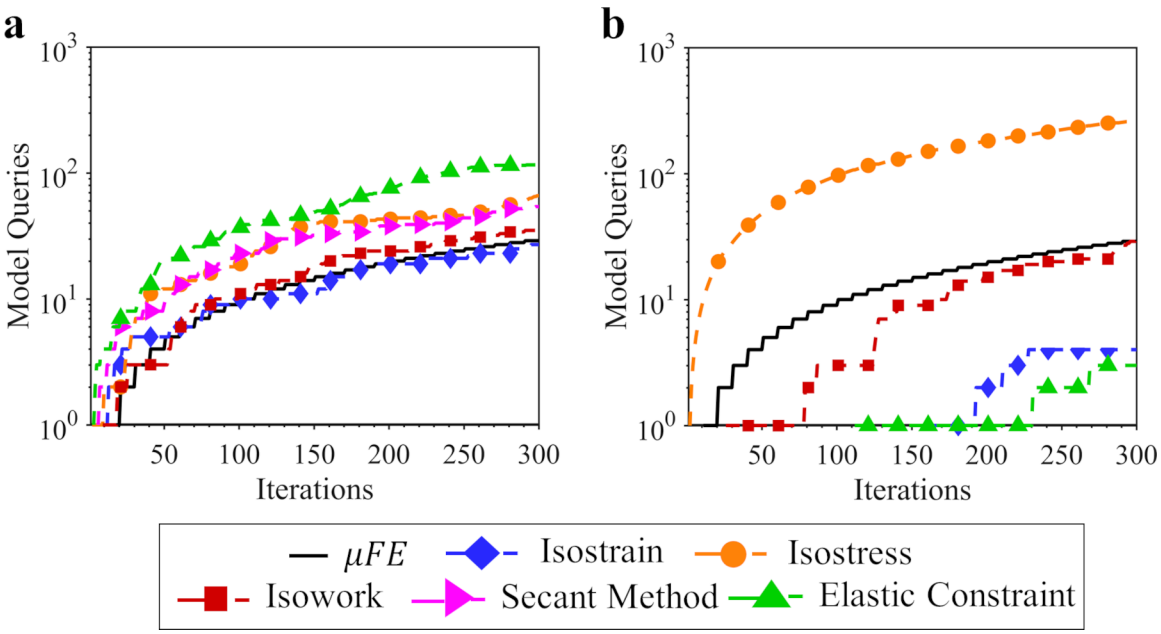

Figure A.8: Exploitation of information sources (Isostrain, Isostress, Isowork, Secant Method and Elastic Constraint reduced-order models) and the 'ground truth' (μFE) model at each design iteration by the (a) novel *microstructure aware* and the (b) traditional *microstructure agnostic* material design approaches when at the beginning of the design process the 'ground truth' information of the input $(\mathbf{X_I})$ - output $(\mathbf{X_O})$ correlation is known at only ten sets of parameters in the input space. The results are shown for one realization of the design process.

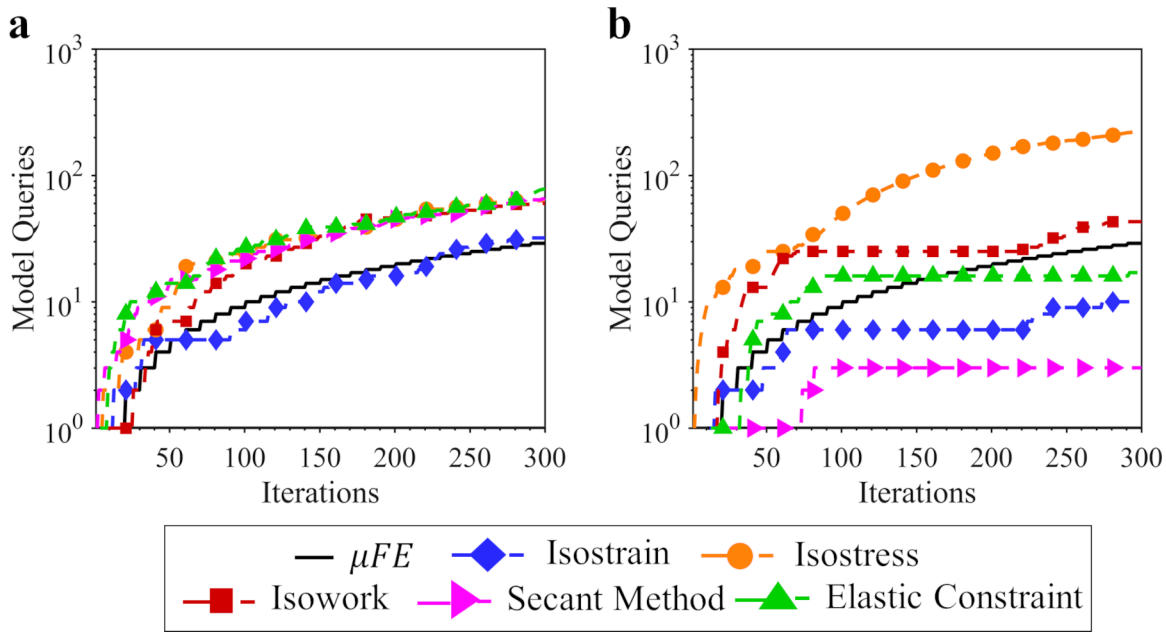

Figure A.9: Exploitation of information sources (Isostrain, Isostress, Isowork, Secant Method and Elastic Constraint reduced-order models) and the 'ground truth' (μFE) model at each design iteration by the (a) novel *microstructure aware* and the (b) traditional *microstructure agnostic* material design approaches when at the beginning of the design process the 'ground truth' information of the input $(\mathbf{X_I})$ - output $(\mathbf{X_O})$ correlation is known at only twenty five sets of parameters in the input space. The results are shown for one realization of the design process.

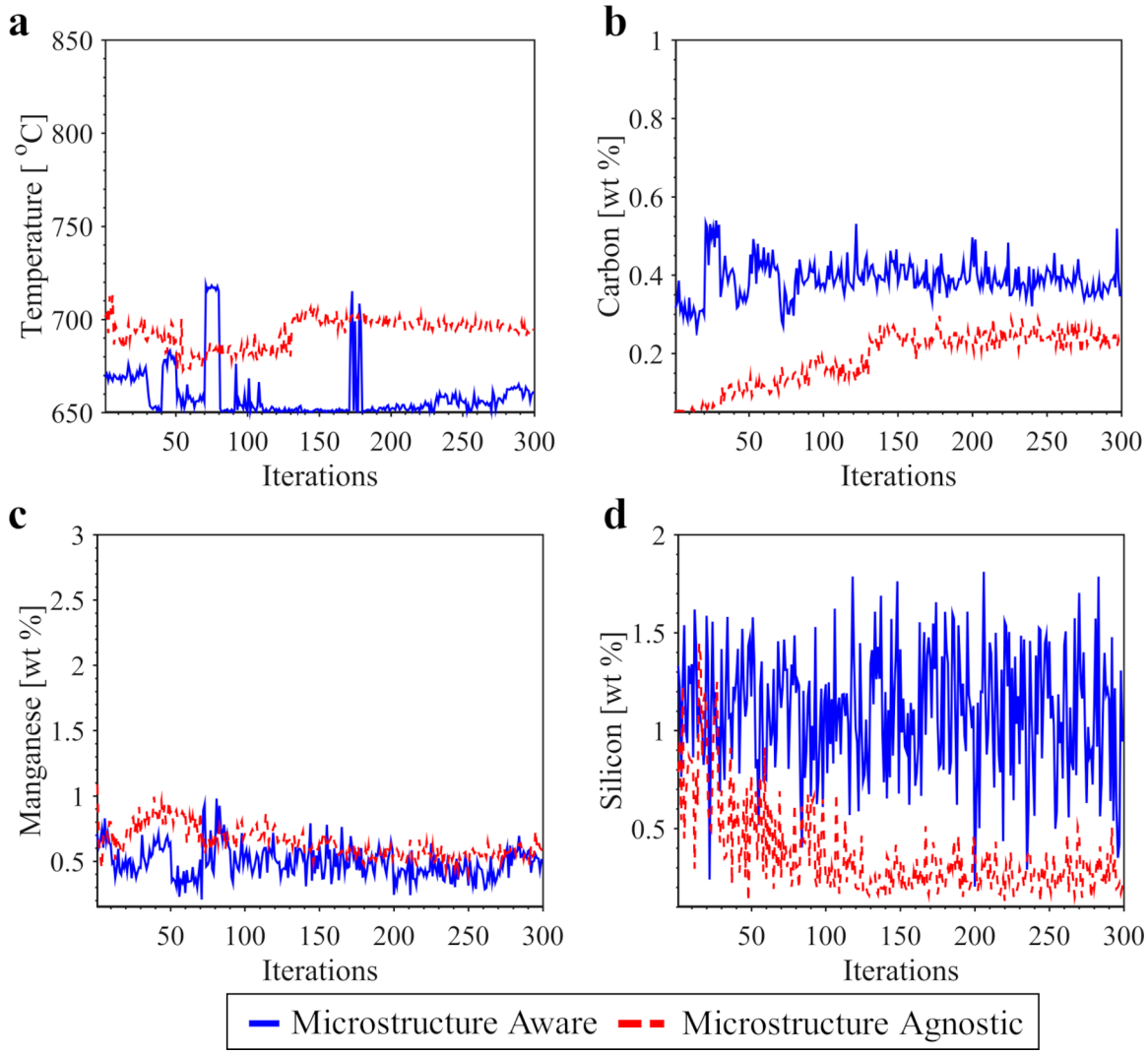

Figure A.10: A comparison of the optimum processing/chemistry parameters identified by the traditional *microstructure agnostic* and the novel *microstructure aware* material design approaches when at the beginning of the design process the 'ground truth' information of the input $(\mathbf{X_I})$ - output $(\mathbf{X_O})$ correlation is known at only one set of parameters in the input space. (a)-(d) Comparing the average optimal values of the processing parameter, intercritical annealing temperature, and the amount of alloying elements, Carbon, Manganese and Silicon that correspond to the average maximum objective value at each design iteration over five realizations of the design process. A realization here refers to different sets of known 'ground truth' $\mathbf{X_I}$ - $\mathbf{X_O}$ correlation at the beginning of the design process.

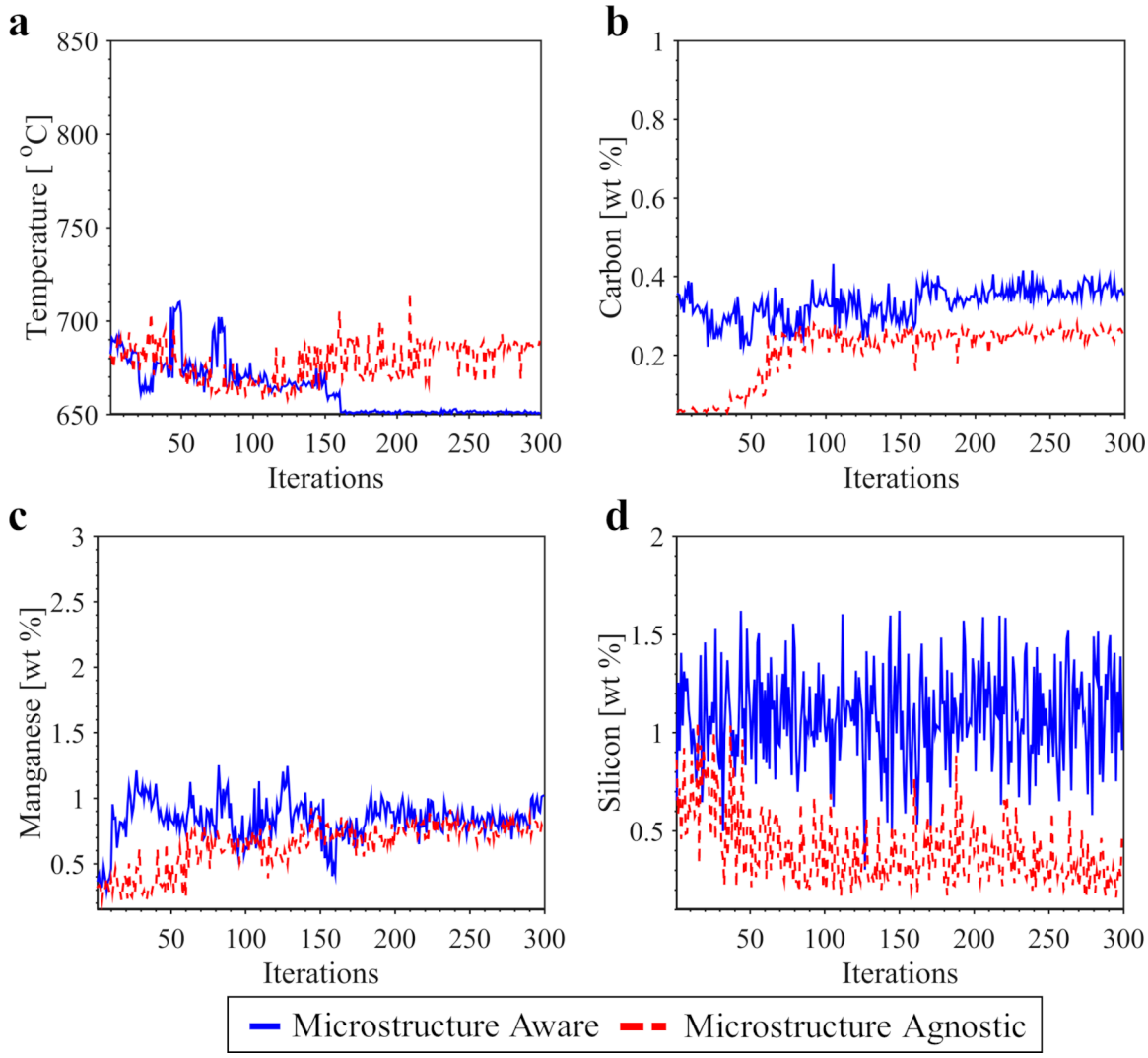

Figure A.11: A comparison of the optimum processing/chemistry parameters identified by the traditional *microstructure agnostic* and the novel *microstructure aware* material design approaches when at the beginning of the design process the 'ground truth' information of the input $(\mathbf{X_I})$ - output $(\mathbf{X_O})$ correlation is known at only ten sets of parameters in the input space. (a)-(d) Comparing the average optimal values of the processing parameter, intercritical annealing temperature, and the amount of alloying elements, Carbon, Manganese and Silicon that correspond to the average maximum objective value at each design iteration over five realizations of the design process. A realization here refers to different sets of known 'ground truth' $\mathbf{X_I}$ - $\mathbf{X_O}$ correlation at the beginning of the design process.

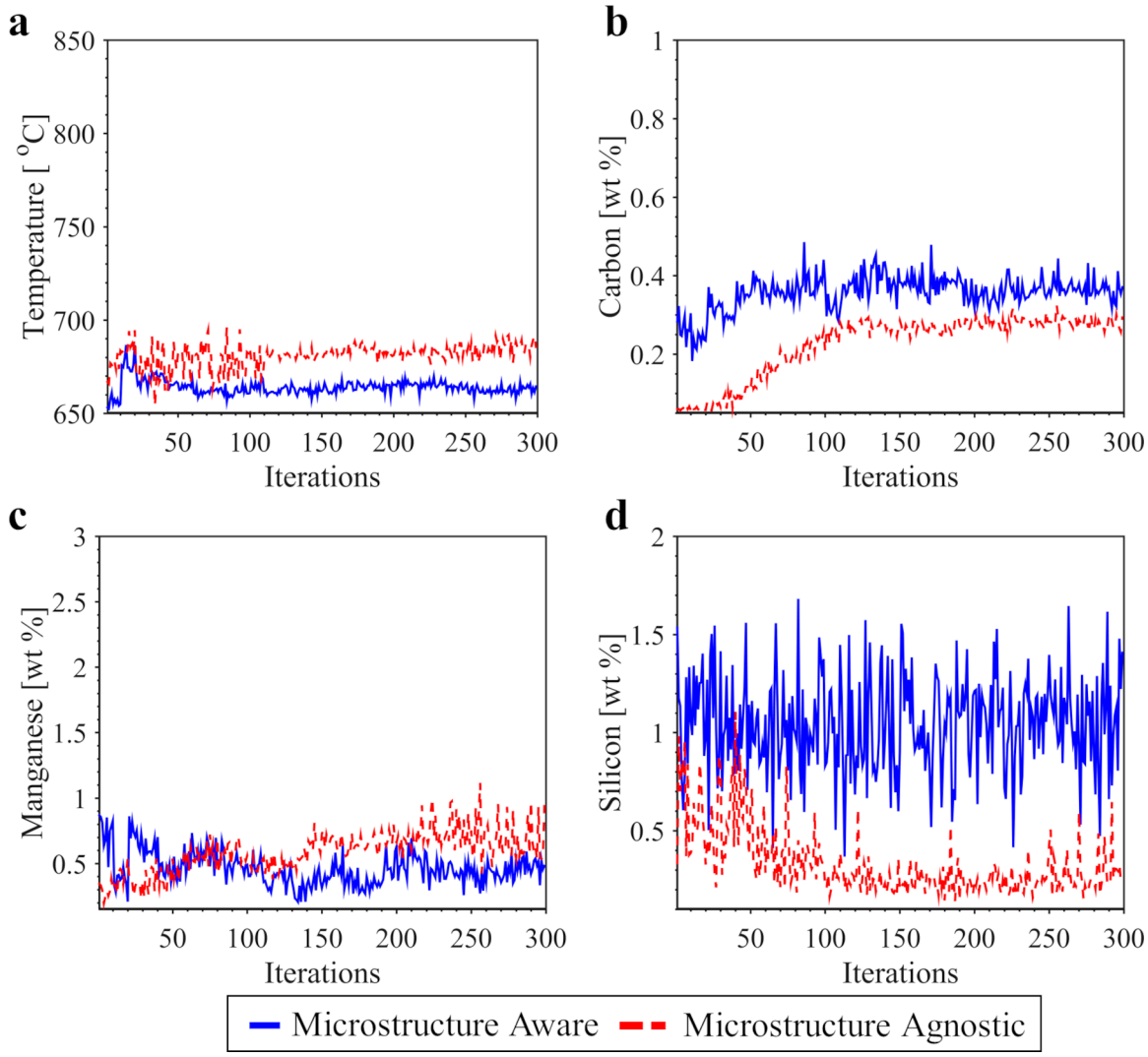

Figure A.12: A comparison of the optimum processing/chemistry parameters identified by the traditional *microstructure agnostic* and the novel *microstructure aware* material design approaches when at the beginning of the design process the 'ground truth' information of the input $(\mathbf{X_I})$ - output $(\mathbf{X_O})$ correlation is known at only twenty five sets of parameters in the input space. (a)-(d) Comparing the average optimal values of the processing parameter, intercritical annealing temperature, and the amount of alloying elements, Carbon, Manganese and Silicon that correspond to the average maximum objective value at each design iteration over five realizations of the design process. A realization here refers to different sets of known 'ground truth' $\mathbf{X_I}$ - $\mathbf{X_O}$ correlation at the beginning of the design process.

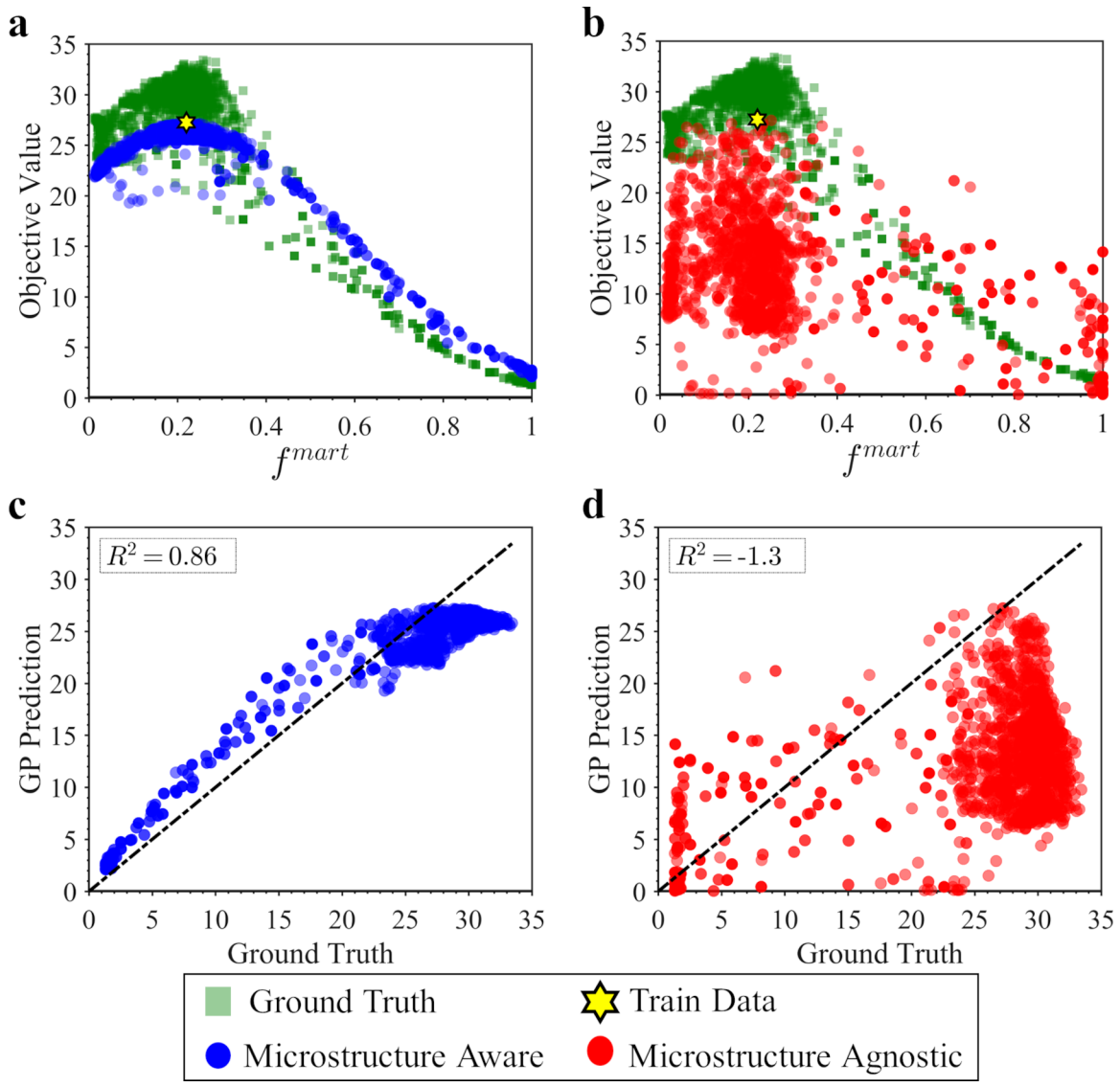

Figure A.13: A comparison of the predicted variation of the objective value as a function of the material microstructure characterized by the volume fraction of the martensite phase, f^{mart}, obtained from exhaustively querying the 'ground truth' information source (μFE) and the initial (at the very first design iteration) fused Gaussian Process model built using only one initial 'ground truth' information (marked as star) following the (a) *microstructure aware* and (b) *microstructure agnostic* approaches. Parity plots of the objective value obtained from exhaustively querying the 'ground truth' information source and the fused Gaussian Process model following the (c) *microstructure aware* and (d) *microstructure agnostic* approaches. The results are shown for one realization of the design process.

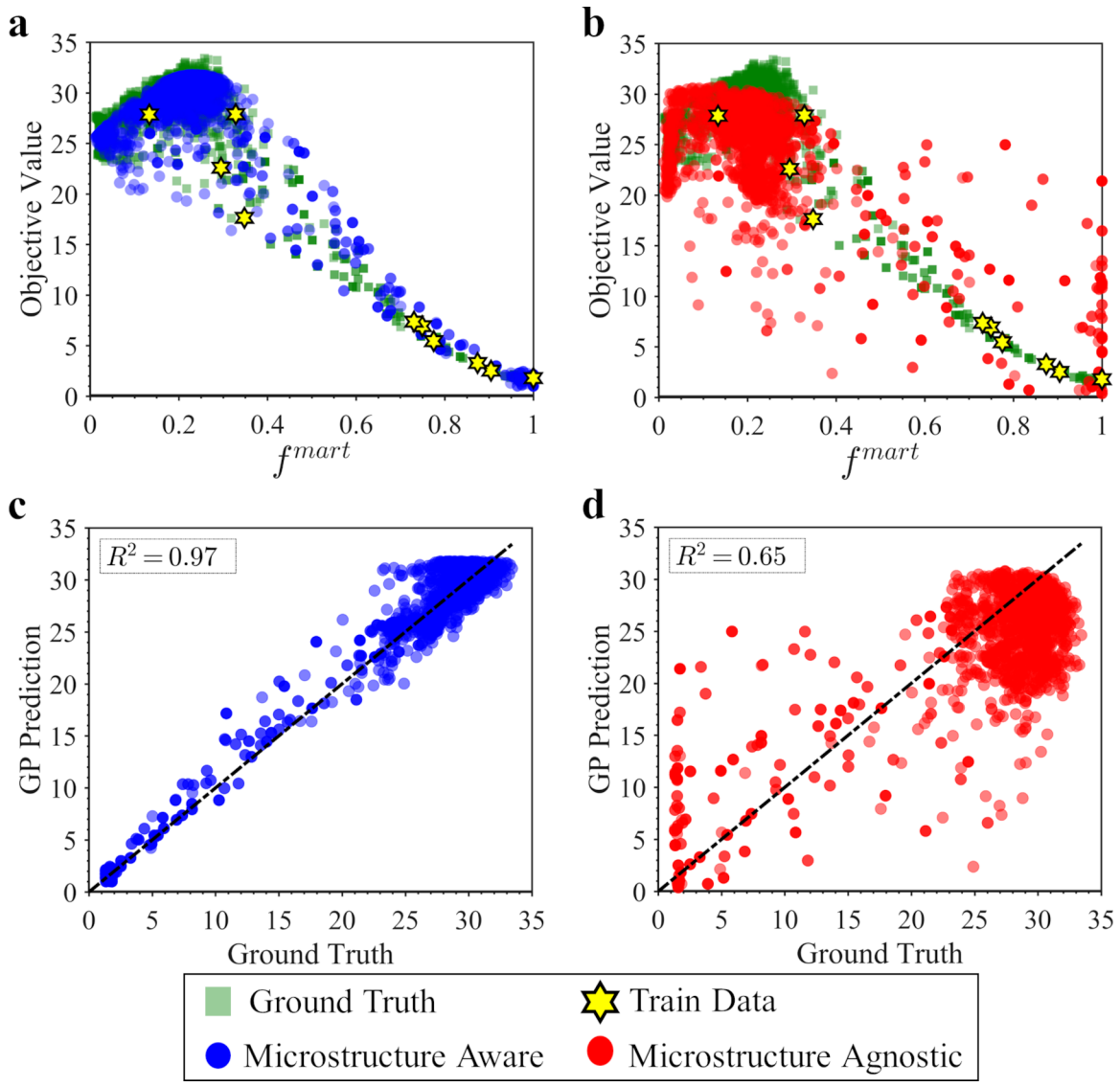

Figure A.14: A comparison of the predicted variation of the objective value as a function of the material microstructure characterized by the volume fraction of the martensite phase, f^{mart}, obtained from exhaustively querying the 'ground truth' information source (μFE) and the initial (at the very first design iteration) fused Gaussian Process model built using only ten initial 'ground truth' information (marked as star) following the (a) *microstructure aware* and (b) *microstructure agnostic* approaches. Parity plots of the objective value obtained from exhaustively querying the 'ground truth' information source and the fused Gaussian Process model following the (c) *microstructure aware* and (d) *microstructure agnostic* approaches. The results are shown for one realization of the design process.

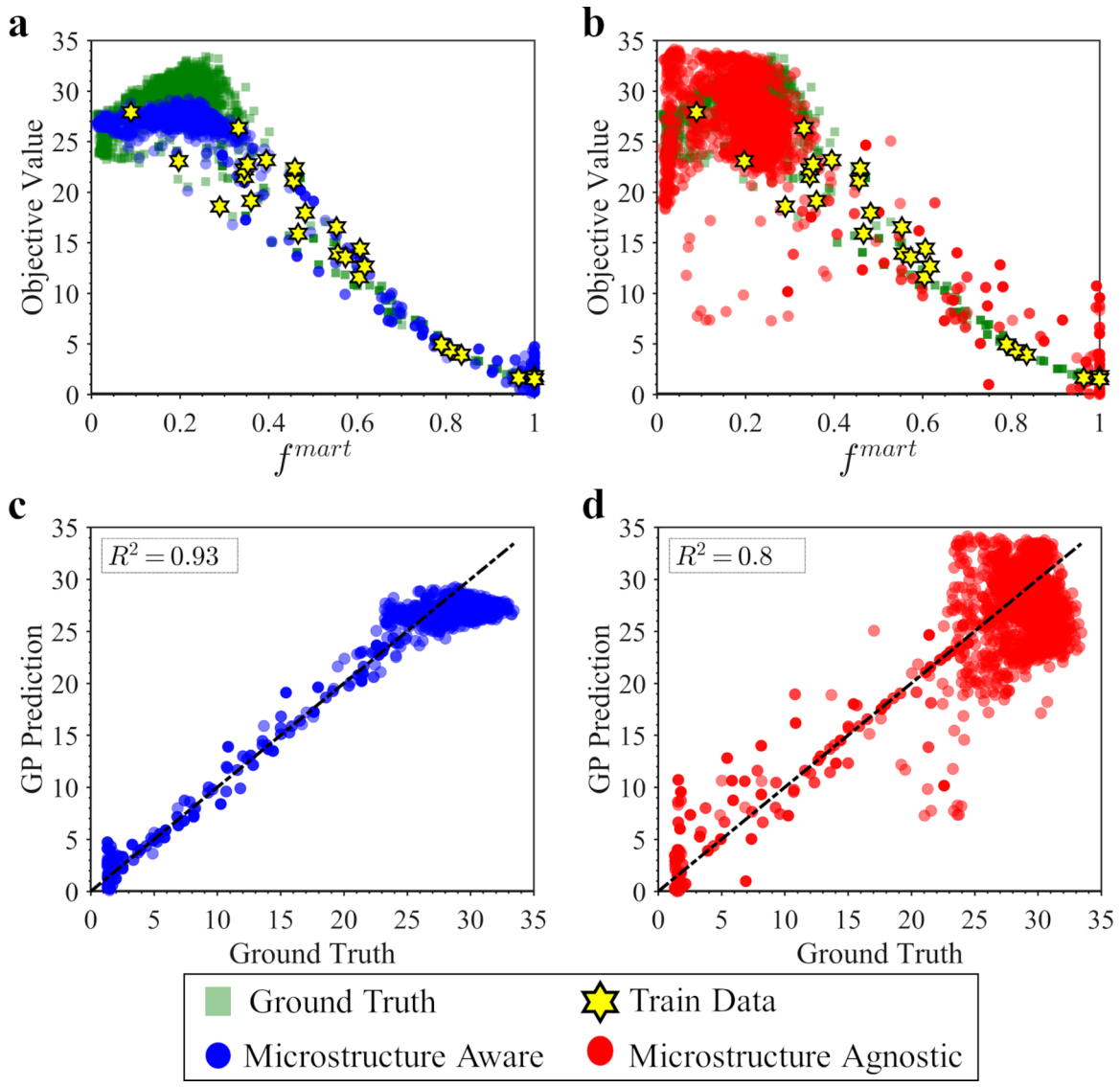

Figure A.15: A comparison of the predicted variation of the objective value as a function of the material microstructure characterized by the volume fraction of the martensite phase, f^{mart}, obtained from exhaustively querying the 'ground truth' information source (μFE) and the initial (at the very first design iteration) fused Gaussian Process model built using only twenty five initial 'ground truth' information (marked as star) following the (a) *microstructure aware* and (b) *microstructure agnostic* approaches. Parity plots of the objective value obtained from exhaustively querying the 'ground truth' information source and the fused Gaussian Process model following the (c) *microstructure aware* and (d) *microstructure agnostic* approaches. The results are shown for one realization of the design process.

APPENDIX B

SUPPLEMENTARY MATERIALS FOR:

DUCTILE FRACTURE PREDICTION USING EVOLVING GRAPHS

This appendix includes:

Supplementary Figures B.1 to B.20.

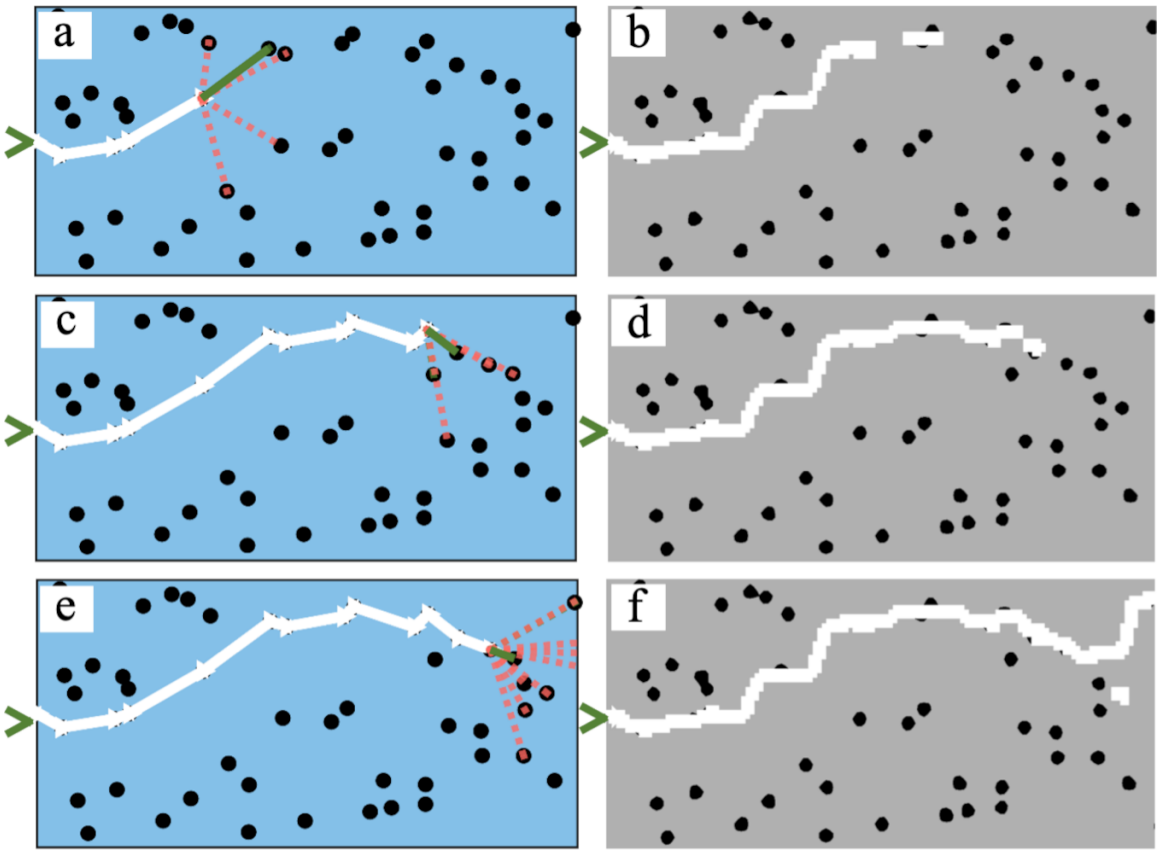

Figure B.1: Comparisons of crack path predicted using evolving graph method and microstructure-based finite element model for disconnected microstructural network constituting of distribution of discrete inclusions with mean inclusion spacing, , $l_{incl} = 6\delta$ shown at three different time steps. (a) construction of a local graph at a inclusion by building the edges (possible crack paths) that connect to this particular inclusion and then the selection of a crack path with least crack growth resistance, ΔJ. Possible crack paths are highlighted as red dashed lines and the selected crack path is shown in solid green line. The solid white line shows the propagation of crack till this inclusion. (b) shows the path predicted using the finite element calculation for the particular time step. (c) shows the another instance of construction of a local graph at this inclusion and then selection of the path with minimum ΔJ. (d) shows the path predicted from finite element calculations for the particular time step. Similarly (e) and (f) show path predicted from graph model and finite element calculations as the crack reaches the end of the microstructure. Here the propagation of crack occurs through collection of predictions of paths from the local graphs built at the inclusions.

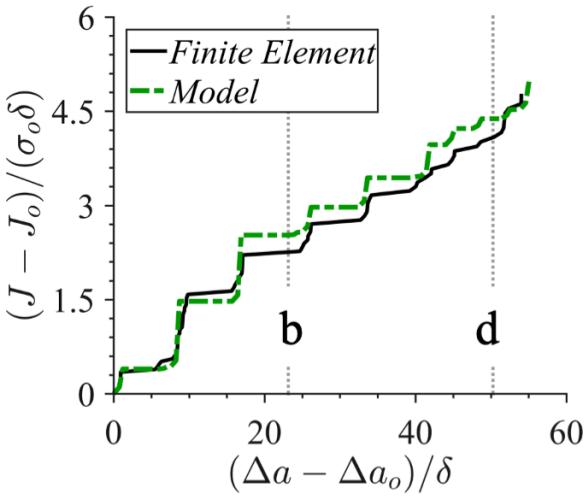

Figure B.2: Comparisons of crack growth resistance curves predicted using evolving graph method and microstructure-based finite element model for disconnected microstructural network with a distribution of discrete inclusions with mean inclusion spacing, $l_{incl} = 6\delta$ shown in Figure B.1 . Comparison of curves of normalized J, $(J - J_0)/(\sigma_0 \delta)$, versus normalized crack extension $(\Delta a - \Delta a_0)/\delta$ computed from finite element calculations (solid line) and evolving graph method (dashed green line). The dotted grey lines, b and d correspond to the locations of propagation of crack in Figure B.1(b) and Figure B.1(d).

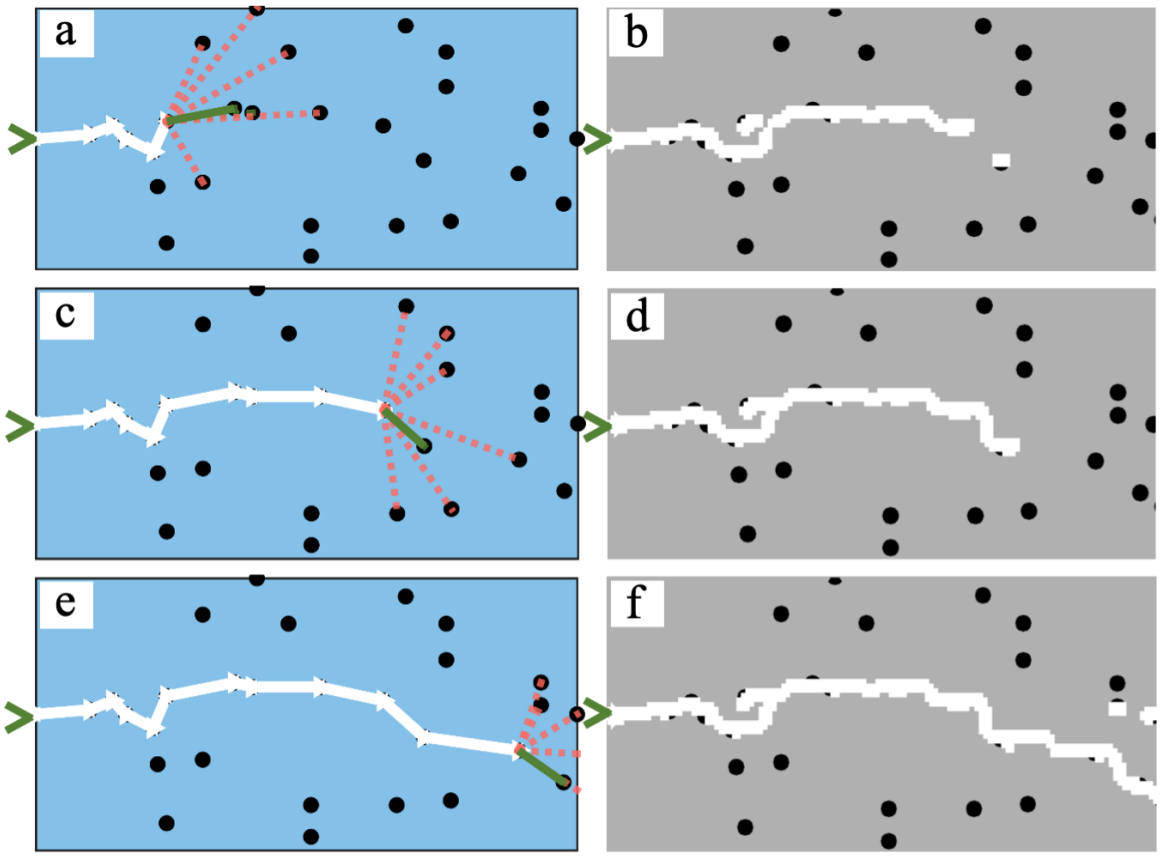

Figure B.3: Comparisons of crack path predicted using evolving graph method and microstructure-based finite element model for disconnected microstructural network constituting of distribution of discrete inclusions with mean inclusion spacing, , $l_{incl} = 8\delta$ shown at three different time steps. (a) construction of a local graph at a inclusion by building the edges (possible crack paths) that connect to this particular inclusion and then the selection of a crack path with least crack growth resistance, ΔJ. Possible crack paths are highlighted as red dashed lines and the selected crack path is shown in solid green line. The solid white line shows the propagation of crack till this inclusion. (b) shows the path predicted using the finite element calculation for the particular time step. (c) shows the another instance of construction of a local graph at this inclusion and then selection of the path with minimum ΔJ. (d) shows the path predicted from finite element calculations for the particular time step. Similarly (e) and (f) show path predicted from graph model and finite element calculations as the crack reaches the end of the microstructure. Here the propagation of crack occurs through collection of predictions of paths from the local graphs built at the inclusions.

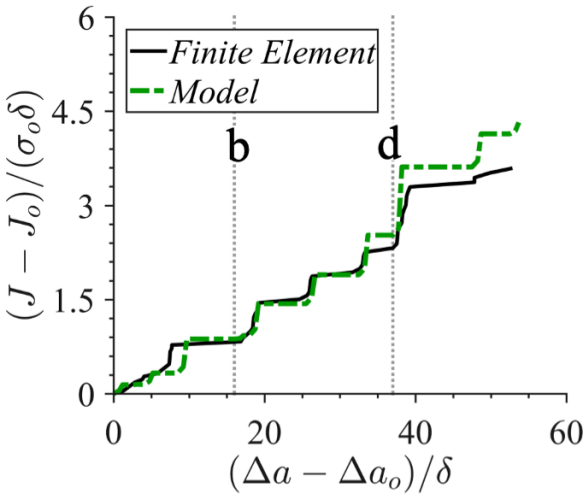

Figure B.4: Comparisons of crack growth resistance curves predicted using evolving graph method and microstructure-based finite element model for disconnected microstructural network with a distribution of discrete inclusions with mean inclusion spacing, $l_{incl} = 8\delta$ shown in Figure B.3 . Comparison of curves of normalized $J, (J - J_0)/(\sigma_0 \delta)$, versus normalized crack extension $(\Delta a - \Delta a_0)/\delta$ computed from finite element calculations (solid line) and evolving graph method (dashed green line). The dotted grey lines, b and d correspond to the locations of propagation of crack in Figure B.3(b) and Figure B.3(d).

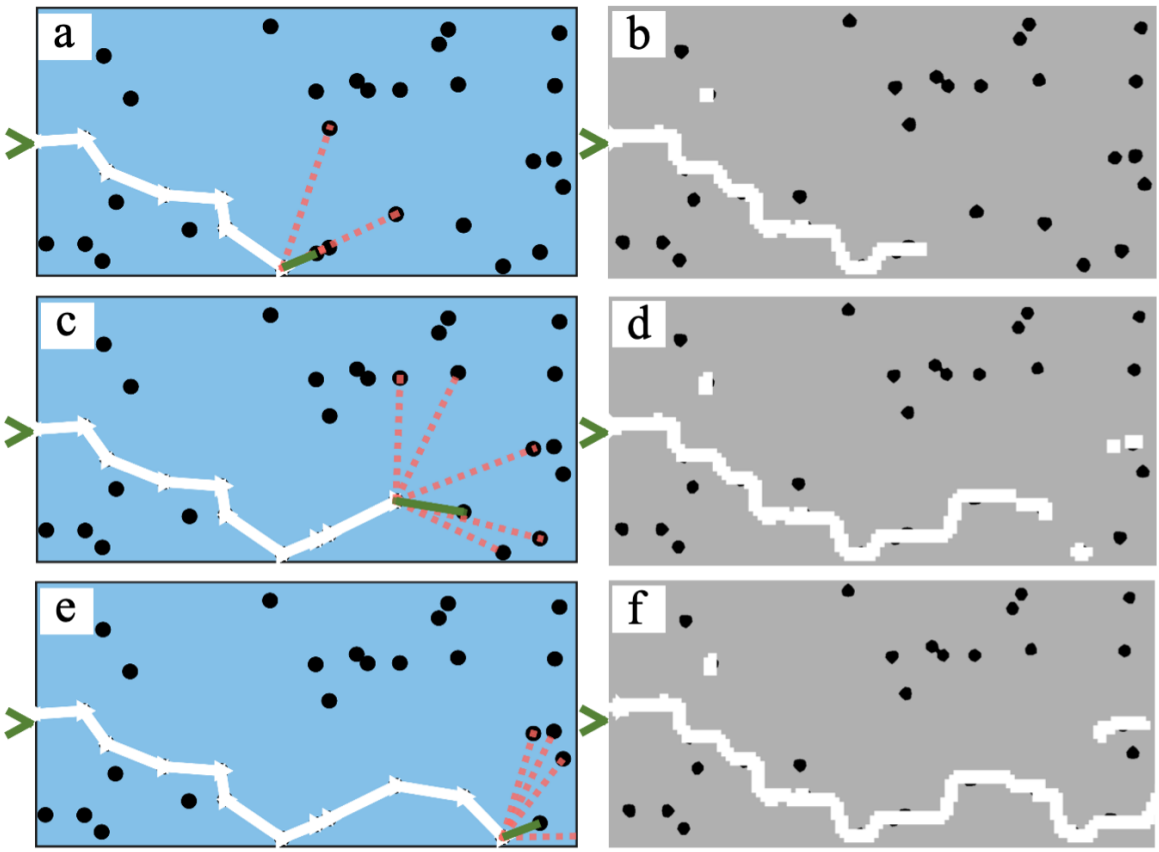

Figure B.5: Comparisons of crack path predicted using evolving graph method and microstructure-based finite element model for disconnected microstructural network constituting of distribution of discrete inclusions with mean inclusion spacing, , $l_{incl} = 8\delta$ shown at three different time steps. (a) construction of a local graph at a inclusion by building the edges (possible crack paths) that connect to this particular inclusion and then the selection of a crack path with least crack growth resistance, ΔJ. Possible crack paths are highlighted as red dashed lines and the selected crack path is shown in solid green line. The solid white line shows the propagation of crack till this inclusion. (b) shows the path predicted using the finite element calculation for the particular time step. (c) shows the another instance of construction of a local graph at this inclusion and then selection of the path with minimum ΔJ. (d) shows the path predicted from finite element calculations for the particular time step. Similarly (e) and (f) show path predicted from graph model and finite element calculations as the crack reaches the end of the microstructure. Here the propagation of crack occurs through collection of predictions of paths from the local graphs built at the inclusions.

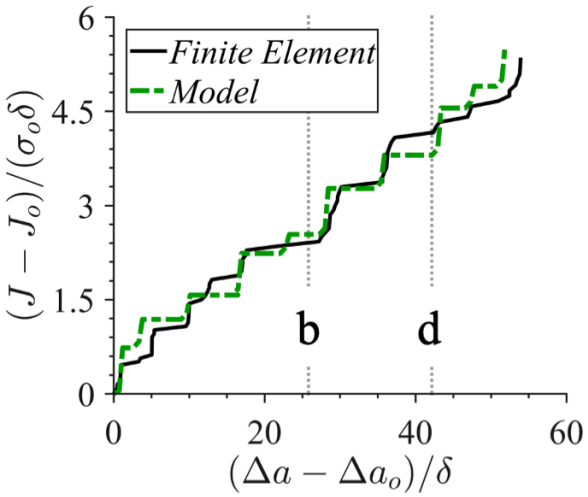

Figure B.6: Comparisons of crack growth resistance curves predicted using evolving graph method and microstructure-based finite element model for disconnected microstructural network with a distribution of discrete inclusions with mean inclusion spacing, $l_{incl} = 8\delta$ shown in Figure B.5 . Comparison of curves of normalized $J, (J - J_0)/(\sigma_0 \delta)$, versus normalized crack extension $(\Delta a - \Delta a_0)/\delta$ computed from finite element calculations (solid line) and evolving graph method (dashed green line). The dotted grey lines, b and d correspond to the locations of propagation of crack in Figure B.5(b) and Figure B.5(d).

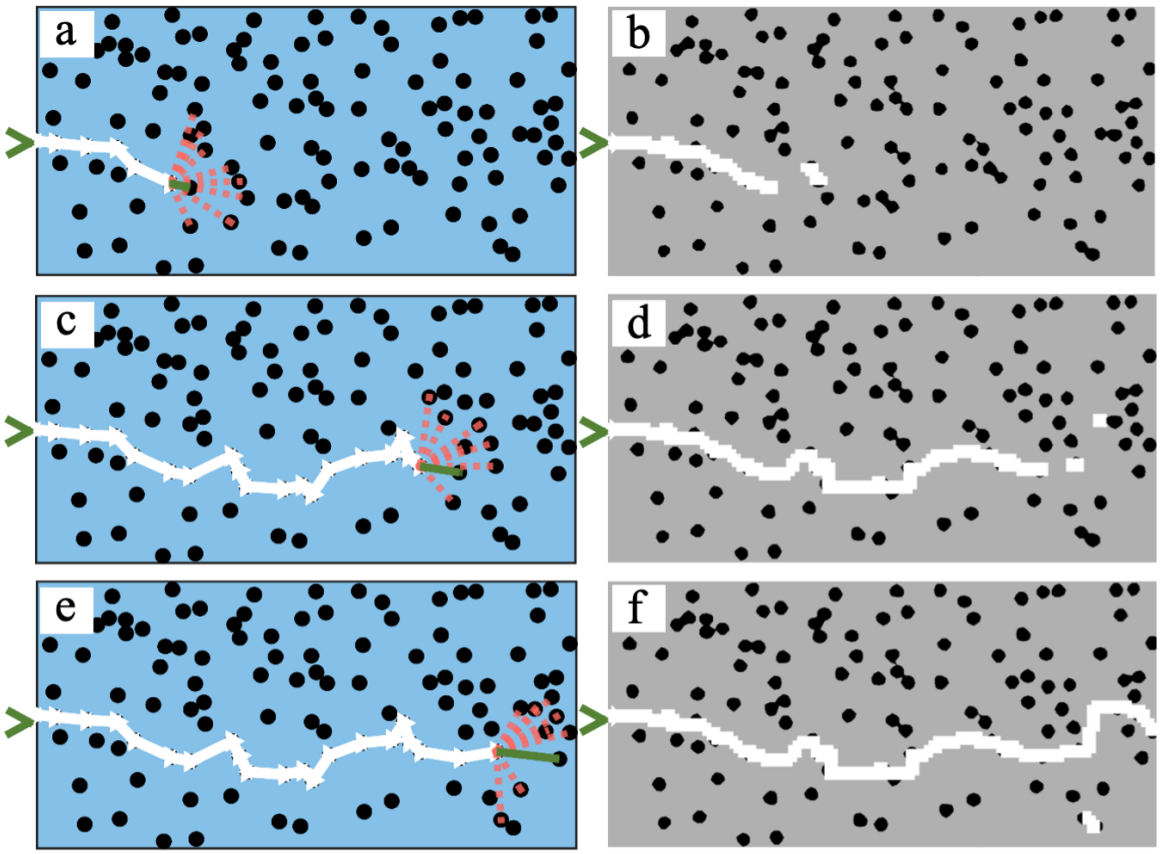

Figure B.7: Comparisons of crack path predicted using evolving graph method and microstructure-based finite element model for disconnected microstructural network constituting of distribution of discrete inclusions with mean inclusion spacing, , $l_{incl} = 4\delta$ shown at three different time steps. (a) construction of a local graph at a inclusion by building the edges (possible crack paths) that connect to this particular inclusion and then the selection of a crack path with least crack growth resistance, ΔJ. Possible crack paths are highlighted as red dashed lines and the selected crack path is shown in solid green line. The solid white line shows the propagation of crack till this inclusion. (b) shows the path predicted using the finite element calculation for the particular time step. (c) shows the another instance of construction of a local graph at this inclusion and then selection of the path with minimum ΔJ. (d) shows the path predicted from finite element calculations for the particular time step. Similarly (e) and (f) show path predicted from graph model and finite element calculations as the crack reaches the end of the microstructure. Here the propagation of crack occurs through collection of predictions of paths from the local graphs built at the inclusions.

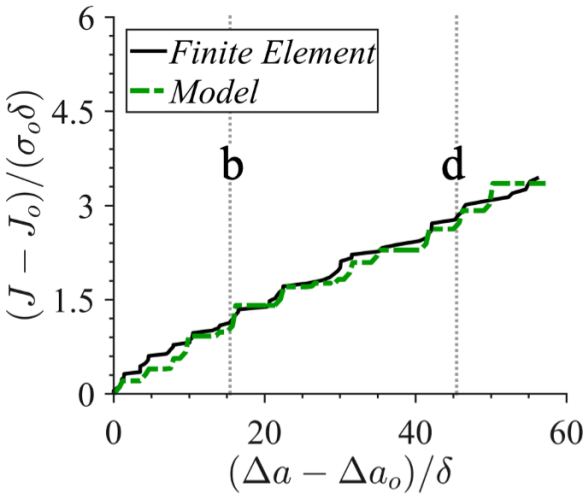

Figure B.8: Comparisons of crack growth resistance curves predicted using evolving graph method and microstructure-based finite element model for disconnected microstructural network with a distribution of discrete inclusions with mean inclusion spacing, $l_{incl} = 4\delta$ shown in Figure B.7 . Comparison of curves of normalized $J, (J - J_0)/(\sigma_0 \delta)$, versus normalized crack extension $(\Delta a - \Delta a_0)/\delta$ computed from finite element calculations (solid line) and evolving graph method (dashed green line). The dotted grey lines, b and d correspond to the locations of propagation of crack in Figure B.7(b) and Figure B.7(d).

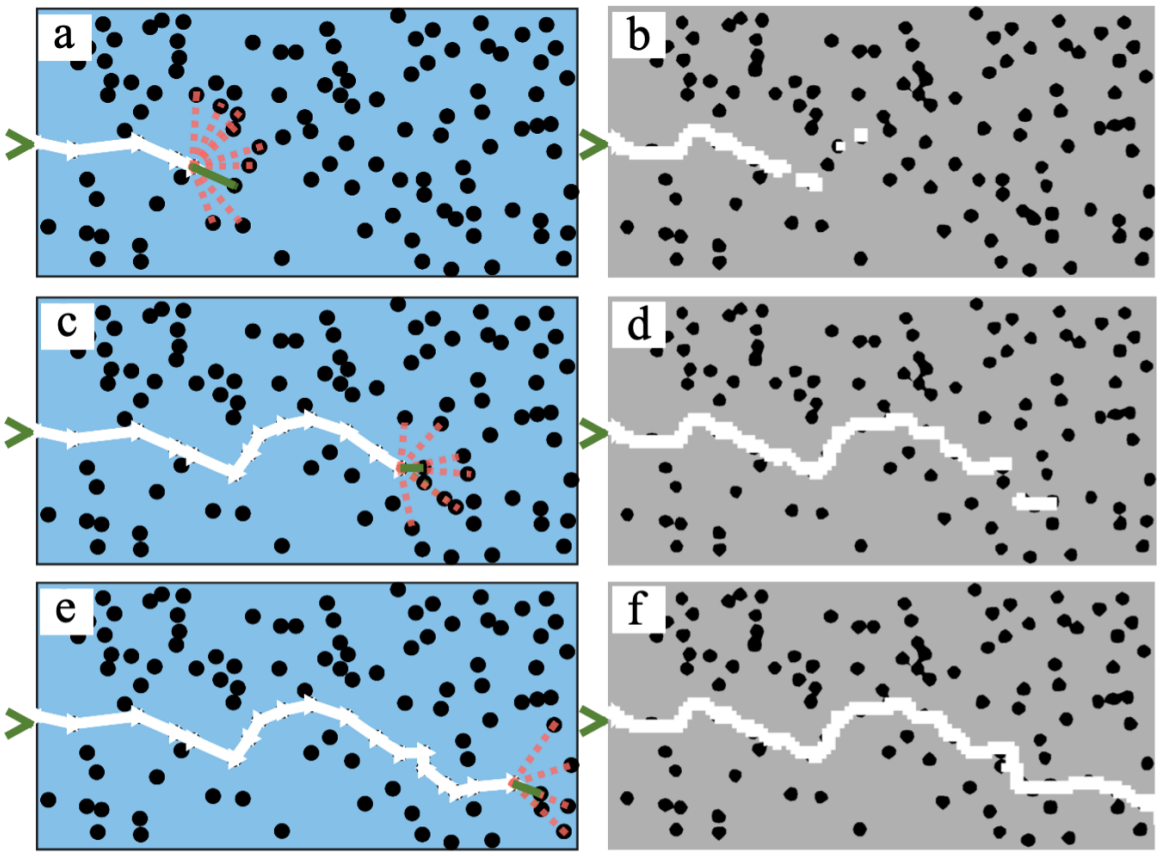

Figure B.9: Comparisons of crack path predicted using evolving graph method and microstructure-based finite element model for disconnected microstructural network constituting of distribution of discrete inclusions with mean inclusion spacing, , $l_{incl} = 4\delta$ shown at three different time steps. (a) construction of a local graph at a inclusion by building the edges (possible crack paths) that connect to this particular inclusion and then the selection of a crack path with least crack growth resistance, ΔJ. Possible crack paths are highlighted as red dashed lines and the selected crack path is shown in solid green line. The solid white line shows the propagation of crack till this inclusion. (b) shows the path predicted using the finite element calculation for the particular time step. (c) shows the another instance of construction of a local graph at this inclusion and then selection of the path with minimum ΔJ. (d) shows the path predicted from finite element calculations for the particular time step. Similarly (e) and (f) show path predicted from graph model and finite element calculations as the crack reaches the end of the microstructure. Here the propagation of crack occurs through collection of predictions of paths from the local graphs built at the inclusions.

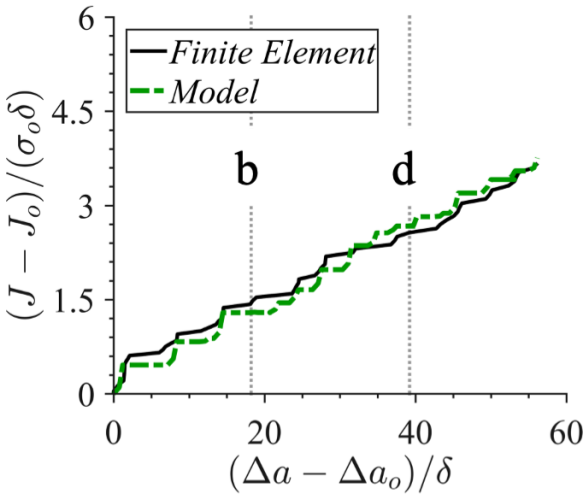

Figure B.10: Comparisons of crack growth resistance curves predicted using evolving graph method and microstructure-based finite element model for disconnected microstructural network with a distribution of discrete inclusions with mean inclusion spacing, $l_{incl} = 4\delta$ shown in Figure B.9 . Comparison of curves of normalized J, $(J-J_0)/(\sigma_0\delta)$, versus normalized crack extension $(\Delta a - \Delta a_0)/\delta$ computed from finite element calculations (solid line) and evolving graph method (dashed green line). The dotted grey lines, b and d correspond to the locations of propagation of crack in Figure B.9(b) and Figure B.9(d).

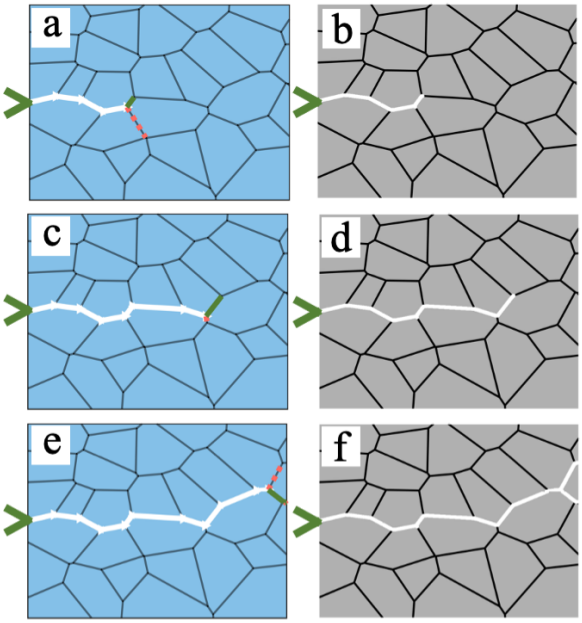

Figure B.11: Comparisons of crack path predicted using evolving graph method and microstructure-based finite element model for connected microstructural network with average grain size, $d_g = 5\delta$ shown at three different time steps. (a) construction of a local graph at the grain boundary junction from the network of grain boundaries at this particular junction and then the selection of a crack path with least crack growth resistance, ΔJ. Possible crack paths are highlighted as red dashed lines and the selected crack path is shown in solid green line. The solid white line shows the propagation of crack till this grain boundary junction where the local graph is built. (b) shows the path predicted using the finite element calculation for the particular time step in (a). (c) shows the another instance of construction of a local graph at this inclusion and then selection of the path with minimum ΔJ. (d) shows the path predicted from finite element calculations for the particular time step in (c). Similarly (e) and (f) show path predicted from graph model and finite element calculations as the crack reaches the end of the microstructure. Here the propagation of crack occurs through collection of predictions of paths from the local graphs built at these grain boundary junctions.

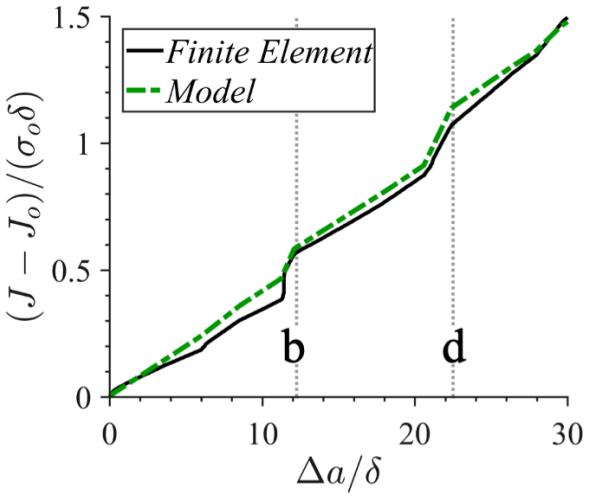

Figure B.12: Comparisons of crack growth resistance curves predicted using evolving graph method and microstructure-based finite element model for connected microstructural network with average grain size, $d_g = 5\delta$ as shown in Figure B.11. Comparison of curves of normalized $J, (J - J_0)/(\sigma_0 \delta)$, versus normalized crack extension $\Delta a/\delta$ computed from finite element calculations (solid line) and graph model (dashed green line). The dotted grey lines, b and d correspond to the locations of propagation of crack in Figure B.11(b) and Figure B.11(d).

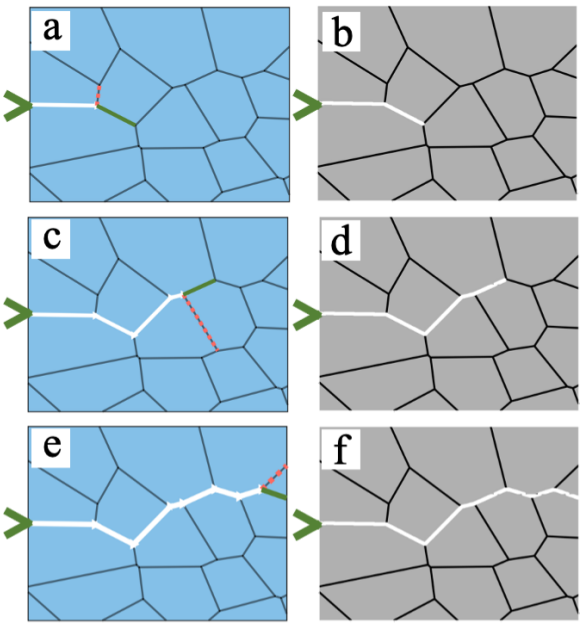

Figure B.13: Comparisons of crack path predicted using evolving graph method and microstructure-based finite element model for connected microstructural network with average grain size, $d_g = 7.5\delta$ shown at three different time steps. (a) construction of a local graph at the grain boundary junction from the network of grain boundaries at this particular junction and then the selection of a crack path with least crack growth resistance, ΔJ. Possible crack paths are highlighted as red dashed lines and the selected crack path is shown in solid green line. The solid white line shows the propagation of crack till this grain boundary junction where the local graph is built. (b) shows the path predicted using the finite element calculation for the particular time step in (a). (c) shows the another instance of construction of a local graph at this inclusion and then selection of the path with minimum ΔJ. (d) shows the path predicted from finite element calculations for the particular time step in (c). Similarly (e) and (f) show path predicted from graph model and finite element calculations as the crack reaches the end of the microstructure. Here the propagation of crack occurs through collection of predictions of paths from the local graphs built at these grain boundary junctions.

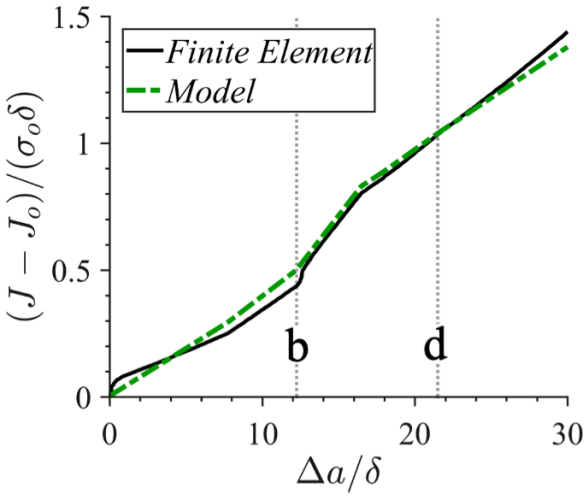

Figure B.14: Comparisons of crack growth resistance curves predicted using evolving graph method and microstructure-based finite element model for connected microstructural network with average grain size, $d_g = 7.5\delta$ as shown in Figure B.13. Comparison of curves of normalized $J, (J - J_0)/(\sigma_0 \delta)$, versus normalized crack extension $\Delta a/\delta$ computed from finite element calculations (solid line) and graph model (dashed green line). The dotted grey lines, b and d correspond to the locations of propagation of crack in Figure B.13(b) and Figure B.13(d).

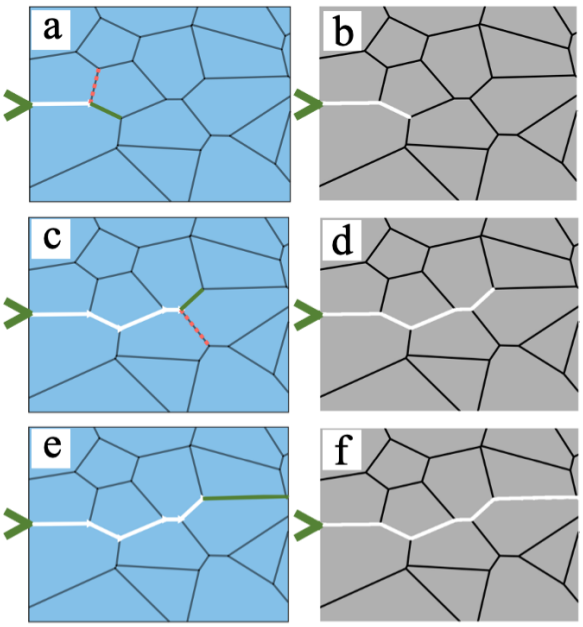

Figure B.15: Comparisons of crack path predicted using evolving graph method and microstructure-based finite element model for connected microstructural network with average grain size, $d_g = 7.5\delta$ shown at three different time steps. (a) construction of a local graph at the grain boundary junction from the network of grain boundaries at this particular junction and then the selection of a crack path with least crack growth resistance, ΔJ. Possible crack paths are highlighted as red dashed lines and the selected crack path is shown in solid green line. The solid white line shows the propagation of crack till this grain boundary junction where the local graph is built. (b) shows the path predicted using the finite element calculation for the particular time step in (a). (c) shows the another instance of construction of a local graph at this inclusion and then selection of the path with minimum ΔJ. (d) shows the path predicted from finite element calculations for the particular time step in (c). Similarly (e) and (f) show path predicted from graph model and finite element calculations as the crack reaches the end of the microstructure. Here the propagation of crack occurs through collection of predictions of paths from the local graphs built at these grain boundary junctions.

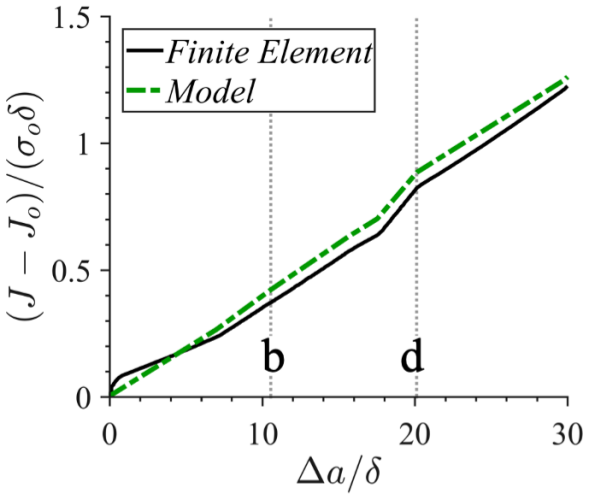

Figure B.16: Comparisons of crack growth resistance curves predicted using evolving graph method and microstructure-based finite element model for connected microstructural network with average grain size, $d_g = 7.5\delta$ as shown in Figure B.15. Comparison of curves of normalized $J, (J - J_0)/(\sigma_0 \delta)$, versus normalized crack extension $\Delta a/\delta$ computed from finite element calculations (solid line) and graph model (dashed green line). The dotted grey lines, b and d correspond to the locations of propagation of crack in Figure B.15(b) and Figure B.15(d).

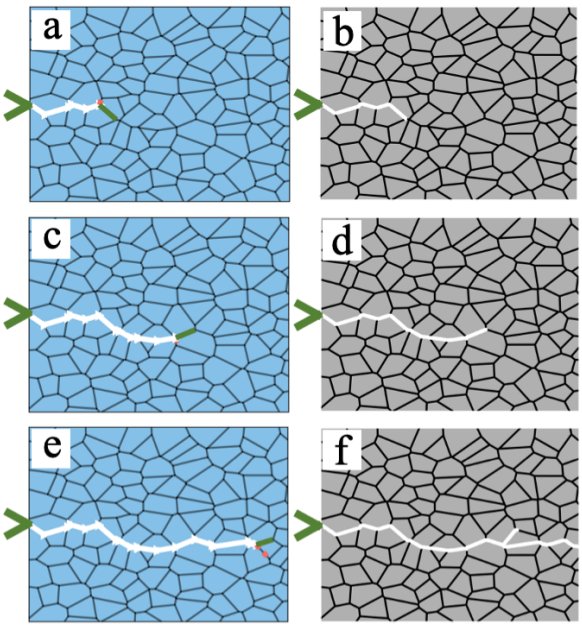

Figure B.17: Comparisons of crack path predicted using evolving graph method and microstructure-based finite element model for connected microstructural network with average grain size, $d_g = 2.5\delta$ shown at three different time steps. (a) construction of a local graph at the grain boundary junction from the network of grain boundaries at this particular junction and then the selection of a crack path with least crack growth resistance, ΔJ. Possible crack paths are highlighted as red dashed lines and the selected crack path is shown in solid green line. The solid white line shows the propagation of crack till this grain boundary junction where the local graph is built. (b) shows the path predicted using the finite element calculation for the particular time step in (a). (c) shows the another instance of construction of a local graph at this inclusion and then selection of the path with minimum ΔJ. (d) shows the path predicted from finite element calculations for the particular time step in (c). Similarly (e) and (f) show path predicted from graph model and finite element calculations as the crack reaches the end of the microstructure. Here the propagation of crack occurs through collection of predictions of paths from the local graphs built at these grain boundary junctions.

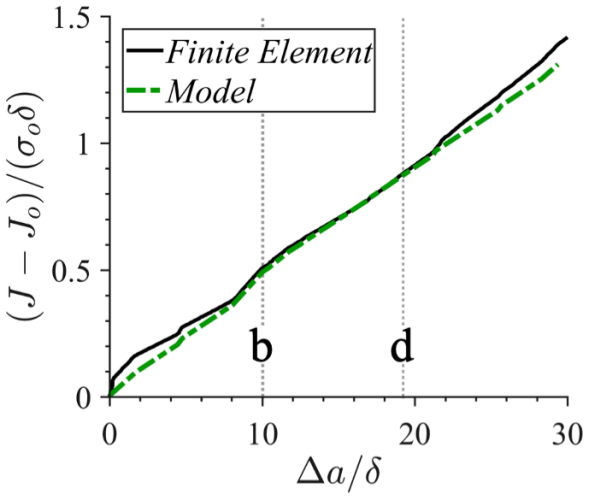

Figure B.18: Comparisons of crack growth resistance curves predicted using evolving graph method and microstructure-based finite element model for connected microstructural network with average grain size, $d_g = 2.5\delta$ as shown in Figure B.17. Comparison of curves of normalized $J, (J - J_0)/(\sigma_0 \delta)$, versus normalized crack extension $\Delta a/\delta$ computed from finite element calculations (solid line) and graph model (dashed green line). The dotted grey lines, b and d correspond to the locations of propagation of crack in Figure B.17(b) and Figure B.17(d).

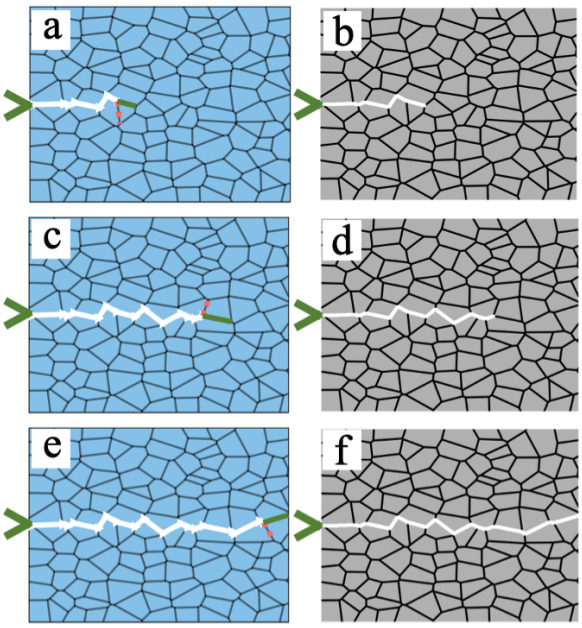

Figure B.19: Comparisons of crack path predicted using evolving graph method and microstructure-based finite element model for connected microstructural network with average grain size, $d_g = 2.5\delta$ shown at three different time steps. (a) construction of a local graph at the grain boundary junction from the network of grain boundaries at this particular junction and then the selection of a crack path with least crack growth resistance, ΔJ. Possible crack paths are highlighted as red dashed lines and the selected crack path is shown in solid green line. The solid white line shows the propagation of crack till this grain boundary junction where the local graph is built. (b) shows the path predicted using the finite element calculation for the particular time step in (a). (c) shows the another instance of construction of a local graph at this inclusion and then selection of the path with minimum ΔJ. (d) shows the path predicted from finite element calculations for the particular time step in (c). Similarly (e) and (f) show path predicted from graph model and finite element calculations as the crack reaches the end of the microstructure. Here the propagation of crack occurs through collection of predictions of paths from the local graphs built at these grain boundary junctions.

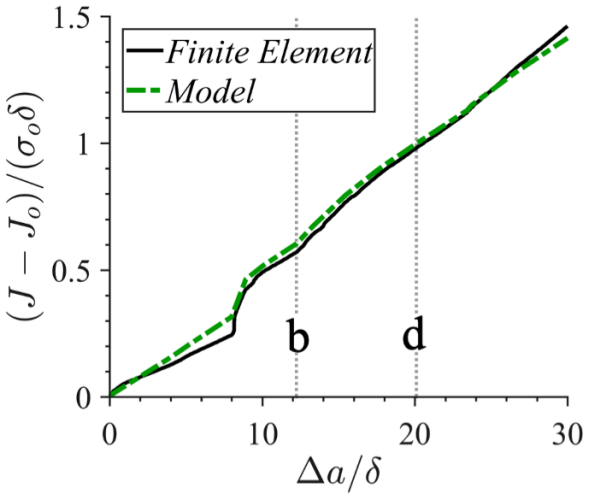

Figure B.20: Comparisons of crack growth resistance curves predicted using evolving graph method and microstructure-based finite element model for connected microstructural network with average grain size, $d_g = 2.5\delta$ as shown in Figure B.19. Comparison of curves of normalized $J, (J - J_0)/(\sigma_0 \delta)$, versus normalized crack extension $\Delta a/\delta$ computed from finite element calculations (solid line) and graph model (dashed green line). The dotted grey lines, b and d correspond to the locations of propagation of crack in Figure B.19(b) and Figure B.19(d).